Platinum Electrocatalysis: Novel Insights into the Dissolution Mechanism and Oxygen Reduction Reaction

by

Mohammad J. Eslamibidgoli

M.Sc. (Physics), Memorial University of Newfoundland, 2012
B.Sc. (Physics), Shahid Beheshti University, 2009

Dissertation Submitted in Partial Fulfillment of the
Requirements for the Degree of
Doctor of Philosophy

in the
Department of Chemistry
Faculty of Science

SIMON FRASER UNIVERSITY
Summer 2016

Approval

Name: **Mohammad J. Eslamibidgoli**

Degree: **Doctor of Philosophy (Chemistry)**

Title: ***Platinum Electrocatalysis: Novel Insights into the Dissolution Mechanism and Oxygen Reduction Reaction***

Examining Committee: **Chair:** Dr. Roger Linington
Associate Professor

Dr. Michael H. Eikerling
Senior Supervisor
Professor _____

Dr. Hua-Zhong Yu
Supervisor
Professor _____

Dr. Noham Weinberg
Supervisor
Adjunct Professor _____

Dr. Tim Storr
Internal Examiner
Associate Professor _____

Dr. Joerg Rottler
External Examiner
Associate Professor
Department of Physics & Astronomy
University of British Columbia _____

Date Defended: July 29, 2016

Abstract

Formation of hydrogen peroxide and oxygenated radical species are the leading cause of chemical degradation observed in polymer electrolyte membranes (PEM) in polymer electrolyte fuel cells. Recent experimental studies have shown that Pt nano-deposits in the PEM, which originate from Pt dissolution in the catalyst layer, play an important role in radical-initiated membrane degradation. Surface reactions at Pt particles facilitate the formation of reactive oxygen species. The net effect of Pt surface processes on membrane degradation depends on the local equilibrium conditions around the Pt nano-deposits, specifically, their equivalent local electrode potential.

In this thesis, we first present a multi-step theoretical approach, validated by a collaborative experimental study, to understand the impact of environmental conditions around the Pt nanodeposits on membrane chemical degradation. In the first step, we developed a physical analytical model for the potential distribution at Pt nanodeposits in the PEM. Given the local potential, we identify the surface adsorption state of Pt. Thereafter, density functional theory (DFT) was used to investigate the influence of the Pt adsorption state on the mechanism of oxygen reduction reaction (ORR), particularly the formation of hydrogen peroxide and hydroxyl radical as the two important reactive oxygen species for membrane degradation.

In a separate work, we employed DFT to study the atomistic mechanism for interfacial place-exchange between surface Pt atom and chemisorbed oxygen at oxidized Pt (111)-water interfaces. Understanding the criteria for Pt oxide growth is a crucial step to comprehend the mechanisms of Pt dissolution during electrochemical processes.

Keywords: Pt Electrocatalysis; Oxygen Reduction Reaction; Pt-In-The-Membrane; Membrane Degradation; Place-exchange Mechanism; Pt Dissolution; Theoretical Modelling; Density Functional Theory

Dedication

I would like to dedicate this thesis to my loving grandparents. The relationships and bonds that I have with my grandparents hold an enormous amount of meaning to me.

Acknowledgements

A special word of thanks goes to my family for their continuous support and encouragement. I would like to acknowledge and extend my heartfelt gratitude to my senior supervisor, Prof. Michael H. Eikerling, for his greatest advices, expertise and knowledge, and his honest encouragement and consultations, which guided me through my graduate program. I would also like to thank my supervisory committee Prof. Noham Weinberg and Prof. Hua-Zhong (Hogan) Yu. I would acknowledge the financial assistance provided by Ballard Power Systems and Automotive Partnership Canada (APC), and the opportunity given to me to conduct research in the CaRPE-FC network. I would also acknowledge the computational resources provided at WestGrid and Compute Canada. I would like to convey my thanks to Prof. Andreas Friedrich and Dr. Stefan Helmly for their contributions in conducting and overseeing the experimental part of this work. Finally, I wish to express a sincere thank you to all the past and present members of Eikerling research group.

Table of Contents

List of Tables

List of Figures

Preface

This thesis is based on our theoretical and modelling works carried out since Sept. 2012. It expands the state of understanding about the origin of Pt nanodeposits in the polymer electrolyte membrane, as well as their role on radical-initiated membrane degradation in polymer electrolyte fuel cells. Due to the nature of the topic, our studies were soon linked to fundamental investigations of the oxygen reduction reaction mechanism, as well the place-exchange mechanism at Pt surfaces. These subjects are highly important, particularly for scientists in the field of fuel cell electrocatalysis. A major part of the thesis has been published and is to be published as follows:

Chapter 3: M. J. Eslamibidgoli, P. A. Melchy, and M. H. Eikerling, "Modelling the local potential at Pt nanoparticles in polymer electrolyte membranes," *Physical Chemistry Chemical Physics*, 17(15), 9802-9811, 2015.

Chapter 4: M. J. Eslamibidgoli, and M. H. Eikerling, "Electrochemical Formation of Reactive Oxygen Species at Pt (111) — A Density Functional Theory Study," *ACS Catalysis* 5(10), 6090-6098, 2015.

The experimental results will be published as: S. Helmly, M. J. Eslamibidgoli, K. A. Friedrich, and M. H. Eikerling, "Impact of Electrochemical Conditions around Pt Deposits in Polymer Electrolyte Membranes on Ionomer Decomposition — An Experimental Study," Submitted, 2016.

Chapter 5: M. J. Eslamibidgoli, and M. H. Eikerling. "Atomistic Mechanism of Pt Extraction at Oxidized Surfaces: Insights from DFT," *Electrocatalysis* 7, 345, 2016.

Part of the results presented in the thesis were also discussed in our perspective article: M. J. Eslamibidgoli, J. Huang, T. Kadyk, A. Malek, and M. H. Eikerling, "How Theory and Simulation Can Drive Fuel Cell Electrocatalysis," *Nano Energy*, 2016, DOI:10.1016/j.nanoen.2016.06.004.

Acronyms

1D	One-dimensional
3D	Three-dimensional
AFM	Atomic force microscopy
AST	Accelerated stress test
BO	Born-Oppenheimer (approximation)
BOL	Beginning of life
BP	Bipolar plates
BV	Butler-Volmer (equation)
CCM	Catalyst coated membrane
CHE	Computational hydrogen electrode
CL	Catalyst layer
CPET	Coupled proton enectron transfer
CV	Cyclic voltammetry
DFT	Density functional theory
DOE	Department of energy
DOS	Density of states
EOL	End of life
eV	Electron volt
EQCN	Electrochemical quartz-crystal nanobalance
fcc	Face-centred cubic
FED	Free energy diagram
FER	Fluoride emission rate
FRR	Fluoride release rate
FTIR	Fourier transform infrared
GDL	Gas diffusion layer
GFC	Gas flow channel
GGA	Generalized gradient approximation
HB	Hydrogen bond
hcp	Hexagonal close-packing
HF	Hartree-Fock
HOR	Hydrogen oxidation reaction
HUPD	Hydrogen under-potential deposition
KS	Kohn Sham
LCAO	Linear combination of atomic orbitals
LDA	Local density approximation
LSDA	Local spin density approximation
MEA	Membrane electrode assembly
MEP	Minimum energy pathway
MD	Molecular dynamics
ML	Monolayer (Unit of coverage)
NEDO	New energy and industrial technology development
NMR	Nuclear magnetic resonance

OCP	Open circuit potential
OCV	Open circuit voltage
ORR	Oxygen reduction reaction
PAW	Projector augmented wave method
PBE	Perdew-Burke-Ernzerhof
PDOS	Projected density of states
PEFC	Polymer electrolyte fuel cell
PEM	Polymer electrolyte membrane
PFSA	Perfluorosulfonic acid
PITM	Pt-in-the-membrane
PSSA	Polystyrene sulfonic acid
PTFE	Polytetrafluoroethylene
PW	Plane wave (basis set)
QM	Quantum mechanics
ReaxFF	Reactive force field
RH	Relative humidity
RHE	Relative hydrogen electrode
SEM	Scanning electron microscopy
SHE	Standard hydrogen electrode
STM	Scanning tunnelling microscopy
TEM	Transmission electron microscopy
VASP	Vienna ab initio simulation package
XPS	X-ray photoelectron spectroscopy

Symbols

F	Faraday constant, C/mol
R	Gas constant, $J/molK$
T	Temperature, K
C_{ref}	Reference concentration, mol/cm^3
E^{eq}	ORR equilibrium potential, V
H_{H_2}	Henry's law constant for H_2 in Nafion®, mol/cm^3kPa
H_{O_2}	Henry's law constant for O_2 in Nafion®, mol/cm^3kPa
$D_{H_2}^{\text{nano}}$	H_2 diffusion coefficient at nanoscale, cm^2/s
$D_{O_2}^{\text{nano}}$	O_2 diffusion coefficient at nanoscale, cm^2/s
$D_{H_2}^{\text{macro}}$	H_2 diffusion coefficient at macroscale, cm^2/s
$D_{O_2}^{\text{macro}}$	O_2 diffusion coefficient at macroscale, cm^2/s
j_{ORR}^0	ORR exchange current density, A/cm^2
j_{HOR}^0	HOR exchange current density, A/cm^2
α_{HOR}^a, α_{HOR}^c	Anodic and cathodic transfer coefficients for HOR
α_{ORR}^a, α_{ORR}^c	Anodic and cathodic transfer coefficient for ORR
$p_{H_2}^0$	H_2 pressure at membrane | anode, kPa
$p_{O_2}^0$	O_2 pressure at membrane | cathode, kPa
r_0	Particle radius, nm
n_{pt}	Particle density, μm^{-3}
x	Dimensional coordinate along PEM thickness, μm
l	Membrane thickness, μm
ξ	Dimensionless coordinate along PEM thickness
Λ	Dimensionless reaction penetration depth
ΔG	Free energy of adsorption, eV
ΔE	Binding energy, eV
ΔZPE	Zero-point energy change, eV
$T\Delta S$	Entropy change, eV
ΔG_{pH}	Free energy contributions due to change in pH, eV
ΔG_U	Free energy contributions due to change in potential, eV
μ	Dipole moment, D
Φ	Work Function, eV
$\Delta\rho$	3D charge density difference, $e/\text{Å}^3$
$\Delta\lambda$	Planar average of the induced charge density, $e/\text{Å}$

Chapter 1

Introduction

1.1 Fuel Cell Technology

Fuel cells are electrochemical devices that convert the chemical energy stored in hydrogen directly into electrical energy to generate electricity and produce water and heat. They have the power to significantly reduce our dependence on fossil fuels, and can have nearly zero emissions of greenhouse gases during operation[1–3]. With no moving parts, fuel cells are a highly suitable technology for a plethora of applications such as in transportation, as well as stationary and portable devices[4,5].

The concept of a fuel cell was developed more than 150 years ago[6,7]. Christian Friedrich Schönbein (1799 -1868) was a German scientist who first conceived the idea of a fuel cell[8]. At the same time, Sir William Robert Grove, a barrister turned scientist in London, built the first prototype of a fuel cell in 1839, which he named the gas voltaic battery. The schematic view of his cell is shown in Fig. 1.1. It consists of several primitive cells connected to a voltmeter[7]. Grove discovered that with arranging two platinum electrodes immersed in sulfuric acid, a cell current was maintained as long as oxygen and hydrogen within the cell were provided. Hydrogen is oxidized at the anode, where protons and electrons are produced in the hydrogen oxidation reaction (HOR),

$$H_2 \rightarrow 2H^+ + 2e^- \qquad E^0 = 0\,V; \tag{1.1}$$

where, E^0 is the equilibrium potential of the reaction at standard conditions (pressure 1 atm, temperature 25°C)[9]. The electrons are conducted via an external circuit to do electrical work. Protons are transported through sulfuric acid to the cathode. At the cathode, oxygen, electrons from the external circuit and protons recombine in the oxygen reduction reaction (ORR) to form water,

$$O_2 + 4H^+ + 4e^- \rightarrow 2H_2O \qquad E^0 = 1.23\ V. \tag{1.2}$$

The overal electrochemical reaction for the cell is,

$$O_2 + 2H_2 \rightarrow 2H_2O \qquad E^0 = 1.23\ V. \tag{1.3}$$

Grove apparently understood how promising and powerful his gas voltaic battery could be; as he wrote, "the device could shock five people holding their hands and one of them holding the device"[7]. However, the fuel cell was not implemented in those years both because of the development of the dynamo technology, and due to easily accessible oil and the invention of the combustion engine.

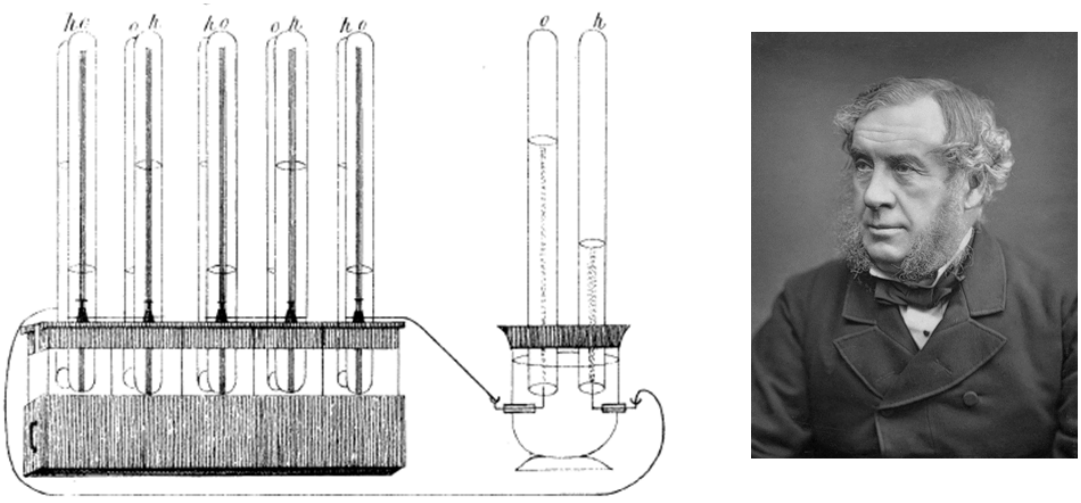

Figure 1.1: William Grove's picture, and the schematic view of his cell; a battery of five cells is shown filled with oxygen and hydrogen, labeled "o" and "h" in the drawing. The battery is connected to the voltmeter, the tubes of which are of the same size as those of the battery. Adapted from Ref. 7.

In the 1950's another British scientist, Francis Thomas Bacon, demonstrated the first practical use of a hydrogen-oxygen fuel cell stack, although there was a long history of scientific curiosities for fuel cell development between the 1840's and 1950's[10]. Building on these efforts, there has been further development to transform fuel cells into powerful and practical devices. The first generation of fuel cells was produced by General Electric in the 1960's, when an alkaline fuel cell was used to power the electrical system of NASA's Gemini space capsules[11]. Polymer electrolyte membranes (PEM) were incorporated into hydrogen fuel cells by Grubb and Niedrach in 1960 at General Electric[12]. Polymer elec-

trolyte fuel cells (PEFCs) operate at low temperature (below 100 °C), and they generate power densities in excess of 0.6 $W\ cm^{-2}$, higher than that of other types of fuel cells [10,13,14].

Nowadays, the most attractive applications of fuel cells are in electric vehicles to replace the internal combustion engines. The fuel cell generates electricity that can be used to power a car, truck, bus or other vehicles as long as hydrogen is supplied as fuel. Hydrogen can be produced in many different ways such as water electrolysis and steam methane reforming [1,15,16]; once produced, hydrogen can be stored as a compressed gas or liquid, or in a chemical or metal compound [15]. If a fuel cell is supplied with pure hydrogen, the emissions of greenhouse gases are nearly zero. Demonstration projects over the last decade have shown the competitiveness of fuel cell electric vehicles to internal combustion engine powered vehicles in terms of driving range, performance, reliability, and flexibility in vehicle design [17]. These factors have driven the global push towards PEFC technology in automotive applications. However, cost-effective utilization of materials as well as their stability and cycle life in the operating cell have remained as the major challenges, which must be successfully addressed in order to commercialize PEFCs for automotive applications [17].

1.1.1 Principles of Materials and Operation

Fig. 1.2 illustrates the operation of a PEFC, fuelled with hydrogen. A single PEFC is made up of two plates (flow field), two electrodes (anode and cathode), and two thin layers of Pt based catalysts, separated by a plastic membrane. When hydrated, the membrane allows proton transport across the cell, while it does not conduct electrons. It also minimizes fuel crossover from the anode to the cathode by separating the oxidizing and reducing environments. These components are placed together in the cell along with gas flow channels (GFCs), and bipolar plates (BP).

The processes that occur during fuel cell operation involve heat transfer, species and charge transport, and electrochemical reactions. As shown in Fig. 1.2, hydrogen and oxygen are directed from the flow field plates to the respective porous gas diffusion layers (GDLs) of the anode and the cathode, and diffuse into the respective catalyst layars (CLs). Hydrogen is oxidized at the anode via the HOR. The electrons are conducted via the carbon support to the anode current collector, and then to the cathode current collector, via an external circuit. Protons are transported through the membrane. At the cathode CL, oxygen from the air, electrons from the external circuit, and protons recombine in the ORR to form water. Water is transported out of the cathode CL through the cathode GDL, and eventually out of the flow channel; heat is generated due to thermodynamic inefficiencies, mainly in

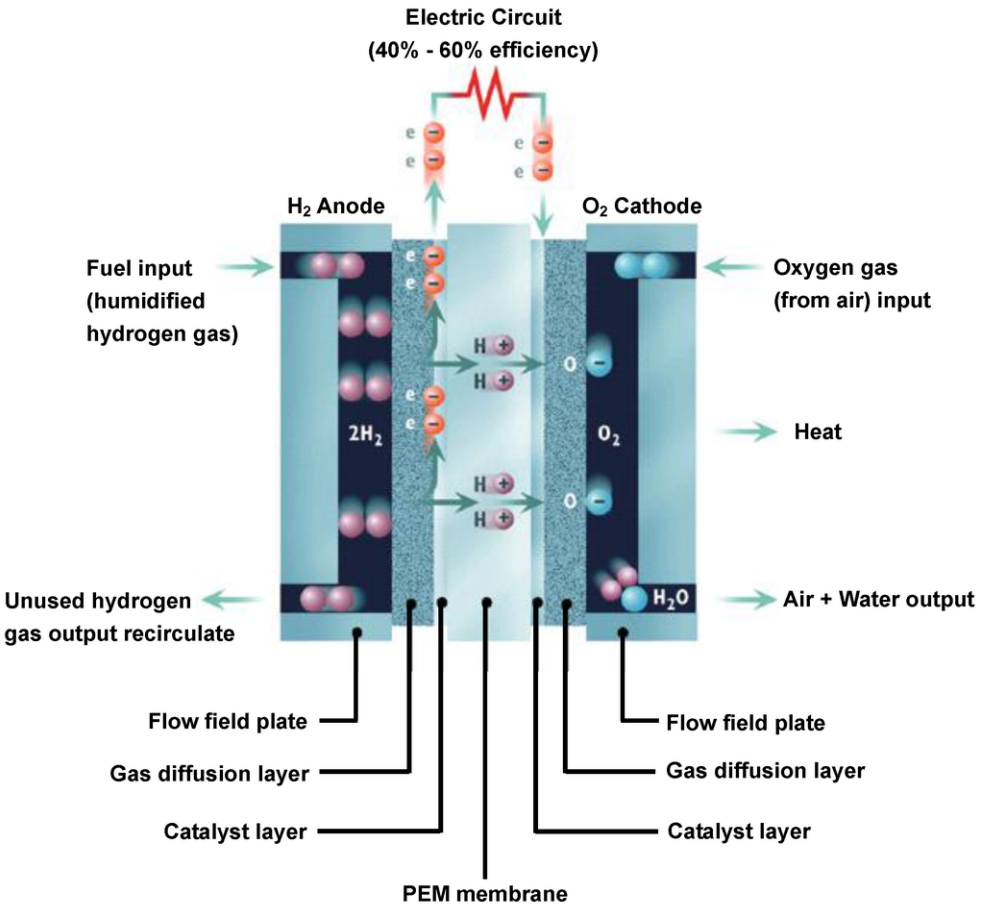

Figure 1.2: Schematic of representative PEFC, showing functional components and processes: Flow fields, gas diffusion layers, catalyst layers, and polymer electrolyte membrane.

the sluggish ORR at the cathode CL, and is conducted out of the cell via carbon support and BPs.

As for the PEM in PEFCs, various ionomers have been tested such as non-fluorinated polyaryl ionomers, polystyrene sulfonic acid (PSSA) and perfluorosulfonic acid (PFSA) ionomers. Among PFSA ionomers, Du Pont's Nafion® was introduced in the 1970's, which could essentially solve the problems associated with proton conductivity and durability of previous membranes[18]. The discovery of Nafion® set new standards in performance, chemical and mechanical durability, as well as the commercial accessibility of PEMs[19,20]. The chemical structure of Nafion is shown in Fig. 1.3. It consists of a polytetrafluoroethylene (PTFE) backbone and perfluorovinylether side chains terminated by sulfonic acid head groups.

Pt and Pt-based alloys are the most effective materials to electro-catalyze the HOR and the ORR in the PEFCs[21–24]. Unfortunately, Pt abundance in the earth is low; thus, Pt is

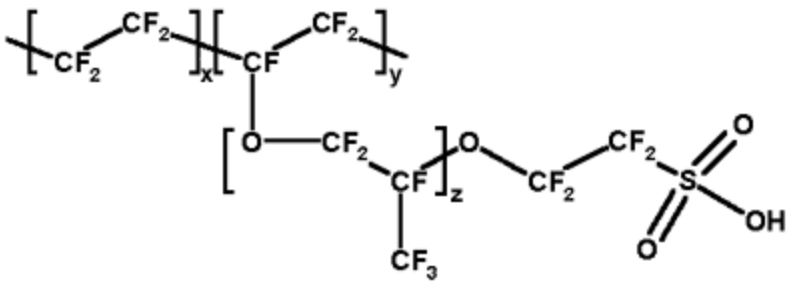

Figure 1.3: Chemical Structure of Nafion

expensive, and it contributes a major fraction of the cost of a fuel cell stack (30% to 70% depending on the electrode design). Therefore, it is essential to bring down the Pt loading (in mg cm^{-2}), while increasing the cell performance and durability.

Major advancements were achieved to bring down the Pt loading from $\sim 4-28$ mg cm^{-2}, as used in the catalysts of Gemini space shuttle[25], to less than ~ 0.4 mg cm^{-2} [26], which is the state-of-the-art in modern days. Groundbreaking progress was made in the late 1980's by developing carbon supported Pt catalysts bound by Nafion®, which led to an increase of the surface area-to-volume ratio of Pt[27,28]. The investigations to further bring down the Pt loadings continue in different ways, which include varying the surface morphology and surface roughness of extended surface catalysts[29–33]; modification in the electronic structure properties of Pt by mixing it with other metals[21–24]; varying the size, shape and morphology of Pt or Pt-alloy nanoparticles[34–40], and variation in the support materials[24,30,32,37,38,41–44]. Extensive investigations aim at finding more stable and less expensive catalyst materials than Pt, with equal or higher activity for the ORR[40,45,46].

The design of a catalyst layer (CL) as a porous gas diffusion electrode, which utilizes carbon-supported Pt nanoparticles as the active material, and which is impregnated with ionomer in order to achieve a high proton conductivity, represents the state-of-the-art in modern day PEFCs[13]. Fig. 1.4 shows the schematic of a typical PEM fuel cell catalyst layer structure[13].

Understanding the mechanisms of the multi-step ORR at Pt is of particular importance for fuel cell operation[47]. The overpotential required to drive the ORR at the cathode contributes in 30% to 40% of voltage losses in PEFCs. The cathode potential in the fuel cell typically varies between 0.6 V to 0.95 V during operation. In this potential window, adsorbed oxygen intermediates from the ORR compete for free catalyst surface sites with thermodynamically stable oxygen-containing adsorbates that are present due to the oxidation of water. On the other hand, potentials up to 1.5 V are possible to occur during start up and shutdown transitions. At this higher potential range, a surface oxide layer is formed

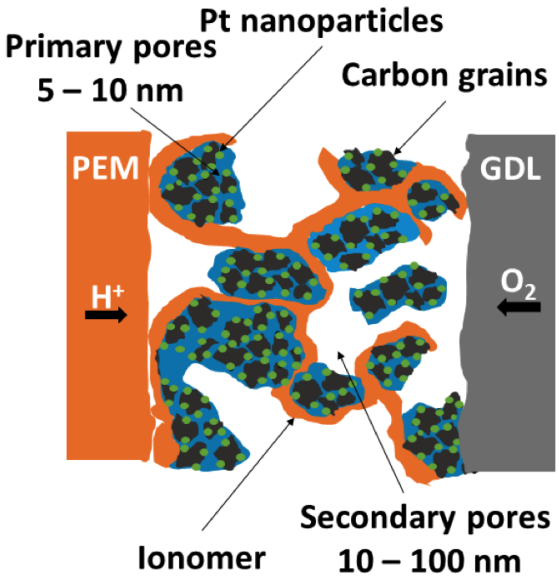

Figure 1.4: Schematic of a typical PEM fuel cell cathode catalyst layer structure.

at Pt. Potential cycling that repeatedly forms and removes this layer results in a high Pt dissolution rate[48,49]. This suggests that the activity of Pt for the ORR and for dissolution can be strongly correlated[50]. Theoretically, the activity vs. stability of the catalyst involves the interplay between parameters related to catalyst composition, morphology, electronic structure, interactions with the support, surface adsorption state, electrostatic interfacial effects, and local reaction conditions provided by surrounding system components.

Overall, a deeper understanding of the principles of materials and operation involved in various components of the fuel cell is required[51]. To accurately describe the relevant operation phenomena in PEFCs, and to predict the performance and durability of the fuel cell, it is essential to develop theoretical models, along with experimental methods, which range from the atomistic scale up to the system level. The grand challenge in modelling is the unavoidable coupling between the phenomena occuring in a wide range of time and length scales. Various approaches have been developed to describe the key processes taking place at a given scale. In this regard, the state-of-the-art in the modelling of PEFC performance and degradation, with correlation to experiment is (i) first-principle approaches at atomistic level, (ii) microscale simulations, (iii) mathematical modelling of different cell components, and (iv) modelling at the stack level.

Table 1.1: Long-term targets and recent milestones for fuel cell vehicles. Adapted from Ref. 18.

Characteristic	Units	2007 Status	2010	2015	2020—2030
Vehicle efficiency	%	50	>50	60	>60
Durability	Hours	1,000	3,000	5,000	> 5,000
Operating temperature	$^{\circ}C$	80	-30 to 90	-30 to 90-100	-40 to 100-120
Cost	$/kW	—	(539-647)	108	43

1.2 Motivation

Commercialization of PEFCs is associated with a balance between the coupled characteristics of durability, performance and cost. Government agencies, particularly in the US, Europe and Japan, have established targets to guide the efforts in order to improve PEFC performance and durability, while decreasing cost. Table 1.1 summarizes the long-term targets and recent milestones for PEFC vehicle efficiency, durability, operating temperature, and cost, according to the Japanese New Energy and Industrial Technology Development Organization (NEDO)[18]. In general, the targets for vehicle efficiency by 2015 have been in a range of 40% to 60%, with Japan setting the highest goal. In terms of operating temperature and relative humidity (RH), the targets for 2020 to 2030 project operation from 100 to 120° C, under non-humidified conditions[18]. For light duty applications, the durability targets by 2015 anticipated 5,000 hours of operation with a cost of $\sim$ \$ $110/kW$[17]. On the other hand, for the development of the next generation heavy duty (bus) fuel cells with durability comparable to or better than current diesel engines, 20,000 hours of operation, including operation with start up and shut down transitions has been targeted[52].

1.2.1 Membrane Chemical Degradation

The durability and longevity of PEFCs are strongly affected by structural degradation of component materials, which is associated with their role in the operation of the fuel cell. In recent years, degradation of the PEMs has become a major focus of fuel cell research, since it strongly impacts the lifetime of the device. Understanding the PEM degradation problem is particularly critical for the development of the next generation heavy duty fuel cells; PEM degradation is accelerated by the harsh operating conditions and the typical voltage cycles. Conditions such as low relative humidity, high temperature, and high cell voltage are known to accelerate the chemical degradation of the membrane[53–55], which in turn results in other issues such as membrane thinning, associated loss of functional ionomer

side-chains, reduced ionomer molecular weight due to chain scission, and consequently the gradual loss in proton conductivity[56]. PEMs are exposed to thermal and mechanical stressors, coupled with the chemical attack of weak bonds of ionomer molecules by oxygenated radical species, generated as by-products of the fuel cell electrochemical reactions[57–59]. Experimental studies linked the chemical degradation of the membrane to the concentrations of these radical species[55,60].

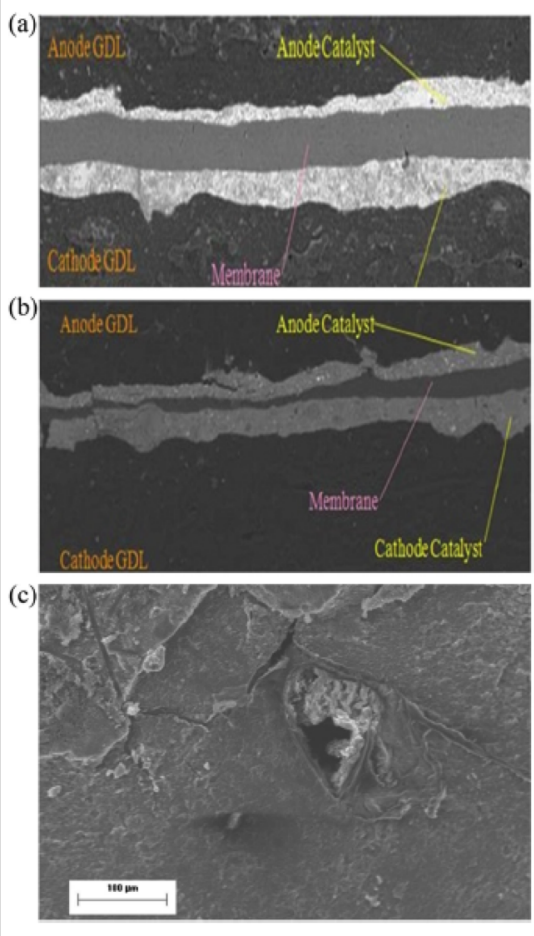

Figure 1.5: SEM micrographs of (a) cross-sectional MEA at the beginning of life (BOL) stage, (b) cross-sectional MEA at the end of life (EOL) stage, and (c) pinhole on the surface of the membrane at EOL. Adapted with permission[61]. Copyright 2014, Elsevier.

As shown in Fig. 1.5, chemical degradation of the membrane results in material loss and membrane thinning, which in turn leads to higher crossover of the reactant gases, which accelerates chemical degradation itself[54,59–61]. Moreover, it weakens the mechanical properties of the membrane, which results in the formation of pinholes, cracks and fractures in the membrane[58,62]. This coupling between chemical and mechanical degradation mechanisms eventually leads to fuel cell failure[54,55].

Various experimental techniques have been employed to study the chemical degradation of the PEMs, such as *in situ* Fourier transform infrared (FTIR) spectro-electrochemical methods [63], X-ray photoelectron spectroscopy (XPS)[64], solid state nuclear magnetic resonance (NMR) spectroscopy[65], scanning electron microscopy (SEM), and transmission electron microscopy (TEM)[66,67]. The test protocols for membrane mechanical and chemical durability have been recommended by the US Department of Energy (DOE)[17]. The accelerated chemical degradation, caused by holding a single cell at open circuit voltage (OCV) for several hundred hours at 30% RH and 90° C, results in degradation of fluorinated PEMs and fluoride release. Membrane degradation is monitored by measuring the fluoride release rate (FRR, also so-called as fluoride emmision rate (FER)) of the cell's effluent water[68,69], measuring membrane thinning[59,62], periodically checking the hydrogen crossover[70,71], and measuring the decrease of ion-exchange capacity[72]. Fig. 1.6 shows the voltage decay and a typical FRR profile under the OCV condition test[73]. Over the course of 200 hour test, the voltage dropped by 850 $\mu V h^{-1}$ and at the end of the test the membrane lost 42% of the initial fluoride inventory[73].

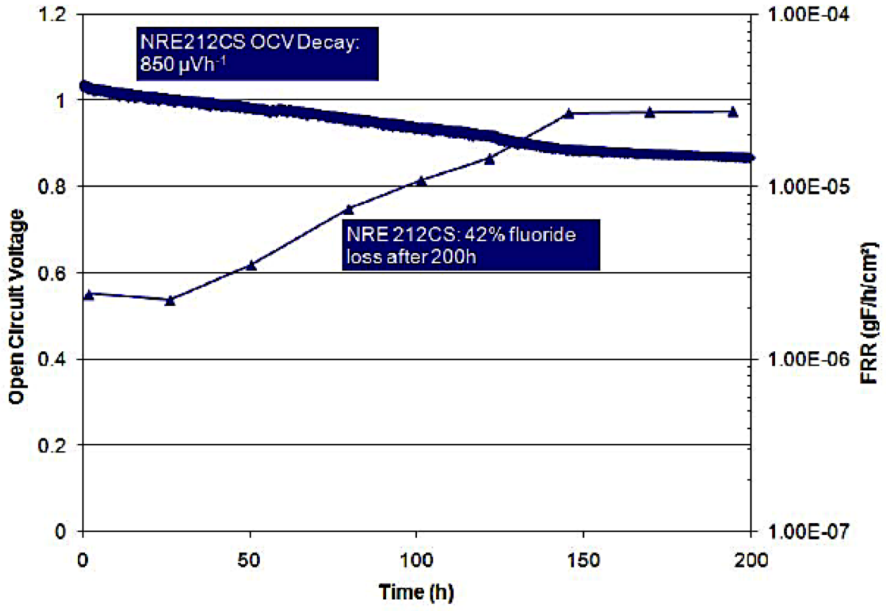

Figure 1.6: Experimental plot of NRE 212CS based MEA under hot, dry OCV (95° C, 50% RH) conditions showing both voltage decay and fluoride release rate (FRR) profiles. Adapted with permission[72]. Copyright 2008, The Electrochemical Society.

1.2.2 Origin and Role of PITM on Membrane Degradation

The generally accepted mechanism to explain membrane degradation has been known for some time to be linked to the formation of hydrogen peroxide. H_2O_2 is an intermediate of the ORR in a 2-electron process,

$$O_2 + 2H^+ + 2e^- \rightarrow H_2O_2 \qquad E^{eq} = 0.67\ V. \tag{1.4}$$

H_2O_2 formation in the PEFCs has been confirmed experimentally[74]. H_2O_2 thus formed could react at iron ion impurities in the PEM to produce attacking radicals via Fenton's reaction[75–81]. It should be noted that impurities are unavoidably present in the membrane from Fe metal ion contamination, originated from end plates in contact with humidified oxygen and hydrogen[59,82]. Conditions such as low relative humidity, high temperature, and high cell voltage accelerate chemical degradation, due to an increased formation of H_2O_2 in the cell[53,54,66]. Therefore, the pathways to the formation of H_2O_2 are of particular importance in order to understand the mechanisms of PEM degradation.

In this context, deposits of Pt-in-the-membrane (PITM) play an important role in initiating membrane chemical degradation. PITM formation is a consequence of Pt dissolution in the cathode catalyst layer[66,81,83–85]. Mobile Pt ion complexes diffuse and migrate into the membrane. They form solid deposits by precipitation in the presence of H_2 and O_2, crossed over from the anode and the cathode, respectively. Formation of PITM is a common observation in the catalyst degradation tests. In the study conducted by Ohma *et al.*[86], it was found that under typical operating conditions, i.e., equal pressure of H_2 and air, the Pt deposits concentrate close to the cathode catalyst layer, as also shown in Fig. 1.7, forming the so-called Pt band[87]. The location of the Pt band depends on the partial pressures of H_2 and O_2 at the membrane/electrode boundaries. The band is formed closer to the anode side for lower partial pressure of hydrogen[88,89].

The effect of PITM on the durability of the PEM is still under debate. Ohma *et al.*[88] found higher rates of membrane degradation in the proximity of the Pt band. Fig. 1.8 shows the relative intensity profiles obtained from a micro-Raman spectroscopy study to analyze the change in the molecular level structure of the membrane. It illustrates a drop in the vicinity of the band, indicating the role of PITM on membrane degradation. Rodgers *et al.* have observed a strong impact of the Pt density on the degradation of Pt-impregnated membranes[85]. Ohguri *et al.* have investigated the formation of $^{\bullet}OH$ at Pt particles in the membrane[90]. In their work, $^{\bullet}OH$ is detected at both the anode and the cathode side, but the amount is much larger for the anode side. Ghassemzadeh *et al.* have observed that the chemical degradation rate was higher in the presence of Pt catalyst for a H_2-rich

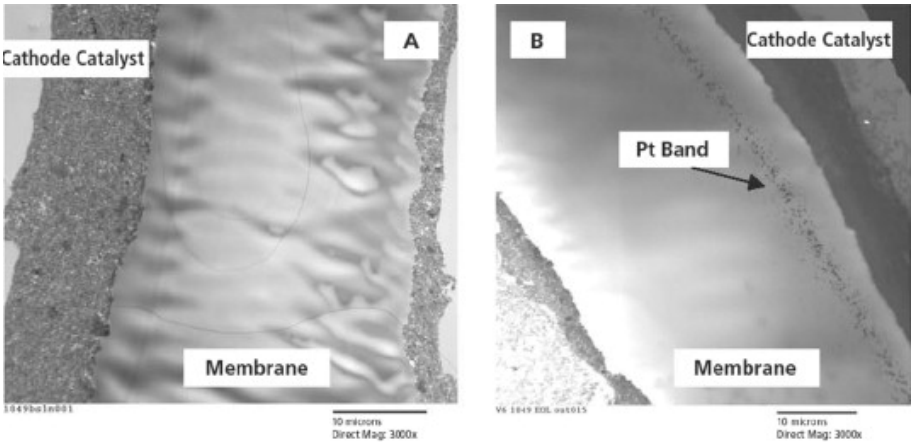

Figure 1.7: A cross-section of the catalyst-coated membrane (CCM) by transmission electron microscopy (TEM), showing catalyst layers and the membrane. (A) beginning of life sample, and (B) after voltage cycling. A Pt band can be identified after voltage cycling. Adapted with permission[86]. Copyright 2009, Elsevier.

mixture of H_2 and O_2 (90% H_2, 2% O_2, 8% Ar) as compared to an O_2 -rich mixture (20% O_2, 2% H_2, 78% Ar)[75]. A similar trend was reported by Aoki *et al.*[76,77], and Ohma *et al.*[78] Other researchers have observed severe membrane degradation in the presence of Pt particles[79–81]; it has also been found that PITM can enhance durability by deactivating radicals and/or H_2O_2[84,91,92].

Therefore, solid Pt nanodeposits can play a double-edge role in membrane chemical degradation. They can provide catalyst surface sites for processes involved in the formation or scavenging of radicals/hydrogen peroxide. The net rate of H_2O_2 formation/decomposition at PITM is considered to depend on three conditions (which also influence each other): distribution of Pt particles in the membrane (i.e., their size, distance, number per volume unit)[81,85,89]; (ii) particle shape,[84,91] and (iii) environmental conditions around particles (i.e., local mole fractions of H_2 and O_2, temperature, pH and RH)[75–81]. The first two conditions have been experimentally well investigated with the observations that degradation decreased when particles were distributed at a high density[85], or as particles were present in a faceted shape such as star or dendritic shape[84]. The influence of electrochemical conditions, however, has not yet been systematically studied, which is the objective of this work.

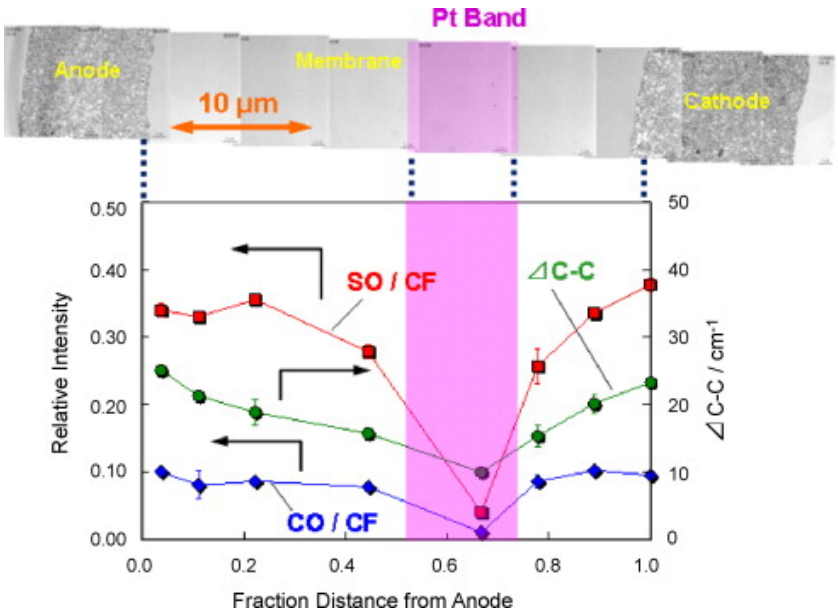

Figure 1.8: Relative intensities of *SO* and *CO* vs. *CF* and Half Bandwidth of *CC* as a function of the fractional distance from the anode. Adapted with permission[85]. Copyright 2007, The Electrochemical Society.

1.2.3 Approach to Investigate the Role of PITM on Membrane Degradation

To understand the impact of PITM on the ionomer decomposition under varying operational conditions, it is essential to develop a multi-step approach, which involves a complex phenomenology of local reaction conditions as well as surface processes at Pt nanodeposits. Fig. 1.9 summarizes our approach to investigate the impact of Pt nano-deposits on the PEM degradation.

In step 1, as presented in chapter 3, we determine the local electrostatic potential at Pt deposits in the membrane, based on a continuum model of crossover of reactant gases in the membrane coupled with their local electrochemical reactions at the Pt surface[93].

Given the local potential from the first step, we identify in an intermediate step the surface adsorption state of Pt. Thereafter, in step 2, presented in chapter 4, we perform DFT calculations to study specific surface processes involved in the H_2O_2 formation at the model system of Pt (111) - water interface, taking into account the surface adsorption state of Pt corresponding to the local electrode potential obtained in the first step[94].

To validate this approach, we present in chapter 4 a two-step experiment to understand the role of the local electrochemical conditions around PITM on the membrane degradation[95]. For this aim, we first experimentally examine the dependence between reactant concentration and electrical potential of a Pt micro-electrode in a membrane electrode as-

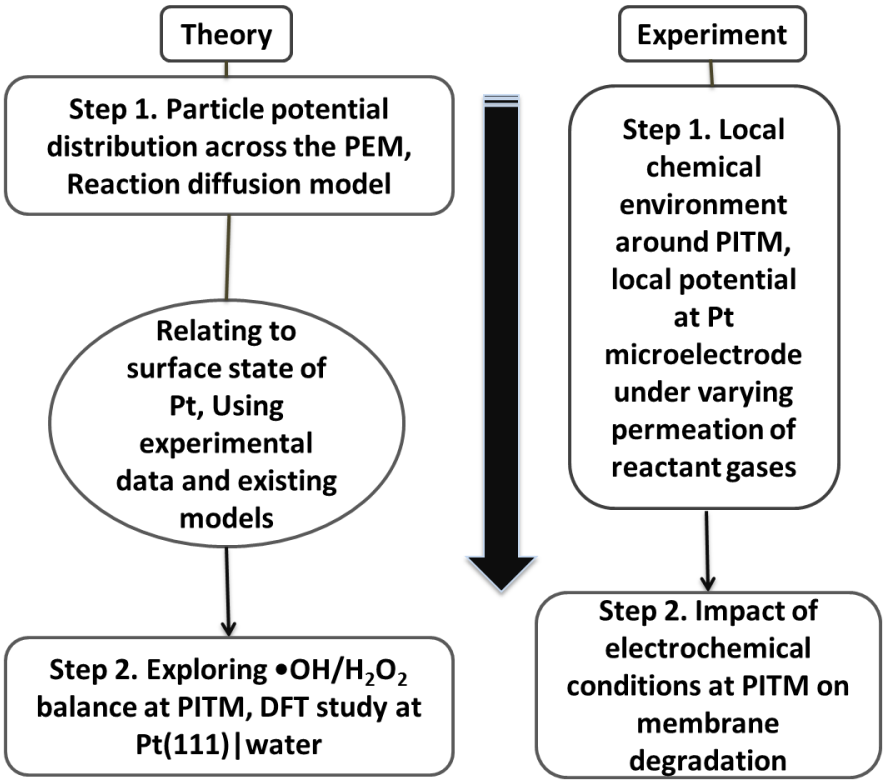

Figure 1.9: Approach to investigate the role of PITM on PEM degradation

sembly (MEA). Subsequently, we investigate the dependence of the electrochemical environment of Pt deposits on ionomer decomposition by performing a degradation test with various model cells, some of which contain PITM.

1.2.4 Atomistic Mechanism of Pt Extraction at Oxidized Surfaces

As discussed, Pt dissolves at the cathode at high potentials, and Pt ions migrate through the membrane due to concentration gradient. In the presence of reactant crossover gases, i.e., H_2 and O_2, Pt ions become deposited in the water channels of the PEM in the form of nanoparticles. Pt dissolution is thus the origin of PITM formation. Understanding the mechanisms of Pt dissolution under electrochemical conditions is a subject of unfading interest in corrosion science as well as energy and environmental science[96–98]. A crucial step in the comprehension of metal dissolution is to understand surface oxidation, a topic that has captivated scientific interest for decades[99]. The third study in this thesis, thus, focuses on the mechanism of oxide formation at Pt.

Experimental studies have found the formation of subsurface oxygen on oxidized Pt surfaces[100–102]. Analysis of CV data of a Pt electrode immersed in 0.5 M aqueous H_2SO_4,

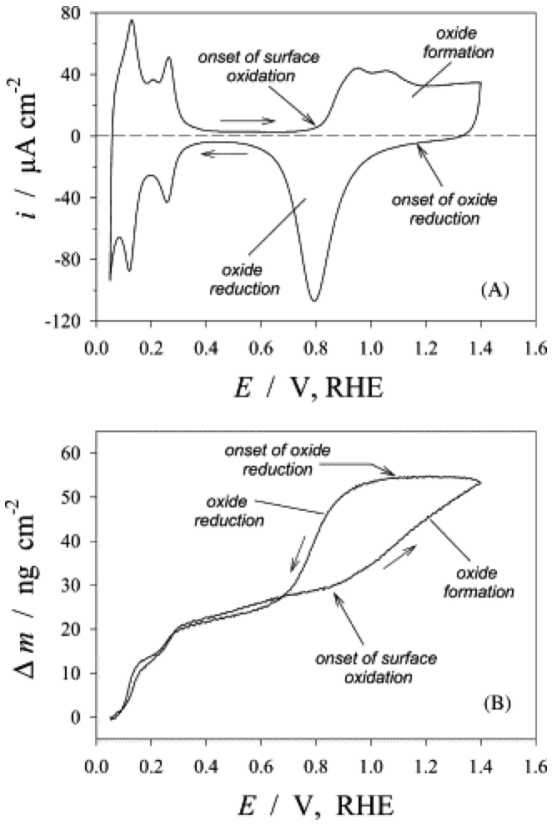

Figure 1.10: Cyclic-voltammetry (i vs. E) profile (A) and mass-response (Δm vs. E) profile (B) for a Pt electrode in 0.5 M aqueous H_2SO_4 solution recorded at s=50 mV S^{-1} and T=298 K. Adapted with permission[100]. Copyright 2004, Elsevier.

recorded concurrently with mass data from an electrochemical quartz-crystal nanobalance, showed that the onset potential of surface oxidation is at around 0.85 V[101], shown in Fig. 1.10. Adsorbed oxygenated species caused by water dissociation at the surface are identified as chemisorbed oxygen at $0.85<\phi^{M}<1.10$ V, which forms up to half of a monolayer (ML) coverage. As the potential increases, further discharge of water molecules leads to the formation of the second half of a monolayer of chemisorbed oxygen that is accompanied by an interfacial "flip" of adsorbed oxygen and surface Pt atoms — commonly referred to as place-exchange or irreversible oxide growth[103].

Recently performed DFT studies have attempted to obtain more detailed molecular level insights on how an initial monolayer of oxide is formed and how oxygen occupies the Pt subsurface[104–107]. Gu and Balbuena[104] focused on the stability of Pt(111) surfaces with oxygen occupying both hollow sites on top of the Pt layer and tetrahedral sites below the top Pt layer at varying coverages. Their results suggests that the tetra-I site is the energetically preferred site for adsorption of atomic oxygen in the subsurface of Pt (111). However, the large activation barrier of ≈ 2.5 eV renders the transfer of surface oxygen to

this site a highly unlikely event. Later, the findings in the work by Asthagiri and coworkers represented a shift in thinking about these surfaces[105]. They considered not only the typical oxygen hollow site occupation but also the experimentally observed effect of Pt buckling at high oxygen coverage[102]. In the buckling phenomenon, a Pt surface atom is displaced from its native lattice position. The buckled Pt screens the repulsion between chemisorbed oxygen atoms, thus leading to more stable phases at oxygen coverage of above half a ML coverage. In that work, however, the researchers were unable to find the minimum energy path at higher oxygen coverage due to the convergence failures of the nudged elastic band calculations; additionally, the possible role of surface water molecules on the buckling process was not explored.

In chapter 5, we employ DFT to present original insights into the atomistic-scale mechanism of interfacial place-exchange between surface Pt atom and chemisorbed oxygen at oxidized Pt(111)-water interfaces[108]. The energy diagrams for the processes of Pt extraction and O^{ads} substitution were generated to determine the local selection criteria for the process. We address the effect of surface coverage with oxygen and the indispensable role of surface water molecules. Results are discussed in terms of surface charging effects caused by oxygen coverage, surface strain effects as well the contribution from electronic interaction effects.

1.3 Thesis Outline

The chapters of this thesis are organized as follows:

- Chapter 2 presents the basic concepts of Hartree-Fock (HF) and DFT methods, and the theoretical treatments for periodic systems by using DFT methods.

- Chapter 3 presents a continuum model to determine the local electrochemical condition at Pt deposits in the membrane. We obtain analytical relations for the crossover of reactant gases in the membrane coupled with their electrochemical reactions at the surfaces of Pt deposits in the PEM to determine the local potential at Pt particles in the membrane.

- Chapter 4 presents DFT calculations to study specific surface processes involved in the formation of H_2O, H_2O_2 and $^{\bullet}OH$ at a model system of a Pt (111) - water interface. We take into account various surface adsorption states of Pt, corresponding to different electrode potential windows. In addition, in this chapter we present a collaborative experimental study to validate our multi-step theoretical approach and

to understand the impact of electrochemical conditions around PITM on membrane degradation.

- Chapter 5 presents a DFT study of the Pt extraction mechanism at oxidized (111) surfaces. We present original insights into the atomistic level mechanism of interfacial place-exchange between surface Pt atom and chemisorbed oxygen at oxidized Pt(111)-water interfaces, the process which may lead to Pt dissolution.

- Finally, Chapter 6 provides conclusions of this work and an outlook on possible future developments in the area of research.

Chapter 2

Theoretical Framework

Density functional theory (DFT) based methods have been widely used in quantum mechanical computations of periodic systems, as well for exploring the potential energy surface of clusters or single molecules. In this chapter, we briefly review the molecular orbital theory with emphasis on the Hartree-Fock (HF) method and DFT, and we present the approach adopted for the *ab initio* study of the electronic structure of periodic systems employed in this thesis.

2.1 The Solution of the Schrödinger Equation

Molecular orbital theory is concerned with obtaining properties of atomic and molecular systems. The fundamental problem involves finding an accurate solution for the Schrödinger equation[109,110]. The non-relativistic Schrödinger equation in the time independent form is given by,

$$\hat{\mathscr{H}}\Psi(\mathbf{r},\mathbf{R}) = E\Psi(\mathbf{r},\mathbf{R})\,; \tag{2.1}$$

where, $\hat{\mathscr{H}}$ is the Hamiltonian operator of the system under consideration, and Ψ is the wave function; **R** and **r** represent the coordinates of nuclei and electrons, and E is the total energy of the system.
The Hamiltonian for a system containing N electrons and M nuclei can be written as

$$\hat{\mathscr{H}} = \hat{T}_n + \hat{T}_e + \hat{V}_{\mathrm{nn}} + \hat{V}_{\mathrm{ee}} + \hat{V}_{\mathrm{ext}}. \tag{2.2}$$

The terms in the Hamiltonian are the nuclear kinetic energy,

$$\hat{T}_n = -\sum_{i=1}^{M} \frac{\hbar^2}{2m_A} \nabla_A^2, \tag{2.3}$$

the electronic kinetic energy,

$$\hat{T}_e = -\sum_{i=1}^{N} \frac{\hbar^2}{2m_e} \nabla_i^2, \tag{2.4}$$

the nucleus-nucleus interaction energy,

$$\hat{V}_{\mathrm{nn}} = \sum_{A=1}^{M} \sum_{B>A}^{M} \frac{Z_A Z_B e^2}{4\pi\varepsilon_0 R_{\mathrm{AB}}}, \tag{2.5}$$

the electron-electron interaction energy,

$$\hat{V}_{\mathrm{ee}} = \sum_{i=1}^{N} \sum_{j>i}^{N} \frac{e^2}{4\pi\varepsilon_0 r_{\mathrm{ij}}}, \tag{2.6}$$

and the nucleus-electron interaction energy,

$$\hat{V}_{\mathrm{ext}} = -\sum_{i=1}^{N} \sum_{i=1}^{M} \frac{Z_A e^2}{4\pi\varepsilon_0 r_{\mathrm{iA}}}. \tag{2.7}$$

Here, Z_A and m_A are the charge and mass of the A^{th} nucleus, respectively, and m_e is the electron mass. The R_{AB} and r_{iA} are the relative nuclear distance between the A^{th} and B^{th} nucleus and the distance between the i^{th} electron and A^{th} nucleus, respectively. r_{ij} is the relative distance between the i^{th} and j^{th} electrons, $\hbar$ is the Planck constant, and ε_0 is the permittivity of free space constant. The Schrödinger equation is an equation of 3(M+N) degrees of freedom, where M is the number of nuclei, and N the number of electrons. The difficulty in solving the Schrödinger equation arises from the two-body Coulomb interactions, which make the equation inseparable. To obtain a solution approximations must be applied.

2.1.1 The Born-Oppenheimer Approximation

The first of several approximations used to simplify the Schrödinger equation is the Born-Oppenheimer approximation[111]. Since the mass of a nucleus is 1836 times larger than that of an electron, it is assumed that the time scale of nuclei motion are much slower than that for electrons. The nuclei can thus be considered as stationary points in space. The full many-body electronic wave functions can be expressed as a product of single-particle wave functions. This leads to a separation of electronic variables and to the complete diagonalization of the Hamiltonian in terms of single particle molecular orbitals for the system. Correspondingly, the total wave function can be written as a product of electronic and nuclear wave functions,

$$\Psi = \Psi_{\text{electrons}} \times \Psi_{\text{nuclei}}, \tag{2.8}$$

The electronic Hamiltonian then becomes

$$\hat{\mathscr{H}} = \hat{T}_e + \hat{V}_{\text{ee}} + \hat{V}_{\text{ext}}. \tag{2.9}$$

where $\hat{T}_e$, $\hat{V}_{\text{ee}}$ and $\hat{V}_{\text{ext}}$ are given in Eqs. 2.4, 2.6, and 2.7, respectively.

2.1.2 The Hartree-Fock Method

The HF method is served as an essential zeroth-order approximation to the ground state of interacting electrons. As electrons are fermions, they obey the Pauli exclusion principle. This requires the total electronic wave function of electrons to be antisymmetric with respect to the interchange of the coordinates of the electrons; it can thus be written as a Slater determinant. For a 2n-electron system the Slater determinant[112] is given by

$$\Psi(r,s) = \frac{1}{\sqrt{2n!}} \begin{pmatrix} \Psi_1(1)\alpha(1) & \Psi_1(1)\beta(1) & ... & \Psi_n(1)\beta(1) \\ \Psi_1(2)\alpha(2) & \Psi_1(2)\beta(2) & ... & \Psi_n(2)\beta(2) \\ ... & ... & ... & ... \\ \Psi_1(2n)\alpha(2n) & \Psi_1(2n)\beta(2n) & ... & \Psi_n(2n)\beta(2n) \end{pmatrix}; \tag{2.10}$$

The factor $\frac{1}{\sqrt{2n!}}$ ensures that the wave function is normalized. Here, Ψ_i is called molecular orbital (MO), which is a function of the coordinates of i^{th} electron with the spin α (up) or β (down).

In the HF method (and generally, all other methods of determining electronic energy), the total energy for a molecular system is given by[113]

$$E^{\text{total}} = E_{\text{HF}} + E_{\text{NN}}; \tag{2.11}$$

where, E_{HF} is the electronic HF energy and E_{NN} is the inter-nuclear coulombic energy. Applying the variational principle to the total energy[114], one obtains the differential HF equations

$$\hat{F}(r)\Psi_i(r) = \varepsilon(r)\Psi_i(r), \tag{2.12}$$

where $\hat{F}(r)$ is defined as

$$\hat{F}(r) = \hat{\mathscr{H}}^{\text{core}}(r) + \sum_{i=1}^{N} \left(2\hat{J}_i(r) - \hat{K}_i(r)\right); \tag{2.13}$$

$\hat{J}$ is the Coulomb operator and $\hat{K}$ is the exchange operator[114], as will be discussed below.

Substituting the Slater determinant for Ψ and the explicit form of the electronic Hamiltonian operator into Eq. 2.9, gives the following equation for the HF energy,

$$E = 2\sum_{i=1}^{n} H_{\text{ii}} + \sum_{i=1}^{n}\sum_{i=1}^{n} \left(2J_{\text{ij}} - K_{\text{ij}}\right). \tag{2.14}$$

H_{ii} presents the electronic energy of a single electron in the surrounding force field of a nuclear core, and is given by

$$H_{\text{ii}} = \int \Psi_i^*(1)\hat{\mathscr{H}}^{\text{core}}\,\Psi_i(1)d\upsilon; \tag{2.15}$$

where $d\upsilon = dxdydz$. The second and third terms in Eq. 2.14 account for the electron-electron interactions[115]. J_{ij} is the Coulomb integral and it represents the electronic repulsion between the electrons in states Ψ_i and Ψ_j, given by

$$J_{\mathrm{ij}} = \int \Psi_i^*(1)\Psi_i(1)\left(\frac{1}{r_{\mathrm{ij}}}\right)\Psi_j^*(2)\Psi_j(2)d\upsilon_1 d\upsilon_2. \tag{2.16}$$

K_{ij} is referred to as an exchange integral and it accounts for the exchange correlation between electrons of the same spin. It is given by the following equation[115]

$$K_{\mathrm{ij}} = \int \Psi_i^*(1)\Psi_i(2)\left(\frac{1}{r_{\mathrm{ij}}}\right)\Psi_j^*(2)\Psi_j(1)d\upsilon_1 d\upsilon_2 \tag{2.17}$$

2.1.3 Basis Set

Ψ_i can be expanded as a linear combination of basis functions[116],

$$\Psi_i = \sum_{s=1}^{m} C_{\mathrm{si}}\phi_{\mathrm{si}}, \qquad i = 1,2,3,...,m\ (m = \mathrm{MO}); \tag{2.18}$$

where C_{si} are the molecular orbital expansion coefficients and ϕ_{si} denotes the basis functions. The widely used basis functions are Slater-type or Gaussian-type functions[117]. Substituting the basis function expansions into the HF equations (Eq. 2.12), we obtain a total of m $\times$ m equations,

$$\sum_{s=1}^{m} F_{\mathrm{rs}}C_{\mathrm{si}} = \varepsilon \sum_{s=1}^{m} S_{\mathrm{rs}}C_{\mathrm{si}}, \tag{2.19}$$

where the Fock matrix elements F_{rs} are

$$F_{\mathrm{rs}} = \int \phi_r \hat{F}\phi_s d\upsilon, \tag{2.20}$$

and the overlap matrix elements S_{rs} are

$$S_{\mathrm{rs}} = \int \phi_r \phi_s d\upsilon. \tag{2.21}$$

In the Roothaan-Hall approach, the matrix form of algebraic HF equations is

$$\mathbf{FC} = \mathbf{SC}\varepsilon. \tag{2.22}$$

The total HF energy is given by

$$E_{\mathrm{HF}} = 2\sum_{s=1}^{m} F_{\mathrm{rs}} C_{\mathrm{si}} + \sum_{s=1}^{m} S_{\mathrm{rs}} C_{\mathrm{si}} \varepsilon_{\mathrm{ij}} \; r = 1,2,3,...,m, \tag{2.23}$$

where ε_{ij} are the elements of the Lagrange multiplier matrix that are related to the molecular orbital energies. The Roothaan-Hall-Hartree-Fock equations are solved iteratively in a self consistent way. The process starts from initial guess for the molecular orbital MOs Ψ and then the matrix elements F_{rs} and S_{rs} are calculated. The eigenvalues ε_{ij} and eigenfunctions C_{ij} of equation Eq. 2.19 are obtained. This process is repeated until MOs do not change from one step to the next within the convergence criteria. A highly simplified algorithmic flowchart illustrating the method is shown in Fig. 2.1.

2.2 DFT Method

The main weakness of HF approximation is that it only accounts for part of electron-electron interactions. The HF approximation is a type of a mean field theory that treats the exchange interaction between the electrons exactly. DFT is one of the post-HF approaches that includes the electron correlations beyond the HF approximation. The main variable in DFT is the electron density ρ rather than the electronic wave function[118,119].

2.2.1 The Hohenberg-Kohn Theorems

The basis of the DFT was formulated by Hohenberg and Kohn in 1964[120], They stated two theorems. The first Hohenberg-Kohn theorem is an existence theorem that says that any ground state energy of a molecular system is a functional of the ground state electron density, ρ_0, moving in the presence of an external potential $v(r)$,

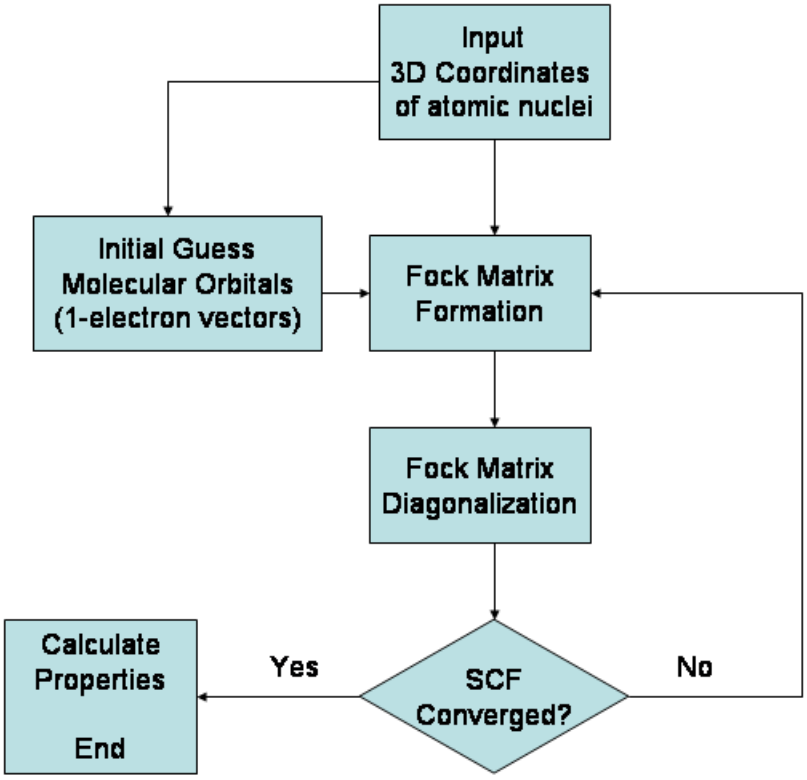

Figure 2.1: Simplified algorithmic flowchart illustrating the Hartree Fock method.

$$E_0 = E[\rho_0]. \tag{2.24}$$

The exact ground state energy functional form is not known. The second Hohenberg-Kohn theorem uses the variational principle that says that any trial electron density gives an energy higher than the true ground state energy calculated with the ground-state electron density function, that is,

$$E[\rho_t] \geqslant E[\rho_0], \tag{2.25}$$

where the E is the electronic energy of the system.
The ground state electronic energy in DFT theory can be written as follows,

$$E_0 = \int \rho_0(r)\upsilon(r)dr + < T\left[\rho_0\right] > + < V_{\mathrm{ee}}\left[\rho_0\right] >, \tag{2.26}$$

where the first term is the potential energy due to electron-nucleus interactions, the second term is the kinetic energy of electrons, and the third term is the potential energy due to electron-electron interactions. The exchange-correlation energy functional E_{xc} is defined as the sum of the kinetic energy deviation from the reference system and the electron-electron repulsion energy deviation from the classical systems

$$E_{\mathrm{xc}}\left[\rho_0\right] = \Delta < T\left[\rho_0\right] > + \Delta < V_{\mathrm{ee}}\left[\rho_0\right] > . \tag{2.27}$$

Writing the functional explicitly in terms of the density built from non-interacting orbitals and applying the variational principle led to the formulation of Kohn-Sham equations [120]

$$\left[-\frac{1}{2}\nabla^2 + \upsilon_{\mathrm{eff}}(r)\right]\psi(r) = \varepsilon_i\psi(r), \tag{2.28}$$

which are similar to HF equations, except that the effective potential is given by

$$\upsilon_{\mathrm{eff}}(r) = \upsilon(r) + \int \frac{\rho\left(r'\right)}{|r-r'|}dr' + v_{xc}, \tag{2.29}$$

an expression that includes an additional exchange-correlation potential, v_{xc}, which is the functional derivative of the exchange-correlation energy functional E_{xc} with respect to the density,

$$v_{\mathrm{xc}}(\mathbf{r}) = \frac{\delta \mathrm{E}_{\mathrm{xc}}[\rho]}{\delta\rho}. \tag{2.30}$$

2.2.2 The Exchange-Correlation Energy Functionals

The Kohn-Sham DFT is an empirical methodology, in a sense that we do not know (and have no way of systematically approaching) the exact functional. However, the functional is universal — it does not depend on the materials being studied. The form of the exchange-

correlation energy functional is unknown, and various approximations are used for E_{xc}, such as local density approximation (LDA), local spin density approximation (LSDA), the generalized gradient approximation (GGA), hybrid functionals and others [109].

The LDA can be considered to be the zeroth order approximation to the semi-classical expansion of the density matrix in terms of the electron density and its derivatives. A typical form of the LDA is:

$$E_{\mathrm{xc}}[\rho] = \int \varepsilon_{\mathrm{xc}}[\rho]\rho(\mathbf{r})d\mathbf{r} \tag{2.31}$$

where, $\varepsilon_{\mathrm{xc}}$ is the exchange correlation energy for a homogeneous electron gas with density ρ [121]. It applies to a uniform electron gas with the nuclei fixed.

A natural progression beyond the LDA is to include the gradient of the density ρ, that is referred to as the generalized gradient approximation (GGA), in which first order gradient terms in the expansion are included [109] in the E_{xc}

$$E_{\mathrm{xc}}[\rho] = \int \rho(\mathbf{r})\varepsilon_{\mathrm{xc}}[\rho, \nabla\rho]d\mathbf{r}. \tag{2.32}$$

In the hybrid methods, the exchange functional is a linear combination of the HF exchange and a functional integral of the density and the density gradient [122]:

$$E^{\mathrm{xc}}_{\mathrm{hybrid}} = c_{\mathrm{HF}}E^{x}_{\mathrm{HF}} + c_{\mathrm{DFT}}E^{\mathrm{xc}}_{\mathrm{DFT}}, \tag{2.33}$$

where, c_{HF} and c_{DFT} are adjustable coefficients.

More recently, empirically dispersion corrected exchange-correlation functionals (DFT-D) were developed and reviewed by Grimme [123,124]. DFT-D methods have been proven accurate for the description of non-covalent interactions and the use of these methods is appearing increasingly more often in the literature [125,126].

2.3 DFT Implementation

All electronic structure calculations in this work were carried out with Vienna *ab initio* Simulation Package (VASP) [127]. VASP is a periodic DFT package for performing *ab initio* quantum-mechanical molecular dynamics (MD) simulations using pseudopotentials or the

projector-augmented wave (PAW) method to describe the electron-ion interactions, and PW basis set to expand the Kohn-Sham orbitals.

2.3.1 Pseudopotentials and the PAW method

Since chemical properties are determined mostly by valence electrons, PAW method approximations are made for the core electron region to overcome the challenges due to the sharp oscillations in the wave functions close to the nuclei. In this method, the strong Coulomb potential of the nucleus and the core electrons are described by an effective ionic potential. Outside a certain cut-off radius, the pseudopotential is constructed to coincide with real potentials and reproduce the correct wave functions (see Fig. 2.2). Reduced number of electrons implemented in this method results in relatively faster calculations for describing the large systems.

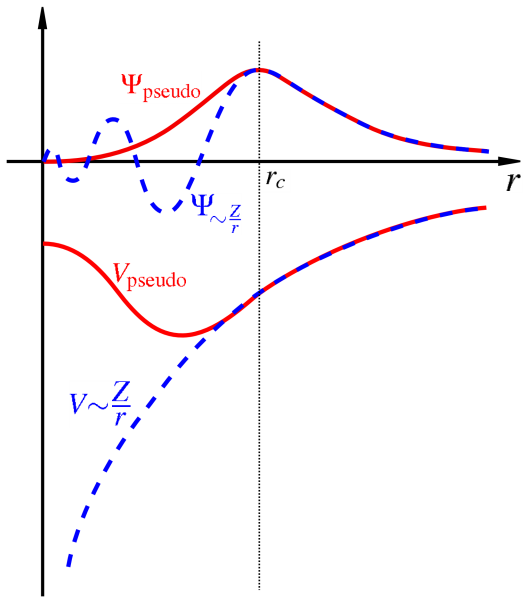

Figure 2.2: Comparison of a wavefunction in the Coulomb potential of the nucleus (blue) to the one in the pseudopotential (red). The real and the pseudo wavefunction and potentials match above a certain cutoff radius, r_c.

2.3.2 Approach to First-Principles QM Study of Periodic Systems

Given the chemical composition and the solid state structure of a periodic system, the aim of first principles computational methods is to calculate its chemical and physical properties as accurately as possible, and at a reasonable computational cost. Therefore, an efficient

computational scheme must be able to manipulate this information economically with regard to CPU time, storage requirements and the number of input and output operations.

Both HF and DFT method can be applied to solid state calculations. For a periodic arrangement of nuclei, the single electron wave functions $\Psi_n(\mathbf{r})$ (where n corresponds to a given atomic level with eigenvalue E_n) can be expressed with the help of Bloch's theorem. That is, in the periodic potential, each atomic wave function, $\Psi_n(r)$, would yield N levels wave of functions $\Psi_n(\mathbf{r}+\mathbf{R})$, where $\mathbf{R}$ is the Bravais lattice vectors such that they satisfy the Bloch condition,

$$\Psi(r+R) = e^{\mathrm{ik}.R}\Psi(r). \tag{2.34}$$

Given the above equation, the single electron wave function can be written as

$$\Psi_{\mathrm{nk}}(r) = \sum_k e^{\mathrm{ik}.R}\phi(r+R), \tag{2.35}$$

where k ranges through the N values in the first Brillouin zone, and $\phi(\mathbf{r}+\mathbf{R})$ can be atomic or molecular spin orbital. The atomic orbital can then be expanded in terms of a linear combination of N basis functions. This approximation is referred to as Linear combination of atomic orbitals (LCAO) method in solid state[128]. The substitution of expanded wave function into the Schrödinger equation results in HF or KS like eigenvalue-eigenfunction equations depending on the level of approximation used[117].

2.3.3 Sampling the Brillouin Zone

Finite integrals over the Brillouin zone in reciprocal space are necessary for obtaining different electronic structure properties. These integrals are numerically calculated at finite number of k-points in the Brillouin Zone. Various methods have been developed to obtain accurate description of the systems. In this thesis, minimum energy structures were determined using Monkhorst Pack k point sampling grids with $3\times3\times1$ k points[129], tested to be sufficient to obtain an accurate electronic potential and total energy.

2.3.4 Computational Details

The Kohn-Sham one-electron wave functions were expanded in a plane wave basis set up to an energy cutoff of 400 eV. Exchange-correlation effects were incorporated within the

generalized gradient approximation (GGA), using the exchange-correlation functional by Perdew, Burke and Ernzerhof (PBE)[130]. This functional consistently describes the properties of water at metal surfaces[125,131,132]. Geometry optimization studies were terminated when all forces on ions were less than 0.03 (or 0.05) eV Å^{-1}.

Chapter 3

Modelling the Local Potential at Pt Nanoparticles in Polymer Electrolyte Membranes

As for the first step of our theoretical approach presented in Fig. 1.9 to understand the role of PITM on membrane degradation, in this chapter we present a physical analytical model for the potential distribution at Pt nanodeposits in a polymer electrolyte membrane. As discussed in section 1.2, experimental studies have shown that solid deposits of Pt in the PEM play an important role in radical-initiated membrane degradation. Surface reactions at Pt particles facilitate the formation of ionomer-attacking species. The net radical balance depends on local equilibrium conditions at Pt nanodeposits in the PEM, specifically, their equivalent local electrode potential. Our model utilizes a continuum description of crossover fluxes of reactant gases, coupled with the kinetics of electrochemical surface reactions at Pt nanodeposits to calculate the potential distribution. The local potential is a function of the PEM structure and composition, which is determined by PEM thickness, concentrations of H_2 and O_2, as well as the size and density distribution of Pt particles. Model results compare well with experimental data for the potential distribution in PEMs.

3.1 Introduction

Understanding the impact of PITM on the chemical degradation of the PEM involves a complex phenomenology of local conditions and structure of the PEM, as well as structure-dependent transport and reaction processes. The balance of competing processes depends on local conditions such as temperature and relative humidity as well as the structure and

local chemical composition of the PEM. The local chemical composition of the PEM is determined by pH and by mole fractions of H_2 and O_2 provided at opposite membrane sides. Local values of H_2 and O_2 concentrations can be calculated for given transport properties, composition and thickness of the PEM. The same conditions also determine the size, shape and density distribution of Pt deposits in the PEM[89,133–135]. On the other hand, the formation of PITM has a feedback effect on concentrations of H_2 and O_2 as well as membrane humidification[81]. Moreover, the rates of catalytic surface processes depend on size and shape of Pt nanoparticle deposits[66,135–137].

The local open circuit potential (OCP) of a Pt nanoparticle, considered as a nanoelectrode in the PEM, is determined by the conditions listed above. Liu and Zuckerbrod have measured the OCP distribution at a Pt nanoprobe in the membrane, with H_2 and air provided at opposite membrane sides[74]. They have observed a step-like potential profile. The local electrode potential in the region close to the anode was found near 0 V vs. RHE. In the region near the cathode, the OCP was found to attain values between 0.8 V and 1.0 V. Takaichi *et al.*[138] have measured the OCP distribution determined by H_2 and O_2 permeation in the membrane. They have observed a change in the step position at different O_2 partial pressure and relative humidity[139].

Understanding the problem of electrostatic potential at isolated metallic nanoparticles in an electrolyte is fundamentally interesting and of broader practical impact. Specifically, the problem of Pt nanodeposits in polymer electrolyte membranes has received significant attention in recent years. However, to the best of our knowledge only one modelling work has been devoted to this topic[140]. Atrazhev *et al.* have developed a model to predict the potential distribution at a single Pt particle in the PEM[140]. Their model employs an “ad hoc" formulation of the problem, in which the surface concentrations of reactant gases, H_2 and O_2, at a spherical Pt particle are obtained as functions of particle position. The relations are substituted in the Butler-Volmer equations and the charge balance condition is applied to numerically calculate the local mixed potential at the particle. Their model, however, suffers from physically inconsistent relations obtained for the current densities of hydrogen oxidation reaction (HOR) and oxygen reduction reaction (ORR), i.e. Eqs (36) and (37) in their paper[140]. As discussed in their paper, at the position of the potential step, both HOR and ORR are controlled by diffusion of reactant gases to the particle surface; thus, at this position, each of the current densities must be independent of the particle potential. However, in their relevant equations the dependency still exists. In addition, the implementation and parameterization of HOR and ORR kinetics employed in their model are incompatible with experimental data[141–143].

In this chapter, we present a rigorous and self-consistent formulation of the problem which results in a physical-analytical model of the mixed-potential distribution at Pt nanodeposits in the PEM. The model employs continuum diffusion for the crossover of reactant gases, H_2 and O_2, coupled with local electrochemical reactions at the surface of Pt nanoparticles. The analytical solution gives the shapes of the reactant concentrations and of the potential profile in terms of experimental parameters, including the relative concentration of H_2 and O_2 at the PEM boundaries, mass transfer coefficients, kinetic parameters of surface reactions at Pt, and size and density of Pt particles in the PEM. Model outcomes are compared to experimental measurements of the OCP at Pt nanodeposits in the membrane[74,139].

3.2 The Model

The model incorporates a two-scale description of transport and reaction processes in the membrane, as illustrated in Fig. 3.1. At the macroscale, one-dimensional (1D) diffusion governs the distribution of redox species, i.e., H_2 and O_2, along the thickness variable x. Even though we do not consider the membrane embedded in the fuel cell configuration, we refer to the side at which hydrogen is supplied as the anode and the side at which oxygen is provided as the cathode. Concentrations of hydrogen and oxygen in the PEM are $c_{H_2}(x)$ and $c_{O_2}(x)$. The concentrations at the PEM boundaries are $c^0_{H_2}$ at $x = 0$ (anode side) and $c^0_{O_2}$ at $x = l$ (cathode side). At the nanoscale, the hydrogen oxidation reaction (HOR), $H_2 \leftrightarrow 2H^+ + 2e^-$, and the oxygen reduction reaction (ORR), $O_2 + 4H^+ + 4e^- \rightarrow 2H_2O$ proceed at the surface of Pt nanoparticles, which we assume spherical. As Pt nanoparticles are not connected to an electron source/sink, the resulting OCP must fulfill a condition that the rates of HOR and ORR processes are balanced at the particle level.

As shown in Fig. 3.2, four regimes can be distinguished to describe the mixed reaction kinetics at the surface of Pt nanodeposits in the PEM. The distinction is based on the comparison of diffusion and kinetically-limited current densities of HOR and ORR at the spherical Pt nanoelectrode. The diffusion limited current density of the HOR and the ORR can be obtained by solving the spherically symmetrical diffusion equation under steady state conditions,[144]

$$\frac{1}{r^2}\frac{d}{\mathrm{dr}}\left(r^2\frac{\mathrm{dc}_{H_2,O_2}}{\mathrm{dr}}\right) = 0 \tag{3.1}$$

where r is the distance from the center of the particle, subject to the following boundary conditions,

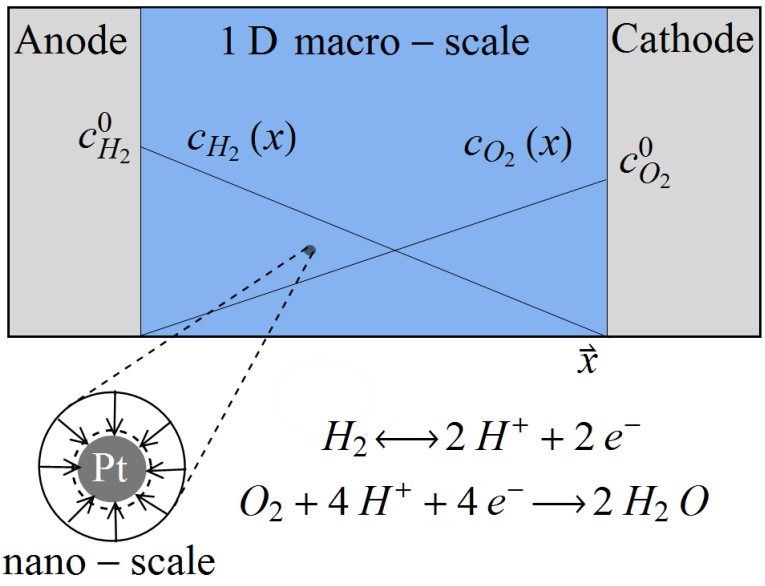

Figure 3.1: Model representation of a Pt nanoparticle in the membrane. The model assumes macroscale diffusion of H_2 and O_2 from the opposite membrane boundaries, coupled with local diffusion around Pt nanodeposits and reactions (HOR and ORR) at the Pt surface.

$$j_{\mathrm{HOR}} = 2FD^{\mathrm{nano}}_{H_2} \left.\frac{\mathrm{dc}_{H_2}}{\mathrm{dr}}\right|_{r=r_0}, \tag{3.2}$$

$$j_{\mathrm{ORR}} = 4FD^{\mathrm{nano}}_{O_2} \left.\frac{\mathrm{dc}_{O_2}}{\mathrm{dr}}\right|_{r=r_0}, \tag{3.3}$$

$$c^{\infty}_{H_2,O_2} = c^{\mathrm{bulk}}_{H_2,O_2}(x). \tag{3.4}$$

The diffusion limited current density of the HOR is then given by

$$j^{\mathrm{d}}_{\mathrm{HOR}} = 2Fc_{H_2}(x)\frac{D^{\mathrm{nano}}_{H_2}}{r_0}, \tag{3.5}$$

and that of the ORR is

$$j^{\mathrm{d}}_{\mathrm{ORR}} = 4Fc_{O_2}(x)\frac{D^{\mathrm{nano}}_{O_2}}{r_0}, \tag{3.6}$$

where F is the Faraday constant, r_0 is the Pt particle radius, and $D^{\mathrm{nano}}_{H_2}$ and $D^{\mathrm{nano}}_{O_2}$ are the diffusion coefficients of H_2 and O_2 at the nanoscale, respectively.

For the faradaic current densities of HOR and ORR at the particle surface, we use expressions in the form of the Butler-Volmer equation, i.e.,

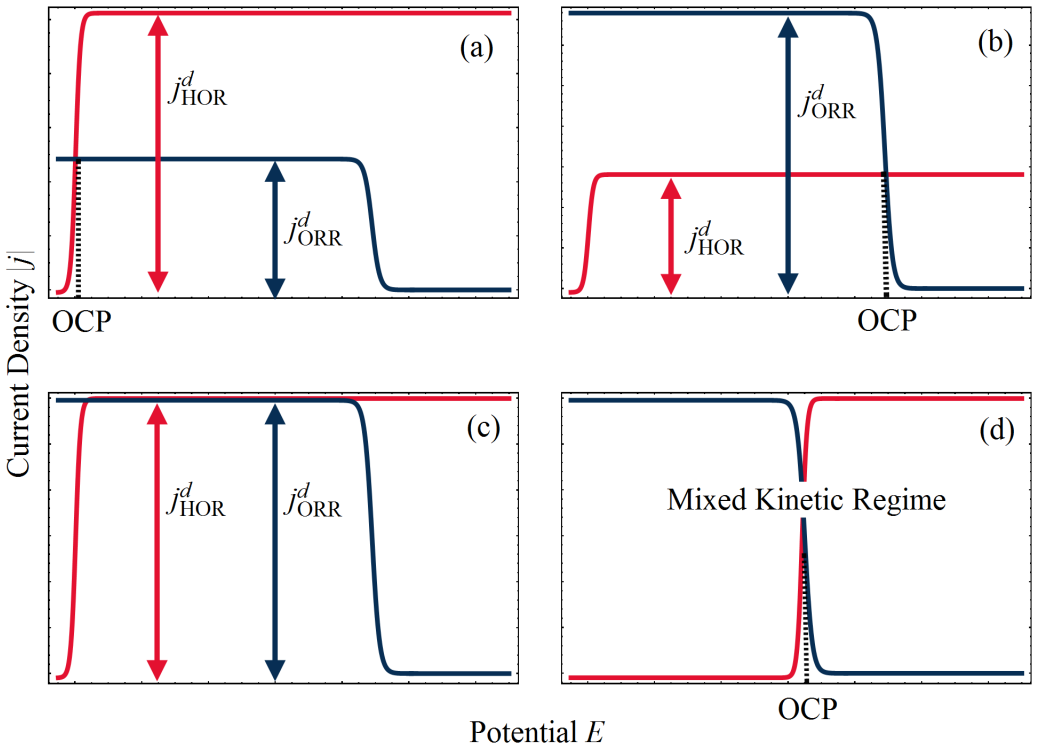

Figure 3.2: Schematic representation of HOR and ORR polarization curves, indicating open circuit potential (OCP). Plots (a) and (b) correspond to mixed diffusion-kinetic regimes for HOR and ORR. For the situation depicted in (c) both reactions are limited by local diffusion, whereas in (d) both reactions are controlled by the kinetics of surface reactions.

$$j_{\mathrm{HOR}} = j^0_{\mathrm{HOR}} \left(\left(\frac{c^s_{H_2}(x)}{C_{\mathrm{ref}}} \right) \exp\left[\frac{\alpha^a_{\mathrm{HOR}}}{b} E(x) \right] - \exp\left[-\frac{\alpha^c_{\mathrm{HOR}}}{b} E(x) \right] \right), \tag{3.7}$$

and

$$j_{\mathrm{ORR}} = j^0_{\mathrm{ORR}} \left(\left(\frac{c^s_{O_2}(x)}{C_{\mathrm{ref}}} \right) \exp\left[-\frac{\alpha^c_{\mathrm{ORR}}}{b} \left(E(x) - E^{\mathrm{eq}} \right) \right] - \exp\left[\frac{\alpha^a_{\mathrm{ORR}}}{b} \left(E(x) - E^{\mathrm{eq}} \right) \right] \right), \tag{3.8}$$

where $b = \frac{RT}{F}$, $c^s_{H_2}$ and $c^s_{O_2}$ are surface concentrations of H_2 and O_2, respectively, and $C_{Ref} = 40.88 \times 10^{-6} mol/cm^3$ is a reference concentration[145]. It corresponds to the O_2 concentration at standard conditions. α^a and α^c are the anodic and cathodic electron transfer coefficients, j^0_{HOR} and j^0_{ORR} are the exchange current densities of HOR and ORR, and E^{eq} is the equilibrium potential of ORR (vs. RHE). R and T are the gas constant and temperature, respectively.

For a Pt nanodeposit at position x, one of four possible scenarios will determine the local value of the OCP, $E(x)$: (1) If $j^d_{\mathrm{HOR}} > j^d_{\mathrm{ORR}}$, then the HOR is controlled by reaction kinetics and the ORR is diffusion-limited, as shown in Fig. 3.2 (a); in this case, $E(x)$ remains close to the equilibrium potential of the HOR. (2) If $j^d_{\mathrm{HOR}} < j^d_{\mathrm{ORR}}$, then the HOR is diffusion-limited and the ORR is kinetically controlled; in this case, $E(x)$ shifts towards the equilibrium potential of the ORR, as illustrated in Fig. 3.2 (b). (3) The transition between the two cases occurs at the position where $j^d_{\mathrm{HOR}} = j^d_{\mathrm{ORR}}$, as shown in Fig. 3.2 (c); in this regime, the current density at the particle is independent of $E(x)$; it corresponds to a step-like change in $E(x)$ at a position x_0. From the condition of equal diffusion-limited current densities in this regime, we will determine the value of x_0. (4) The last possible scenario is that both reactions are controlled kinetically, as depicted in Fig. 3.2 (d); in this case, $E(x)$ is found from the condition $j_{\mathrm{HOR}} = j_{\mathrm{ORR}}$, using Eqs. 3.7 and 3.8.

Following the distinction of different kinetic regimes, governing the local current at the nanoparticle surface, the PEM can be divided into two spatial regions, viz. an anodic region at $x < x_0$, in which $j^d_{\mathrm{HOR}} > j^d_{\mathrm{ORR}}$ and a cathodic region at $x > x_0$, in which $j^d_{\mathrm{HOR}} < j^d_{\mathrm{ORR}}$. In the anodic region, the HOR current is kinetically controlled, whereas the ORR is usually in the diffusion-limited regime. In the cathodic region, the ORR is kinetically controlled, whereas the HOR is usually in the diffusion-limited regime.

If a reaction at the Pt surface is kinetically controlled, the surface concentration of redox species will be equal to the bulk concentrations, i.e. $c^s_{H_2} = c_{H_2}(x)$ in the anodic region and $c^s_{O_2} = c_{O_2}(x)$ in the cathodic membrane region. For diffusion-limited reactions, we will assume zero surface concentration of the transport-limited reactant, i.e. $c^s_{O_2} \approx 0$ in the anodic region and $c^s_{H_2} \approx 0$ in the cathodic region. As we are interested in obtaining analytical solutions for the potential profile $E(x)$, we will employ modified forms of the Butler-Volmer expressions in Eqs. 3.7 and 3.8, given by

$$j_{\mathrm{HOR}} = 2 j^0_{\mathrm{HOR}} \left(\frac{c_{H_2}(x)}{C_{\mathrm{ref}}} \right) \sinh \left[\frac{1}{2b} E(x) \right], \tag{3.9}$$

and

$$j_{\mathrm{ORR}} = j^0_{\mathrm{ORR}} \left(\frac{c_{O_2}(x)}{C_{\mathrm{ref}}} \right) \exp \left[-\frac{1}{b} \left(E(x) - E^{\mathrm{eq}} \right) \right]. \tag{3.10}$$

In Eqs. 3.9 and 3.10, we assume $\alpha^a_{\mathrm{HOR}} = \alpha^c_{\mathrm{HOR}} = \frac{1}{2}$ (see Ref. [141]) and $\alpha^c_{\mathrm{ORR}} = 1$ (see Refs [142,143]). In Eq. 3.9 the sinh-expression for the faradaic current density of the HOR represents a common interpolation [146]. It allows for a continuous description of the HOR rate in the limit of small overpotential, $E(x) \leq b/3$, where $c_{H_2}(x) \approx C_{ref}$, and high overpo-

tential, $E(x) \geq 3b$, where $2\sinh[E(x)/2b] \approx \exp[E(x)/2b]$. The single term BV-equation for the ORR in Eq. 3.10 is the standard form, accounting for the irreversible kinetics of the ORR.

We apply the charge balance condition for anodic and cathodic regions in the PEM and at the transition between these regions, to obtain analytical relations for the potential profile. In the anodic region, i.e. for $x < x_0$, we have

$$j_{\mathrm{HOR}} = j^{\mathrm{d}}_{\mathrm{ORR}}. \tag{3.11}$$

Inserting Eqs. 3.6 and 3.9 and solving for $E(x)$ results in

$$E(x) = 2b\,\sinh^{-1}\left[\frac{1}{2}\frac{c_{O_2}(x)}{c_{H_2}(x)}\frac{J^{\mathrm{d}}_{\mathrm{ORR}}}{j^{0}_{\mathrm{HOR}}}\right] \tag{3.12}$$

with

$$J^{\mathrm{d}}_{\mathrm{ORR}} = 4FC_{\mathrm{ref}}\frac{D^{\mathrm{nano}}_{O_2}}{r_0}. \tag{3.13}$$

Similarly, in the cathodic region of the PEM, i.e. for $x > x_0$, we have

$$j_{\mathrm{ORR}} = j^{\mathrm{d}}_{\mathrm{HOR}}. \tag{3.14}$$

In this case, using Eqs. 3.5 and 3.10 and solving for $E(x)$, gives

$$E(x) = E^{\mathrm{eq}} - b\ln\left[\frac{c_{H_2}(x)}{c_{O_2}(x)}\frac{J^{\mathrm{d}}_{\mathrm{HOR}}}{j^{0}_{\mathrm{ORR}}}\right] \tag{3.15}$$

with

$$J^{\mathrm{d}}_{\mathrm{HOR}} = 2FC_{\mathrm{ref}}\frac{D^{\mathrm{nano}}_{H_2}}{r_0}. \tag{3.16}$$

At $x = x_0$, both the current densities of HOR and ORR are controlled by diffusion and, therefore,

$$j^{\mathrm{d}}_{\mathrm{HOR}} = j^{\mathrm{d}}_{\mathrm{ORR}}, \tag{3.17}$$

which leads to a unique relation between the ratio of the bulk concentrations of the reactant gases at x_0, and the diffusion coefficients,

$$2c_{O_2}(x_0)\,D^{\mathrm{nano}}_{O_2} = c_{H_2}(x_0)\,D^{\mathrm{nano}}_{H_2}. \tag{3.18}$$

Eq. 3.18 can be solved to find x_0 whence the distributions $c_{O_2}(x)$ and $c_{H_2}(x)$ are known. The last possible case is when both current densities of HOR and ORR are controlled by reaction kinetics,

$$j_{\mathrm{HOR}} = j_{\mathrm{ORR}}. \tag{3.19}$$

In this scenario, the potential profile is obtained using Eqs. 3.9 and 3.10, giving,

$$E(x) = 2b \ln \left[\frac{12^{1/3} + \left(\kappa(x) + \sqrt{(\kappa(x))^2 - 12} \right)^{2/3}}{18^{1/3} \left(\kappa(x) + \sqrt{(\kappa(x))^2 - 12} \right)^{1/3}} \right], \tag{3.20}$$

where

$$\kappa(x) = 9 \left(\frac{c_{O_2}(x)}{c_{H_2}(x)} \frac{j^0_{\mathrm{ORR}}}{j^0_{\mathrm{HOR}}} \right) \exp \left[\frac{E^{\mathrm{eq}}}{b} \right]. \tag{3.21}$$

Eqs. 3.12, 3.15 and 3.20 allow expressing the potential profile in the PEM through the distribution of concentrations, $c_{H_2}(x)$ and $c_{O_2}(x)$. In order to obtain the concentrations, we must solve 1D diffusion equations for hydrogen and oxygen in the distinct PEM regions.

We define $\xi = \frac{x}{l}$ as the dimensionless coordinate along the membrane thickness and $\xi_0 = \frac{x_0}{l}$ as the dimensionless position of the potential step. In the anodic region ($\xi < \xi_0$), the reaction-diffusion equation for O_2 is

$$\frac{d^2 c_{O_2}(\xi)}{d\xi^2} = \Lambda^{-2} c_{O_2}(\xi), \tag{3.22}$$

and that for H_2, using Eq. 3.11, is

$$\frac{d^2 c_{H_2}(\xi)}{d\xi^2} = \frac{2\Lambda^{-2}}{\delta^2} c_{O_2}(\xi), \tag{3.23}$$

with

$$\delta^2 = \frac{D^{\mathrm{macro}}_{H_2}}{D^{\mathrm{macro}}_{O_2}} \tag{3.24}$$

and

$$\Lambda = \frac{1}{l} \left(4\pi r_0 n_{\mathrm{Pt}} \left(\frac{D^{\mathrm{nano}}_{O_2}}{D^{\mathrm{macro}}_{O_2}} \right) \right)^{-1/2}, \tag{3.25}$$

where n_{Pt} is the number of Pt particles per unit PEM volume. The product Λl represents the dimensional reaction penetration depth of O_2. In the dilute limit of Pt particle distributions $\Lambda \gg 1$, and in the dense limit $\Lambda \ll 1$.

The diffusion coefficients at nanoscale and macroscale are distinguished as the structure and effective transport resistance of the medium is different at the two scales. The macroscale diffusion coefficient corresponds to diffusion in a random composite medium, with randomly mixed resistances due to polymer and water-filled domains. Nanoscale diffusion coefficients, on the other hand, approach the values for water. Therefore, the macroscopic diffusion coefficient will be smaller than the value in water by a factor that incorporates percolation effects. We consider this value as 10 because the diffusion coefficient of H_2 and O_2 in water[147] is one order of magnitude larger than its value in Nafion®. This ratio is included in Eq. 3.25.

Due to large overpotential for the ORR at the anode, we assume that O_2 is completely used up at ξ=0. The boundary conditions of Eqs. 3.22 and 3.23 are given by

$$c_{O_2}(\xi = 0) = 0, c_{O_2}(\xi_0) = c_{O_2}^{\xi_0}, \tag{3.26}$$

and

$$c_{H_2}(\xi = 0) = c_{H_2}^0, c_{H_2}(\xi_0) = c_{H_2}^{\xi_0}. \tag{3.27}$$

The solution of Eqs. 3.22 and 3.23 subject to the boundary conditions 3.26 and 3.27 are as follows,

$$c_{O_2}(\xi) = c_{O_2}^{\xi_0} \frac{\sinh(\Lambda^{-1}\xi)}{\sinh(\Lambda^{-1}\xi_0)}, \tag{3.28}$$

$$c_{H_2}(\xi) = \frac{2}{\delta^2} c_{O_2}^{\xi_0} \frac{\sinh(\Lambda^{-1}\xi)}{\sinh(\Lambda^{-1}\xi_0)} + \left(c_{H_2}^{\xi_0} - c_{H_2}^0 - \frac{2}{\delta^2} c_{O_2}^{\xi_0} \right) \frac{\xi}{\xi_0} + c_{H_2}^0. \tag{3.29}$$

Similarly, in the cathodic region of the PEM ($\xi > \xi_0$), the reaction-diffusion equation of H_2 is

$$\frac{d^2 c_{H_2}(\xi)}{d\xi^2} = \Lambda^{-2} c_{H_2}(\xi), \tag{3.30}$$

and that of O_2, using Eq. 3.14, is

$$\frac{d^2 c_{O_2}(\xi)}{d\xi^2} = \frac{\Lambda^{-2}\delta^2}{2} c_{H_2}(\xi); \tag{3.31}$$

here, for simplicity, we assume $\left(\frac{D_{O_2}^{\text{nano}}}{D_{O_2}^{\text{macro}}}\right) = \left(\frac{D_{H_2}^{\text{nano}}}{D_{H_2}^{\text{macro}}}\right)$, so that Λ is the same as defined in Eq. 3.25. The boundary conditions are

$$c_{H_2}(\xi_0) = c_{H_2}^{\xi_0}, c_{H_2}(\xi = 1) = 0, \tag{3.32}$$

and

$$c_{O_2}(\xi_0) = c_{O_2}^{\xi_0}, c_{O_2}(\xi = 1) = c_{O_2}^{0}. \tag{3.33}$$

The solutions of Eqs. 3.30 and 3.31 are

$$c_{H_2}(\xi) = c_{H_2}^{\xi_0} \frac{\sinh(\Lambda^{-1}(\xi - 1))}{\sinh\left(\Lambda^{-1}(\xi_0 - 1)\right)}, \tag{3.34}$$

$$c_{O_2}(\xi) = \frac{\delta^2}{2} c_{H_2}^{\xi_0} \frac{\sinh(\Lambda^{-1}(\xi - 1))}{\sinh\left(\Lambda^{-1}(\xi_0 - 1)\right)} + \left(c_{O_2}^{\xi_0} - c_{O_2}^{0} - \frac{\delta^2}{2} c_{H_2}^{\xi_0}\right) \frac{\xi - 1}{\xi_0 - 1} + c_{O_2}^{0}. \tag{3.35}$$

To obtain the equations for $c_{H_2}^{\xi_0}$ and $c_{O_2}^{\xi_0}$, we apply the continuity condition at $\xi = \xi_0$,

$$\frac{dc_{H_2}(\xi)}{d\xi}|_{\xi=\xi_0^-} = \frac{dc_{H_2}(\xi)}{d\xi}|_{\xi=\xi_0^+}; \frac{dc_{O_2}(\xi)}{d\xi}|_{\xi=\xi_0^-} = \frac{dc_{O_2}(\xi)}{d\xi}|_{\xi=\xi_0^+}. \tag{3.36}$$

Inserting Eqs. 3.29 and 3.34, we obtain

$$\left(\frac{2\Lambda^{-1}\xi_0}{\delta^2}\coth\left(\Lambda^{-1}\xi_0\right) - \frac{2}{\delta^2}\right) c_{O_2}^{\xi_0} = \left(\Lambda^{-1}\xi_0 \coth\left(\Lambda^{-1}(\xi_0 - 1)\right) - 1\right) c_{H_2}^{\xi_0} + c_{H_2}^{0}. \tag{3.37}$$

Similarly, by inserting Eqs. 3.28 and 3.35 into Eq. 3.36, we obtain

$$\left(\frac{\Lambda^{-1}\delta^2(\xi_0 - 1)}{2}\coth\left(\Lambda^{-1}(\xi_0 - 1)\right) - \frac{\delta^2}{2}\right) c_{H_2}^{\xi_0} = \left(\Lambda^{-1}(\xi_0 - 1)\coth\left(\Lambda^{-1}\xi_0\right) - 1\right) c_{O_2}^{\xi_0} + c_{O_2}^{0}. \tag{3.38}$$

The solution for Eqs. 3.37 and 3.38 for $c_{H_2}^{\xi_0}$ and $c_{O_2}^{\xi_0}$ can be obtained from following steps: Rewriting Eqs. 3.37 and 3.38,

$$\mathscr{R} c_{H_2}^{\xi_0} = \mathscr{S} c_{O_2}^{\xi_0} + \mathscr{T}\ ;\ \mathscr{U} c_{H_2}^{\xi_0} = \mathscr{V} c_{O_2}^{\xi_0} + \mathscr{W} \tag{3.39}$$

$c_{H_2}^{\xi_0}$ and $c_{O_2}^{\xi_0}$ are given by:

$$c_{H_2}^{\xi_0} = \frac{\mathscr{S}\mathscr{W} - \mathscr{T}\mathscr{V}}{\mathscr{U}\mathscr{S} - \mathscr{R}\mathscr{V}}, \; ; \; c_{O_2}^{\xi_0} = \frac{\mathscr{R}\mathscr{W} - \mathscr{T}\mathscr{U}}{\mathscr{U}\mathscr{S} - \mathscr{R}\mathscr{V}}. \tag{3.40}$$

where,

$$\mathscr{R} = \Lambda^{-1}\xi_0 \coth\left[\Lambda^{-1}(\xi_0 - 1)\right] - 1, \tag{3.41}$$

$$\mathscr{S} = \frac{2\Lambda^{-1}\xi_0}{\delta^2}\coth\left[\Lambda^{-1}\xi_0\right] - \frac{2}{\delta^2}, \tag{3.42}$$

$$\mathscr{T} = -c_{H_2}^0, \tag{3.43}$$

$$\mathscr{U} = \left[\frac{\delta^2\Lambda^{-1}(\xi_0 - 1)}{2}\coth\left[\Lambda^{-1}(\xi_0 - 1)\right] - \frac{\delta^2}{2}\right], \tag{3.44}$$

$$\mathscr{V} = (\xi_0 - 1)\Lambda^{-1}\coth\left[\Lambda^{-1}\xi_0\right] - 1, \tag{3.45}$$

$$\mathscr{W} = c_{O_2}^0. \tag{3.46}$$

In the dilute limit of Pt particles, as $\Lambda \gg 1$, $c_{H_2}^{\xi_0}$=$c_{H_2}^0$(1-ξ_0) and $c_{O_2}^{\xi_0}$=$c_{O_2}^0\xi_0$. Substituting the relations for $c_{H_2}^{\xi_0}$ and $c_{O_2}^{\xi_0}$, into Eq. 3.18 the position of the potential step is found as

$$\xi_0 = \frac{1}{1 + \frac{2}{\delta^2}\frac{c_{O_2}^0}{c_{H_2}^0}}. \tag{3.47}$$

It indicates that as the uniform distribution of particles is assumed, ξ_0 is independent of the size and density of particles and only depends on the relevant concentrations of reactant gases at boundaries and the ratio of diffusion coefficients. This result is independent of the particle shape. The effect of particle shape appears in the form of the diffusion limited current densities and as well in Λ. ξ_0 is obtained by applying the charge balance condition for the limiting current densities of HOR and ORR as given in Eq. 13. In this equation, as the parameters affecting the particle shape are assumed to be the same for HOR and ORR, they cancel out from both sides of the equation for any particle shape. In addition, for a uniform distribution the step position is independent of Λ, hence of the particle shape.

3.2.1 Model Parameters

Physical properties and constants are listed in Table 3.1. The adopted values for the macroscale diffusion coefficients correspond to H_2 and O_2 diffusion in Nafion® 117, evaluated at 100% RH and 60 °C[148]. Exchange current densities of the HOR and ORR have been extracted from Refs. (136) and (130), respectively.

As the molar concentrations of H_2 and O_2 in Nafion® are reasonably small for the relevant partial pressures, we use Henry's law to relate H_2 and O_2 concentrations at the membrane boundaries to external partial pressures,

$$c^0_{H_2} = H_{H_2} p^0_{H_2} \; ; \; c^0_{O_2} = H_{O_2} p^0_{O_2}. \tag{3.48}$$

with Henry's law constants H_{H_2} and H_{O_2} in Nafion®.
Substituting Eq. 3.48 into Eq. 3.47, we obtain

$$x_0 = \frac{l}{1 + 2\beta \frac{p^0_{O_2}}{p^0_{H_2}}}, \tag{3.49}$$

where,

$$\beta = \frac{D^{\text{macro}}_{O_2} H_{O_2}}{D^{\text{macro}}_{H_2} H_{H_2}}. \tag{3.50}$$

The value of β used in this work is taken from Ref. (25). It is reported as 0.38 ± 0.05, evaluated experimentally in permeability tests of crossover hydrogen and oxygen at 100% RH and 65 °C[89].

The evaluated ranges of parameters are listed in Table 3.2 The ranges correspond to values of parameters reported in the literature. As a baseline for parametric studies, we consider a membrane with $l = 50\ \mu m$ in which particles with $r_0 = 150\ nm$ are uniformly distributed with $n_{Pt} = 5 \times 10^9\ cm^{-3}$. The range of n_{Pt} is estimated based on the amount of Pt in the membrane. Results of electron microscopy-energy dispersive spectroscopy analysis have been used to quantify the amount of Pt transported from cathode to the membrane[89]. This study estimates that $\approx 13\%$ of Pt in the cathode is transported into the membrane following 3000 potential cycles. This amount corresponds to $\approx 0.38\ mg$ Pt, if we consider a Pt loading of 0.1 $mg\ cm^{-2}$ for a $5 \times 5\ cm$ membrane. Equivalently, this amount results in a uniform distribution of Pt particles with $r_0 = 150\ nm$ and $n_{Pt} \approx 10^{10}\ cm^{-3}$ across a membrane with $l = 50\ \mu m$.

Table 3.1: Physical parameters, symbols and values

Description	Value	Ref.
Faraday constant, F	96485 C/mol	
Gas constant, R	8.314 J/mol K	
Temperature, T	333 K	
ORR equilibrium potential, E^{eq}	1.23 V	
Reference H_2 molar concentration, C_{ref}	40.88 $\times 10^{-6}$ mol/cm^3	145
Reference O_2 molar concentration, C_{ref}	40.88 $\times 10^{-6}$ mol/cm^3	145
H_2 diffusion coefficient in Nafion®, $D^{macro}_{H_2}$	1.2 $\times$ 10^{-5} cm^2/s	148
O_2 diffusion coefficient in Nafion®, $D^{macro}_{O_2}$	2.1 $\times$ 10^{-6} cm^2/s	148
HOR exchange current density, j^0_{HOR}	0.8 $\times$ 10^{-3} A/cm^2	149
ORR exchange current density, j^0_{ORR}	5.4 $\times$ 10^{-11} A/cm^2	143
Transfer coefficients for HOR, α^a_{HOR}= α^c_{HOR}	1/2	141
Transfer coefficient for ORR, α^c_{ORR}	1	142

Table 3.2: Ranges for parameters

Description	Value
H_2 pressure at membrane|anode, $p^0_{H_2}$, kPa	21-125
O_2 pressure at membrane|cathode, $p^0_{O_2}$, kPa	21-125
Particle radius, r_0 , nm	50-5000
Membrane thickness, l , μm	25-200
Particle density, n_{Pt} , cm^{-3}	10^7-10^{10}

3.3 Results and Discussion

Fig. 3.3 shows the concentration profiles of H_2 and O_2 across the PEM and the step position, ξ_0, in dilute and dense limit of Pt particles. As shown, the position of ξ_0, given by Eq. 3.47 (or 3.49), depends on the relative concentrations of reactant gases at the membrane boundaries. The step shifts towards the cathode as $p^0_{H_2}$ increases relative to $p^0_{O_2}$ and vice versa. In the uniform particle distribution regime, ξ_0 is independent of Λ, as can be seen from Eq. 3.49.

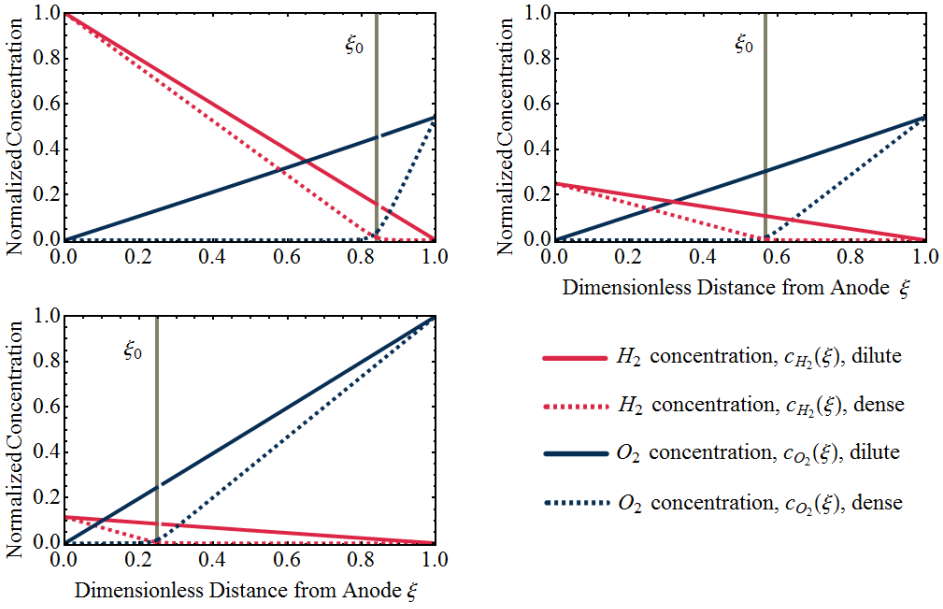

Figure 3.3: Analytical solution of concentration profiles of H_2 and O_2 in dilute limit and dense limit of uniformly distributed Pt deposits for various relative concentrations of H_2 and O_2 at the PEM boundaries. The position of potential step position is indicated as vertical dashed line which is independent of particle density.

As shown in Fig. 3.3, in the dilute limit of Pt particles, as $\Lambda \gg 1$, the concentration profiles are linear, given by $c_{H_2}(\xi)=c^0_{H_2}(1-\xi)$ and $c_{O_2}(\xi)=c^0_{O_2}\xi$ (see Eqs. 3.28, 3.29, 3.34 and 3.35). As $\Lambda \to 1$ concentration profiles deviate from linear curves. According to Eq. 3.22 and 3.23, nonlinearity occurs when the local rate of reactant consumption is of similar order of magnitude as the rate of reactant flux. In dense limit, as $\Lambda \ll 1$, both concentrations approach to zero at ξ_0 which is expected as a trivial solution to Eq. 3.18.

For the case of a dense Pt band formed in the PEM, due to the small rate of transport and high rate of consumption at the position of the dense Pt layer, the concentration of reactants must approach to zero at the band position. In this case, the potential step is expected to occur in the vicinity of the band, as found in experiment[89]. The particle deposition process

in the membrane is due to repeated oxidation/dissolution and reduction/deposition of the migrated Pt ions by crossover O_2 and H_2, respectively[136]. At x_0 optimal conditions are provided for the deposition of particles to form the Pt band.

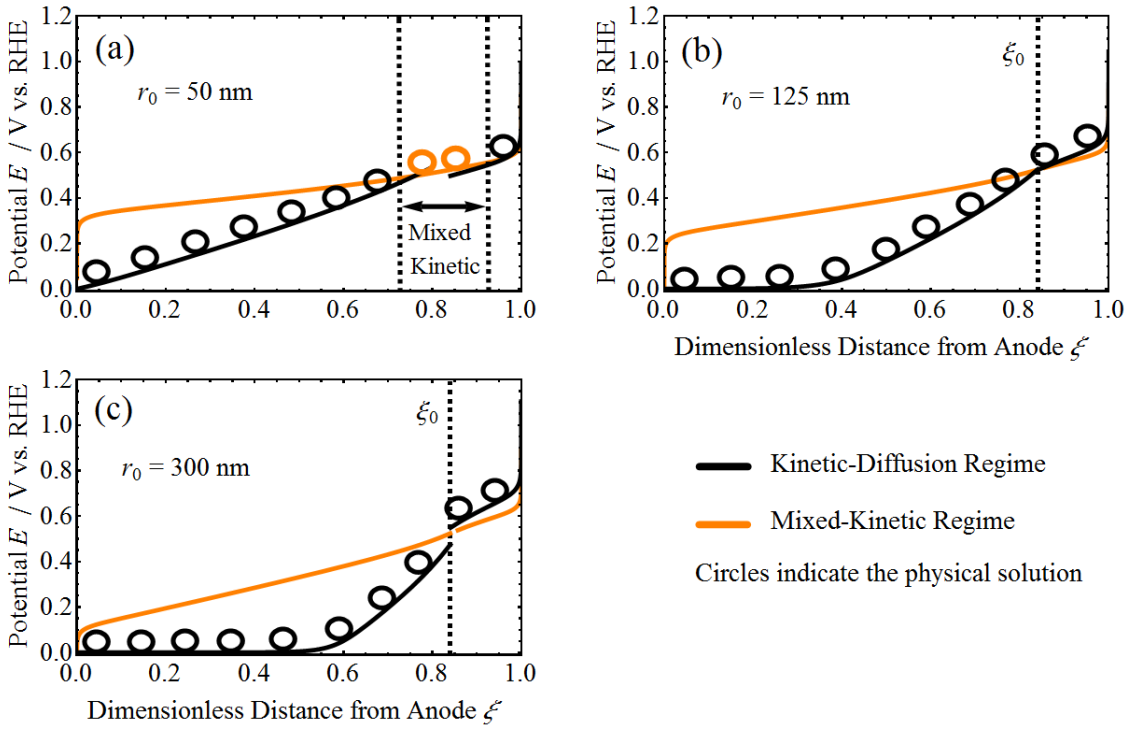

Figure 3.4: Potential distribution at spherical Pt nanodeposits in the PEM. The graphs shown in (a) to (c) illustrate change in the local reaction regime with increasing size of the Pt nanoelectrode.

Fig. 3.4 shows the potential distribution at spherical Pt particles in the PEM for a uniform distribution with $n_{Pt} = 10^{10}\ cm^{-3}$. In Fig. 3.4 (a)-(c), the potential profile in the mixed kinetic regime (see Fig. 3.2 (d) and Eq. 3.20) is compared to those of mixed "kinetic-diffusion" regimes in the two PEM regions (see Fig. 3.2 (a), Fig. 3.2 (b), Eq. 3.12 and Eq. 3.15). The results indicate that for particles with radius smaller than $r_0 \approx 125\ nm$, the transition of ORR from diffusion-limited to kinetically controlled regime occurs at $\xi < \xi_0$. Similarly, for this particle size range, the transition of HOR from diffusion-limited to kinetically controlled regime occurs at $\xi > \xi_0$. In the region between the two dashed lines in Fig. 3.4 (a), both HOR and ORR are controlled by the reaction kinetics. This case is more relevant to the Pt in the membrane, as the average PITM sizes reported in the literature are smaller than 125 nm[81]. It implies that in the vicinity of the potential step the concentration gradient of the reactants close to the particle surface is negligible as both reactions are kinetically controlled. On the other hand, for particles with radius greater than $r_0 \approx 125\ nm$

the transition occurs at ξ_0, as shown in Fig. 3.4 (b) and (c) (also see Fig. 3.2 (c) and Eq. 3.18).

In Fig. 3.5 (a), the potential profile is plotted as a function of the particle size at a particle density of $n_{Pt} = 5 \times 10^9\ cm^{-3}$, for a membrane with thickness of l= 50 μm. As shown, the OCP depends on the particle size, especially close to the step. As the particle size increases the potential decreases in the anodic region and increases in the cathodic region. The OCP change as a function of microelectrode size has been experimentally reported[150]. Particle size dependence of potential has also been obtained in the model by Atrazhev *et al.*[140].

Fig. 3.5 (b), shows the potential profile for a constant particle size (150 *nm*) as a function of n_{Pt}. As n_{Pt} increases, the potential decreases in the anodic region and increases in the cathodic region. For a constant particle size and uniform particle distribution, as the PEM thickness increases the potential decreases in the anodic region and increases in the cathodic region, as shown in Fig. 3.5 (c). At ξ_0, the value of the potential drop only depends on the particle size. At this position, the ratio of the concentrations of reactant gases is independent of the particle density (see Eq. 3.18); thus, according to Eqs. 3.12 and 3.15 the potential drop is independent of n_{Pt}.

Fig. 3.6 shows the current density distribution at Pt nanoparticles in the PEM as a function of particle density, corresponding to the potential distribution shown in Fig. 3.5 (b). At $\xi < \xi_0$, the current density increases from zero to a maximum value at ξ_0 (see Eq. 3.6); and at $\xi > \xi_0$ the current density decreases to zero (see Eq. 3.5). As n_{Pt} increases, the local flux becomes smaller due to the higher consumption of crossover gases.

Fig. 3.7 compares the model and experimental data of the potential profile for various relative partial pressures of H_2 and O_2. In the experimental measurements of Takaichi *et al.*[139], seven Pt microelectrode probes, with 30 μm in diameter, were used to measure the OCP determined by H_2 and O_2 permeating in the PEM. The microelectrodes are sandwiched between eight thin membrane films, 25 μm Nafion® (NRE211, Dupont, 3 $\times$ 7 cm), resulting in the total thickness of about 200 μm. H_2 at ambient pressure was fed to the anode side. At the cathode side, O_2 was held at partial pressures of 21 *kPa*, 25 *kPa*, 101 *kPa* and 119 *kPa*. In the experimental measurements performed by Liu and Zuckerbrod[74], flattened Pt wires with an initial diameter of 25 or 50 μm were used. Two Pt microelectrodes were laminated within a membrane electrode assembly with a dimension of 5 $\times$ 5 cm. Three layers of membranes were used. Two 10 μm GORE-SELECT® (GSM) membranes sandwiched a membrane with variable thickness, X. The two microelectrodes were laminated in between the outer 10 μm GORE-SELECT membrane and membrane X, both aligned with the gas inlet region, one close to the cathode and the other close to the anode. The position of the microelectrode area the cathode side was varied by changing the

thickness of the membrane X. Both anode and cathode were standard GORE-PRIMEA® Series 5510 electrodes with Pt loadings of 0.4 mg/cm^2. H_2 and air under 100 kPa pressure was fed to the anode and cathode sides, respectively. The potential at the microelectrodes was measured under OCP conditions at 60 °C.

To compare our model with the experimental data, we assume a spherical Pt microelectrode with r_0=5 μm in a membrane with $l = 200$ μm and a dilute particle density of $n_{Pt} = 10^7$ cm^{-3}. For the H_2 partial pressure we assumed 100 kPa and for the O_2 partial pressure we used the values reported in experiment. The variation in microelectrode shape does not demand a modification of the model; it is merely a parametric effect in the diffusion-limited current densities at the particle surface[144]. We use Eq. 3.49 to determine x_0 with $\beta = 0.38$ for all the pressure settings.

The potential shapes calculated from the model are in agreement with values of the potential found in experiment. As shown in Fig. 3.7, the step-like potential profile is reproduced in the model and the dependence of the position of the step to relative partial pressures at the membrane boundaries is captured. Discrepancies might be due to a combination of the effect of microelectrode size and shape. Microelectrodes used in the experiments are large compared to the thickness of the membrane; hence, the spatial localization of potential values is relatively imprecise and represents effective values. In contrast, the model predicts the exact local value of the potential at a spherical microelectrode in the PEM. It is required to perform experimental studies with smaller microelectrodes in order to obtain better spatial resolution.

In this chapter, we presented an analytical model based on a continuum description of crossover fluxes of reactant gases to calculate the local mixed electrode potential in the membrane, which is closely related to the local equilibrium conditions at Pt nanoparticles for affecting the net radical balance. The results obtained are in good agreement with experimental measurements. The related parameters were also provided for future reference. The model will be employed for understanding of the balance of the degrading species which directly affect the lifetime of polymer electrolyte membrane in the fuel cell applications.

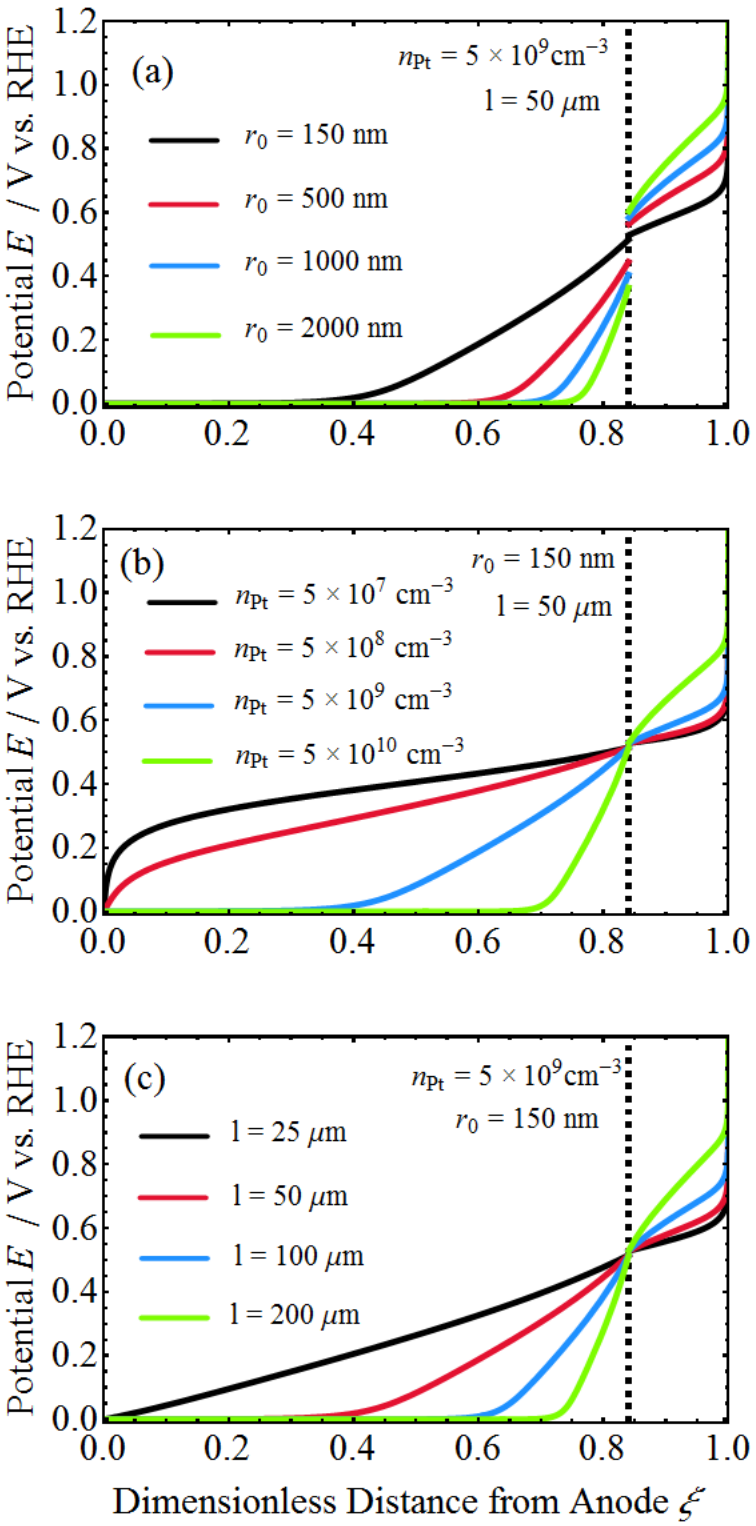

Figure 3.5: Analytical solution of the potential distribution at spherical Pt nanodeposits in membrane, for (a) varying particle sizes, (b) varying particle densities, and (c) varying membrane thickness.

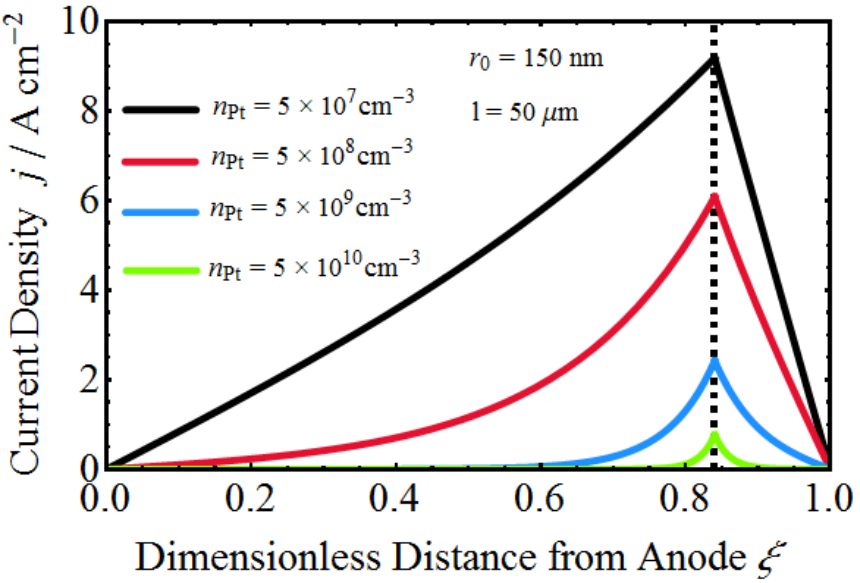

Figure 3.6: Current density distributions at spherical Pt nanoelectrode calculated in the model, for various values of the particle density, corresponding to the cases depicted in Fig. 3.5 b.

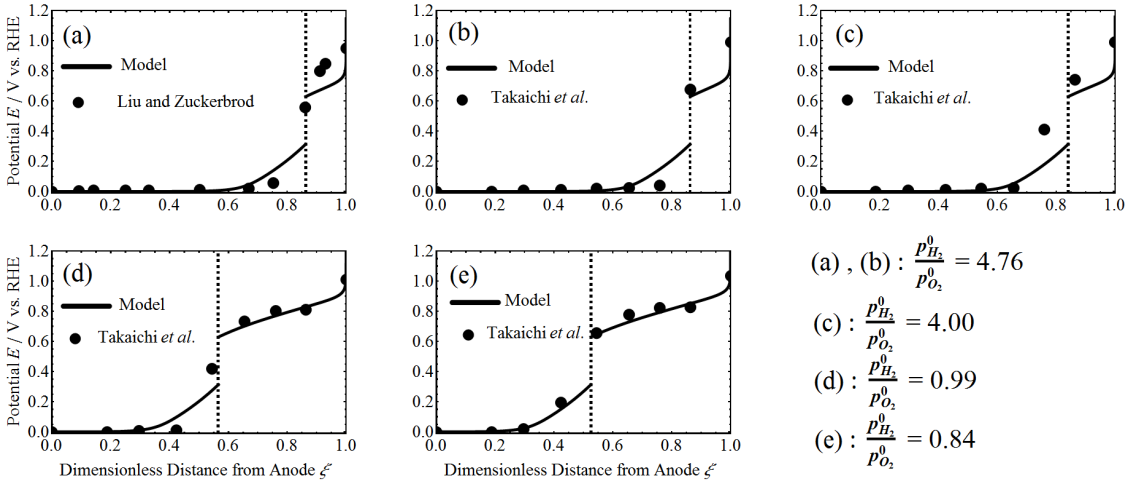

Figure 3.7: Comparison between potential distributions and those observed in experiment for various relative partial pressures of H_2 and O_2 at the membrane boundaries, as indicated in the graphs. Parameters used in calculations are listed in Table 3.1 and 3.2

Chapter 4

DFT Study of Oxygen Reduction Reaction Mechanism at Pt(111)

As for the second step of the approach to understand the role of PITM on membrane degradation, density functional theory was used to investigate the influence of the Pt adsorption state on the formation of H_2O_2 and $^{\bullet}OH$ as two important reactive oxygen species. We generated the free energy diagrams of reduction sequences involving O_2 and H_2O_2 as reactants and H_2O_2, $^{\bullet}OH$, or H_2O as products. The Pt (111) water interface was considered in three adsorption states that are encountered in different regions of the electrode potential: an adsorption state with a monolayer of hydrogen (low electrode potential); a clean surface (intermediate potential); and an adsorption state with 1/3 of a monolayer of oxygen (high potential). Results reveal a strong impact of surface water interactions on the pathways of water oxidation and oxygen reduction reactions. In agreement with experimental results reported in the literature, we found that the oxygen reduction pathway is highly sensitive to the hydrogen coverage. Coverage by one monolayer hydrogen renders the surface highly hydrophobic, thereby suppressing its activity for the oxygen reduction. Therefore, for high hydrogen coverage, the formation of H_2O_2 by a two-electron pathway becomes a preferred path. Next, we present our collaborative experimental study to validate the theoretical results in the context of radical-initiated chemical degradation of polymer electrolyte membranes in polymer electrolyte fuel cells.

4.1 Introduction

Cyclic voltammetry (CV) studies reveal the Pt surface adsorption state as a function of electrode potential;[96,151–153] CVs of Pt (be it for nanoparticle-based supported catalysts or

extended surfaces) distinguish three characteristic potential regions: (i) the region of hydrogen under-potential deposition (HUPD region) at electrode potentials between $0.05V < E < 0.40V$ vs. RHE; (ii) the double layer region at $0.40V < E < 0.60V$ vs. RHE and (iii) the surface oxide region at $E > 0.7$ V vs. RHE.

Markovic *et al.*[154,155] studied the oxygen reduction reaction (ORR) on a rotating-disk electrode using Pt low index single crystal surfaces. They found that the ORR is highly structure-sensitive in the HUPD region. The activity of the ORR on Pt (111) decreases in this region, reaching half of the value of the diffusion-limited current for the four-electron process; the diffusion-limited current in this potential region corresponds to the two-electron reduction of O_2 with near 100% H_2O_2 formation.[156] Similarly, the H_2O_2 reduction activity was seen to decrease with hydrogen adsorption[154]. The authors discussed that these results imply a change in the mechanism of the ORR in the hydrogen adsorption region. However, in spite of the importance of this process, to the best of our knowledge, it has not yet been theoretically addressed[157–159].

In the approach to understand the balance of H_2O_2 and $^{\bullet}OH$ at Pt nano-deposits in the PEM, in the previous chapter, we presented the reaction-diffusion model to calculate the local potential at isolated Pt particles in the PEM. The potential depends on the local composition of the electrolyte. Under H_2-rich conditions, the potential is close to the equilibrium potential of the HOR; while under O_2-rich conditions, it is closer to the equilibrium potential of the ORR. The transition between the two cases occurs at a point in the membrane where both HOR and ORR are controlled by diffusion.

Subsequently, we relate the particle potential to specific adsorption states of Pt, using experimental data[156,160,161] and DFT simulations[162–166]. As a logical continuation, this chapter focuses on DFT studies of the reaction paths in different surface adsorption states that correspond to distinct potential regions, discussed in the previous paragraph. We have evaluated processes that lead to formation or deactivation of H_2O_2 and $^{\bullet}OH$ at the Pt-water interface. Our study is different from extensive investigations of ORR at Pt (111),[157,158,167–169] since we take explicitly into account both adsorbates and a water layer at the surface. By comparison to experimental results, we evaluate the significance of our findings for reactions at Pt nano-deposits in PEMs, as well as in the broader context of Pt-catalyzed surface reactions.

4.2 Model System

The surface was modeled by a super-cell containing a four-layer slab of Pt (111) and a $2\sqrt{3} \times 2\sqrt{3}\ R30^o$ water layer with hexagonal structure on one side of the slab to model the metal-solution interface. The hexagonal water structure at close-packed metal surfaces has been studied experimentally[170,171] and theoretically[131,172]. Our model included 12 Pt atoms per slab layer and 8 water molecules per unit cell. Repeated slabs were separated by a vacuum region of about 15 Å. Our computational method and model system is similar to Refs.[131,132], for which the convergence tests for DFT calculations had been done.

The simulated slab is asymmetric, with adsorbates and water layer considered only at one surface. This configuration leads to the accumulation of equal and opposite charges at opposing surfaces of the slab. A standard dipole correction scheme,[173] implemented in VASP, has been used to compensate the unphysical interaction between opposite surfaces that correspond to neighboring images across the vacuum region of the periodically repeated slab. In this approach, a dipole moment is inserted in the center plane of the vacuum region that results in a constant potential value.

In all geometry optimizations, the two bottom layers of the slab were fixed in their bulk positions, while the two top layers together with adsorbates and the water layer were allowed to relax. It should be noted that at low temperature the arrangement of a monolayer of water at Pt (111) has $\sqrt{37} \times \sqrt{37}\ R25.3^o$ and $\sqrt{39} \times \sqrt{39} R16.1^o$ periodicities,[174] as found in high resolution scanning tunneling spectroscopy (STM) images[175] and DFT calculations[176]; however, we did not use these larger structures assuming that it does not impact our investigation of the ORR mechanism.

We set out to study the influence of the surface adsorption state on the energetics of Pt surface reactions; therefore, we considered three adsorption states for Pt (111) that correspond to different potential regions: (1) For the HUPD region, we considered adsorption of one monolayer (ML) of hydrogen at the fcc sites, which has been found theoretically to be more stable compared to adsorption at atop and hcp sites[132,162,164]. (2) In the double layer potential region, we considered an adsorbate-free Pt surface in direct contact with a water overlayer as the most stable surface state[162,165]. (3) For the oxide region, we considered 1/3 of a monolayer of oxygen adsorbed at fcc sites[162,165,166].

To account for the orientation of water molecules at the interface, we evaluated two water structures: 1. The H-up structure, originally proposed by Doering and Madey[177], in which half of the water molecules bind directly to surface Pt atoms with one lone pair orbital of the oxygen (the so-called flat-lying water molecules), while the other half, i.e., every second water molecule in the adsorbed layer, has OH bonds that point away from the

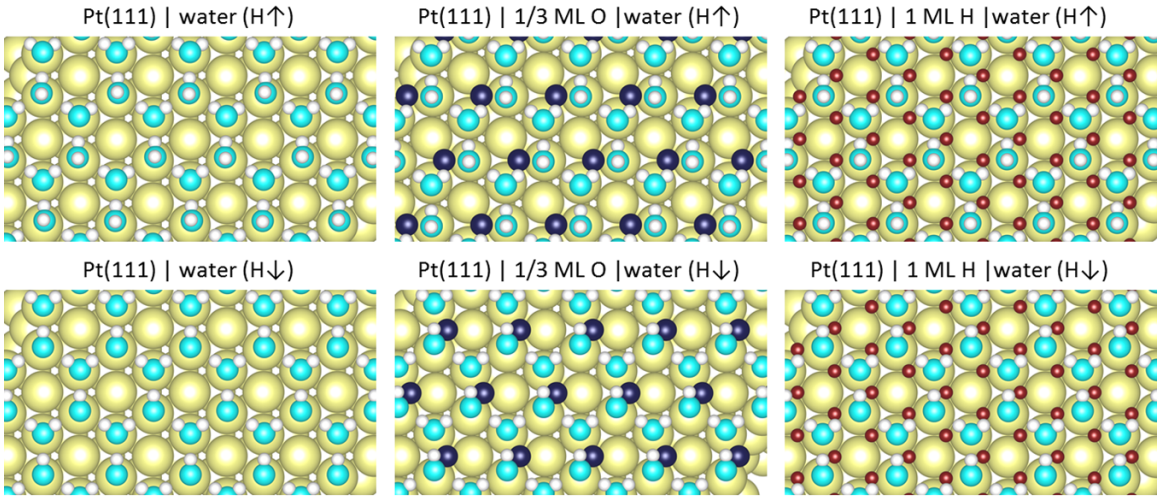

Figure 4.1: Top view of the final states of the model systems; yellow, light blue, white, brown, and dark blue colors are used to represent Pt, O, H, H*, and O*, respectively.

surface. 2. The H-down structure, with OH bonds of every other water molecule oriented towards the surface[178]. The corresponding structures are shown in Fig. 4.1. The orientation of surface water molecules depends on electrode potential, adsorption state, and the total surface charge density; the positively (or negatively) charged surface stabilizes the H-up structures (or H-down)[179]. Fully self-consistent computations of these dependences are still not computationally feasible. In this chapter, we compare reaction pathways and energetics obtained for the two interfacial water structures with fixed orientation. Consistent with the study by Schnur and Groß,[131] we found that in all cases the H-down structures are slightly more stable than H-up structures (by less than 0.05 eV). We note that in thermodynamic equilibrium the two orientations will be mixed due to the thermal reorientation of water molecules[131,179].

4.3 Results and Discussion

4.3.1 Oxygen Reduction Pathways at Pt (111)

The ORR is an important and notoriously complex reaction in electrochemistry. First-principles quantum mechanics calculations based on DFT have been established as a first and crucial step in a hierarchy of methods to understand the ORR mechanisms at Pt(111)[167]. In spite of extensive efforts in this field, pivotal effects such as the sensitivity of the ORR to

the surface adsorption state or implications of surface-water interactions on reaction pathways have not been understood in sufficient detail[167,180,181].

In a complete electrochemical ORR sequence, molecular oxygen needs to be associated with four electrons and protons ($O_2 + 4H^+ + 4e^- \rightarrow 2H_2O$)[182]. In the process, electrons lose potential energy by occupying lower energy levels in the water molecules formed. The total Gibbs energy change for all four electrons is -4.92 eV, which corresponds to 1.23 eV per electron. The ORR proceeds at the catalyst surface, where electrons are readily available, at a concentration that is determined by the electronic density of states of the metal. Protons are supplied from the electrolyte, with a concentration determined by the composition of the electrolyte and by the distribution of the electrolyte potential[13].

The ORR sequence involves surface-adsorbed intermediate species (indicated by a *) such as surface oxygen, O^*, hydroxide, OH^*, superoxide, OOH^*, hydrogen peroxide, $H_2O_2^*$ and water, H_2O^*. To generate the free energy diagrams (FED) for the ORR, explicit determination of the binding energies of the intermediates is required.

In this DFT study, we employed a coupled-proton-electron-transfer (CPET) process, originally proposed by Damjanovic and Brusic,[182] for each of the electrochemical reaction steps. This allowed us to use the original approach developed by Nørskov and coworkers[183] to account for the electrode potential in free energy calculations. In this approach the potential is only included indirectly for reaction steps that involve CPET processes.

The reaction Gibbs energies of the reaction step is obtained using thermochemical considerations[158,162,165,183–186], based on the equation

$$\Delta G = \Delta E + \Delta ZPE - T\Delta S + \Delta G_{\mathrm{pH}} + \Delta G_U . \tag{4.1}$$

where, ΔE is the binding energy, ΔZPE is the zero-point energy and $T\Delta S$ is the entropy change; ΔG_{pH} and ΔG_U are the free energy contributions due to variations in proton concentration and electrode potential, U, relative to a reference state. Zero-point energy corrections and entropic contributions to the free energy of adsorption are typically small and often neglected in theoretical studies; for example, the contribution corresponding to ΔZPE-$T\Delta S$ for $(O^* + H_2)$ is 0.05 eV, and that for $(OH^* + 1/2H_2)$ is 0.35 eV, while the corresponding calculated reaction heats for Pt(111) system is 1.57 eV and 1.05 eV, respectively[183].

Energy optimization studies based on DFT calculations are carried out to find the total energy change, ΔE, involved in a CPET process, which might correspond to formation, transformation or release of an adsorbed reaction intermediate at the electrode/electrolyte interface[157,168,187],

$$\Delta E = E_{total} + \frac{n}{2} E_{\mathrm{H_2}} - E_{Ref}, \tag{4.2}$$

where, E_{total} is the total energy of an intermediate adsorbed to the substrate, and n denotes the number of CPET in each step required to reach the final step, i.e., with two water molecules as product. For example, n for the step involved OOH^* is 3, while that for the step involved O^* or OH^*, is 2 and 1, respectively. The reference energy, E_{Ref}, corresponds to the surface configuration optimized with a complete water bilayer and a water molecule in gas phase (see Fig. 4.1).

In the CHE method[183], the reference state corresponds to the standard hydrogen electrode. At standard conditions ($T = 298$ K and $P = 1$ atm, [pH] $= 0$), with $U_{\mathrm{SHE}} = 0$ V, the hydrogen oxidation/evolution reaction ($\frac{1}{2}H_2(g) \rightleftharpoons H^+(aq) + e^-$) is in equilibrium. Thus, by referring the potential to that of the standard hydrogen electrode, the free energy of hydrogen in the gas phase ($\frac{1}{2}H_2(g)$) can be used instead of that for electron and proton in solution ($H^+(aq) + e^-$). Therefore, in this simple and efficient approach, the electrochemical potential can be accounted for without having to perform computationally intensive and relatively inaccurate calculations of the solvation energy of protons. More generally, the CHE circumvents taking the molecular electrochemical environment of metal electrode and reactive species in the electrolyte into account. Deviation of the electrode potential from equilibrium shifts the reaction Gibbs energy by $\Delta G_U = -e_0(U - U_{\mathrm{SHE}}) = -e_0 U$ for each step that includes a coupled proton and electron transfer step. Variation in the pH is represented by a term $\Delta G_{\mathrm{pH}} = k_{\mathrm{B}} T ln[H^+]$ in Eq.(4.1).

This method has been applied to predict trends in the electrochemical activity of the ORR[158,162,165,183–186]. The concept has been expanded to account not only for the mechanisms with coupled proton and electron transfer, but also for other redox couples[188]. The method has also been employed to create surface Pourbaix diagrams for surface coverages of intermediates of ORR and water oxidation at various transition metals,[162] and more recently, for equilibrium coverages of various halides on metal electrodes[189].

We considered three possible mechanisms for the reduction of $\mathrm{O_2}$ to form $\mathrm{H_2O}$ or $\mathrm{H_2O_2}$ (M1 to M3), and three mechanisms for the formation of the hydroxyl radical, $^{\bullet}$OH (M4 to M6):

M1. In this mechanism, adsorption of $\mathrm{O_2}$ is followed immediately by one CPET to form OOH^*. Then two water molecules at the surface are involved as catalysts to dissociate OOH^*, leading to the formation of $3OH^*$ and the immediate reproduction of one water molecule. OH^* intermediates undergo three further CPET to reproduce the second water molecule and form two new water molecules as the reaction products.

Table 4.1: Reaction Energies of the Elementary Reaction Steps (in eV) at U = 0 V

Mechanism	Pt-water-Hup	Pt-water-Hdown	Pt-1/3 ML O-water-Hup	Pt-1/3 ML O-water-Hdown	Pt-1 ML H-water-Hup	Pt-1 ML H-water-Hdown
(1.1) $O_2 + H^+ + e^- \rightarrow OOH^*$	-0.83	-0.80	-0.36	-0.36	-0.09	-0.06
(1.2) $OOH^* + H_2O \rightarrow 3OH^*$	-1.63	-1.69	+0.43	+0.12	+1.09	+1.26
(1.3) $3OH^* + H^+ + e^- \rightarrow 2OH^* + H_2O$	-0.58	-0.51	-1.19	-0.90	-1.57	-1.32
(1.4) $2OH^* + H^+ + e^- \rightarrow OH^* + H_2O^*$	-1.00	-1.28	-2.06	-1.94	-2.40	-2.62
(1.5) $OH^* + H^+ + e^- \rightarrow H_2O$	-0.87	-0.64	-1.74	-1.84	-1.95	-2.12
(2.1) $OH^* + H^+ + e^- \rightarrow H_2O$	-0.87	-0.64	-1.74	-1.84	-1.95	-2.12
(2.2) $OOH^* + H^+ + e^- \rightarrow O^* + H_2O$	-2.72	-2.78	-2.57	-2.64	—	—
(2.3) $O^* + H^+ + e^- \rightarrow OH^*$	-0.53	-0.75	-0.81	-0.65	—	—
(2.4) $OH^* + H^+ + e^- \rightarrow H_2O$	-0.84	-0.59	-1.18	-1.27	—	—
(3.1) $OOH^* + H^+ + e^- \rightarrow H_2O_2^*$	-0.60	-0.79	-1.07	-1.09	-1.35	-1.32
(3.2) $H_2O_2^* \rightarrow H_2O_2$	+0.09	+0.26	+0.08	+0.11	+0.11	+0.04
(3.3) $H_2O_2^* \rightarrow 2OH^*$	-2.07	-2.07	-0.48	-0.65	+0.09	+0.01
(4) $OOH^* + H_2O \rightarrow 2OH^* + \bullet$OH	+1.08	+1.09	+2.52	+2.51	+2.83	+2.72
(5) $H_2O_2^* \rightarrow OH^* + \bullet$OH	+0.68	+0.61	+1.53	+1.67	+1.78	+1.88
(6) $2OH^* \rightarrow OH^* + \bullet$OH	+2.75	+2.68	+2.02	+2.32	+1.68	+1.90

M2. In this mechanism, originally proposed by Anderson *et al.*,[190,191] OOH^* formed in the initial step is followed by a CPET to form O^* and H_2O^*. Then O^* undergoes two subsequent CPET to form the second H_2O.

M3. In this mechanism, O_2 adsorption is followed by two CPET to form $H_2O_2^*$. The two electron reduction pathway is completed, when $H_2O_2^*$ desorbs from the surface. However, $H_2O_2^*$ might decompose before desorbing, forming $2OH^*$, which can undergo two CPET to form two water molecules.

M4. In this mechanism, OOH^* formed as in M1, decomposes with water at the surface to form $2OH^*$ and $^\bullet$OH.

M5. $^\bullet$OH could be formed by decomposition of $H_2O_2^*$ to OH^* and $^\bullet$OH.

M6. $^\bullet$OH could be formed by direct desorption of OH^*.

The elementary reaction steps of the mechanisms and the corresponding reaction Gibbs energies at $U = 0\ V$ vs. RHE for the H-up and H-down water layer structures are shown in Table 4.1. Results indicate that the water orientation exerts a smaller impact on the reaction energies than the surface adsorption state. The impact of the water orientation on the reaction energies is due to the different surface potential contributions for H-up and H-down water layers[131].

We generated the FED of these mechanisms at the Pt (111)-water interface for the three Pt surface adsorption states defined above. Using binding energies of reaction intermediates obtained from DFT, we calculated the FED for the HUPD region (corresponding to U=0 V vs. RHE), for the double layer region (at U=0.5 V vs. RHE) and for the surface oxide region (U=0.9 V vs. RHE). The open circuit potential for the $4e^-$ ORR was considered as 1.23 V vs. RHE and that for $2e^-$ ORR was considered as 0.68 V vs. RHE[192].

Fig. 4.2 (a1 and a2) show the FEDs for the ORR along the reaction paths M.1 (green path), M.2 (black path), M.3 (blue path for the $2e^-$ reduction) and M.4 (red path) at clean Pt (111), corresponding to $U = 0.5\ V$ vs. RHE, with H-up or H-down water layer structures (upper and lower panels, respectively). Fig. 4.2 (b1 and b2) depict FEDs for reaction paths M.3 (black) as well as for M.5 and M.6 (in red). The FEDs show that the four electron pathway of the ORR, resulting in the formation of two water molecules, is clearly preferred for the clean surface state in the intermediate potential region. The formation of H_2O_2 is possible but thermodynamically highly unlikely. Instead, a clean Pt surface could be expected to be highly effective at reducing H_2O_2 to water. The spontaneous formation of $^\bullet$OH is completely insignificant.

Fig. 4.3 (a1 and a2) show the FEDs of the ORR in the surface oxide region, at $U = 0.9\ V$ vs. RHE. The increased electrode potential increases the reaction Gibbs energy for the formation of OOH^*. In addition, the positive ΔG for the decomposition of OOH^* by surface water molecules suggests that M1 is inhibited for this surface state. Similarly, the positive ΔG for H_2O_2 and $^\bullet$OH, prevents the formation of these species in the oxide region at $U = 0.9\ V$ vs. RHE. Instead, H_2O_2 or $^\bullet$OH, if present as a reactant in solution, would be scavenged at the Pt surface and reduced to water in this potential regime, as shown in Fig. 4.3 (b1 and b2). It has also been suggested that the dissociative adsorption of oxygen ($1/2O_2 \rightarrow O^*$) offers a more favorable pathway for the ORR at high electrode potentials[158]; whereas, the formation of OOH^* intermediates becomes more favorable as the potential decreases from $0.6\ V$ to $0.3\ V$ vs. RHE[159].

Fig. 4.4 (a1 and a2) show the FEDs of the ORR in the HUPD region, at $U = 0.0\ V$ vs. RHE. For this surface state, M1 is suppressed, as the intermediate state with formation of $3OH^*$ involves a high activation Gibbs energy. M2 is also inhibited for this surface state as the adsorbed hydrogen atoms block the reactive fcc sites necessary for the formation of O^*. However, M3 proceeds spontaneously in this region, since the $2e^-$ process is exothermic at $U = 0\ V$ vs. RHE. As shown in Fig. 4.4 b, the presence of a monolayer of adsorbed hydrogen prevents the HO-OH bond cleavage and stabilizes $H_2O_2{}^*$. Therefore, for this surface state, $H_2O_2{}^*$ formed as an intermediate could be released into the electrolyte and thereby be prevented from further reduction to water by a relatively large energy barrier that could

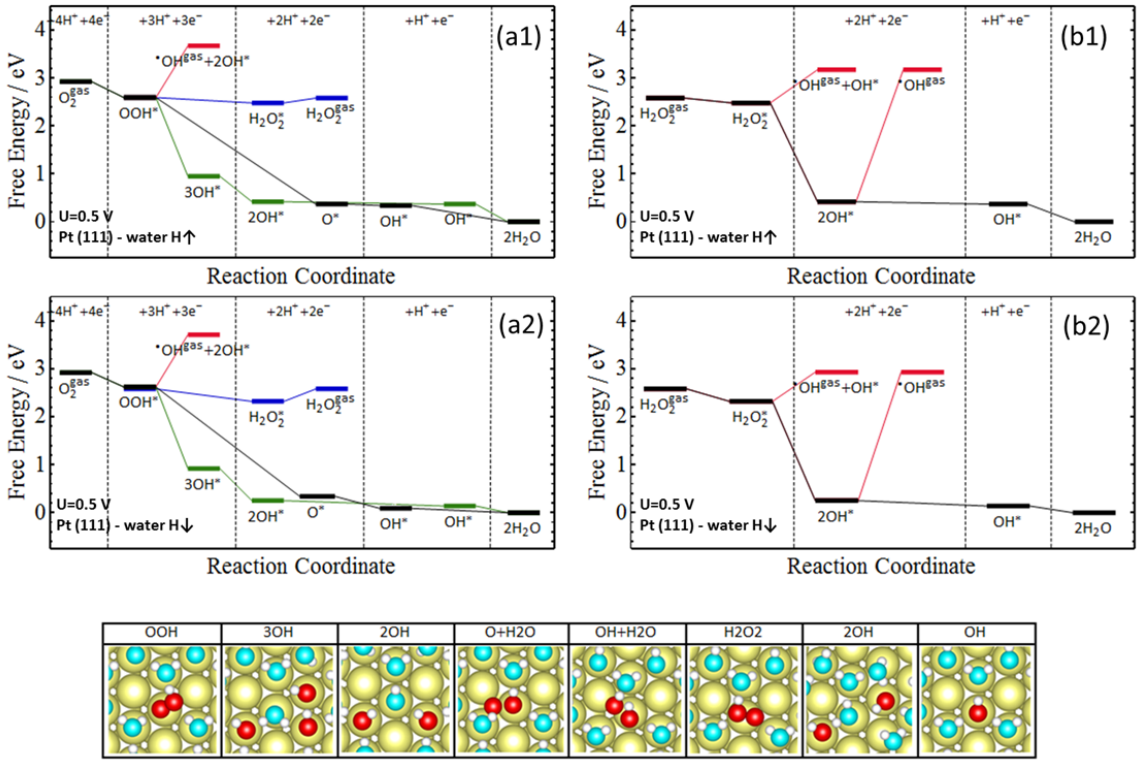

Figure 4.2: Free energy diagrams of oxygen reduction reaction (on left) and hydrogen peroxide reduction reaction (on right) at clean Pt (111)-water interface for U = 0.5 V vs RHE. Results for H-up and H-down water configurations are shown in top (a1 and b1) and bottom (a2 and b2) panels, respectively. Optimized structures of the most important intermediate states are shown below the energy diagrams. Yellow, light blue and white colors are used to represent Pt, O, and H, respectively; oxygen atoms of the intermediates are shown in red for clarity.

be involved in the formation of $2OH^*$. In the following section, we will discuss more about this effect in terms of hydrophobicity of the hydrogen-covered Pt (111) surface. Experimental observations of a preferential two-electron exchange in the HUPD region at Pt(111), as well as the detection of H_2O_2 in this potential range confirm our findings [154,193–195].

It should be noted that mechanism M1 has been studied by Rossmeisl *et al.* [186] for a half dissociated hexagonal water structure at Pt (111), where every second water molecule has been oxidized to OH*. They found that O_2 reduction proceeds via a direct $4e^-$ pathway, with negligible peroxide formation [186]. The reaction barrier for proton transfer, calculated in Ref. [186] was 0.26 eV.

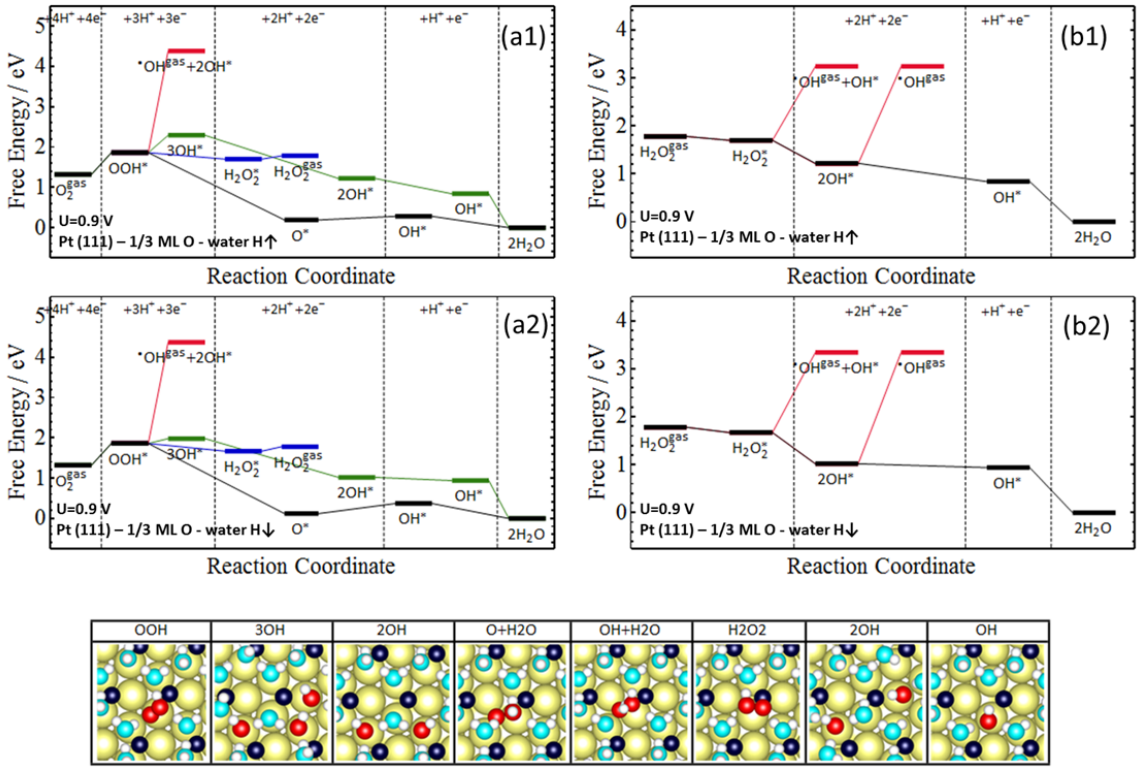

Figure 4.3: Free energy diagrams of oxygen reduction reaction (on left) and hydrogen peroxide reduction reaction (on right) at 1/3 ML oxygen covered Pt (111)-water interface for U = 0.9 V vs RHE. Results for H-up and H-down water configurations are shown in top (a1 and b1) and bottom (a2 and b2) panels, respectively. Optimized structures of the most important intermediate states are shown below the energy diagrams. Yellow, light blue, and white colors are used to represent Pt, O, and H, respectively; dark blue are adsorbed oxygen atoms and red are oxygen atoms for the intermediates shown in different color for clarity.

4.3.2 The origin of hydrogen peroxide formation at hydrogen-covered Pt (111)

Analysis of electrochemical quartz-crystal nanobalance (EQCN) have revealed that the interfacial mass of a Pt electrode reaches a minimum value with the completion of the saturation layer of electroadsorbed HUPD[196]. Jerkiewicz *et al.* discussed that the layer of HUPD modifies the surface dipole moment and the wetting properties of Pt, which in turn minimizes the interaction of water molecules with the surface. This renders the hydrogen-covered Pt surface hydrophobic, as has also been addressed in a recent DFT study[132].

To evaluate the impact of hydrogen adsorption on the surface hydrophobicity, we calculated the average adsorption energy per water molecule at clean and hydrogen-covered surfaces, defined as

$$E^{ads} = (E_{total} - (E_{slab(-H)} + nE_{H_2O}))/n, \tag{4.3}$$

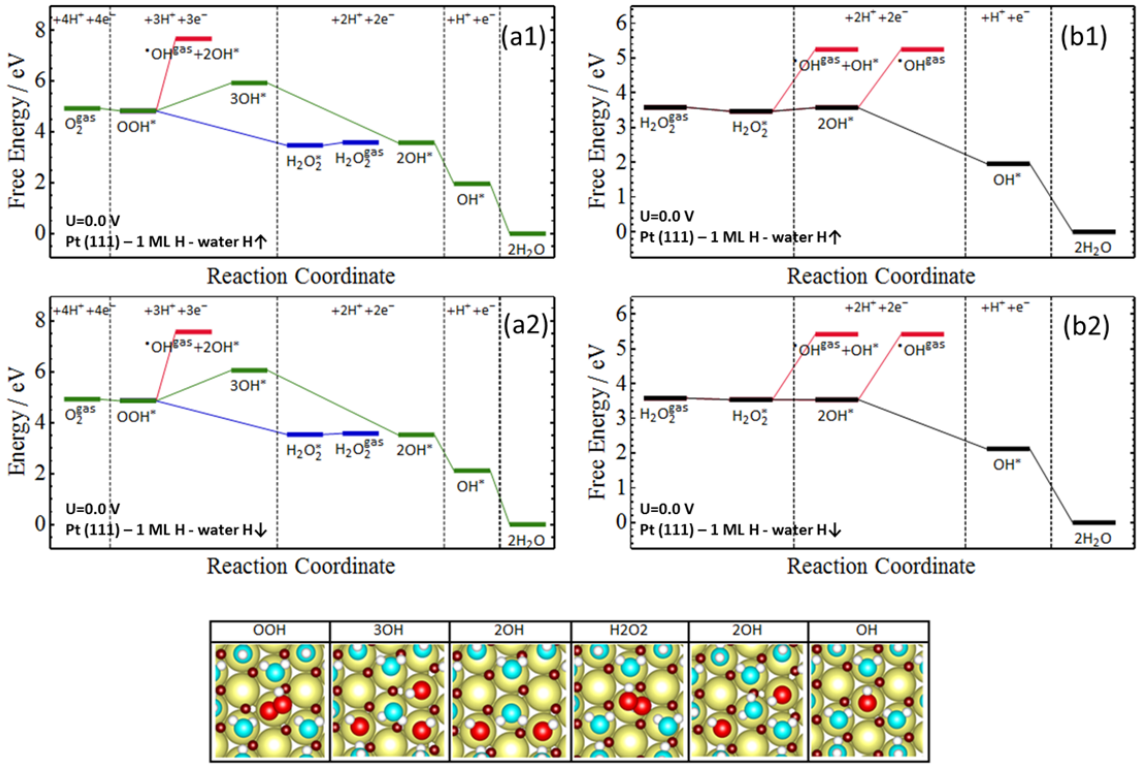

Figure 4.4: Free energy diagram of oxygen reduction reaction (on left) and hydrogen peroxide reduction reaction (on right) at 1 ML hydrogen-covered Pt (111)-water interface for U = 0 V vs RHE. Results for H-up and H-down water configurations are shown in top (a1 and b1) and bottom (a2 and b2) panels, respectively. Optimized structures of the most important intermediate states are shown below the energy diagram. Yellow, light blue, and white colors are used to represent Pt, O, and H, respectively; brown are adsorbed hydrogen atoms and red are oxygen of the intermediates shown in different color for clarity.

Here, E_{total} is the total energy of the reference system; $E_{slab(-H)}$ is the energy for the slab; E_{H_2O} is the energy of a water molecule in vacuum; and n is the number of water molecules in the unit cell. For a water layer at the surface, we found similar values of $E^{ads} = -0.48$ eV and -0.46 eV at the clean and hydrogen-covered surfaces, respectively; which is consistent with Ref.[132].

On the other hand, the adsorption energy for a single flat-lying water molecule (defined as $E^{ads}[monomer]$, where $n = 1$ in the above equation) was found to be drastically different for clean and hydrogen-covered surfaces. For the clean surface it was found to be -0.24 eV and for the hydrogen-covered surface it was found to be -0.04 eV. We calculated the H-bond energy in the adsorbed water structure, defined as in Ref.[197].

$$E^{\mathrm{HB}} = \left(E^{\mathrm{ads}}[\mathrm{monomer}]N_{\mathrm{Pt}-H_2O} - nE^{\mathrm{ads}}\right)/N_{\mathrm{HB}} \tag{4.4}$$

Here, $N_{(Pt-H_2O)}$ is the number of molecule surface bonds and N_{HB} is the number of H-bonds in the water structure. In this case, we obtained the values of -0.15 eV and -0.29 eV for the clean and hydrogen-covered surfaces, respectively. At the hydrogen-covered Pt surface, HB among water molecules are stronger as compared to the clean surface.

In Fig. 4.5, the isodensity contours of the total electron density as well as the charge density difference isosurfaces of a water monomer at clean and hydrogen-covered surfaces are compared. As shown, the electron density is very small in the region between the water molecule and the hydrogen-covered surface. Moreover, the distance between the water molecule and Pt surface is significantly larger in this case (3.55 Å at the hydrogen-covered surface as compared to 2.46 Å at the clean surface). Similarly, in the case of one water layer at the surface, the average distance of water molecules from the hydrogen-covered surface was found to be 4.09 Å (and 3.90 Å) in H-up (and H-down) structures; while, that for the clean surface was obtained as 3.36 Å (and 3.64 Å), respectively.

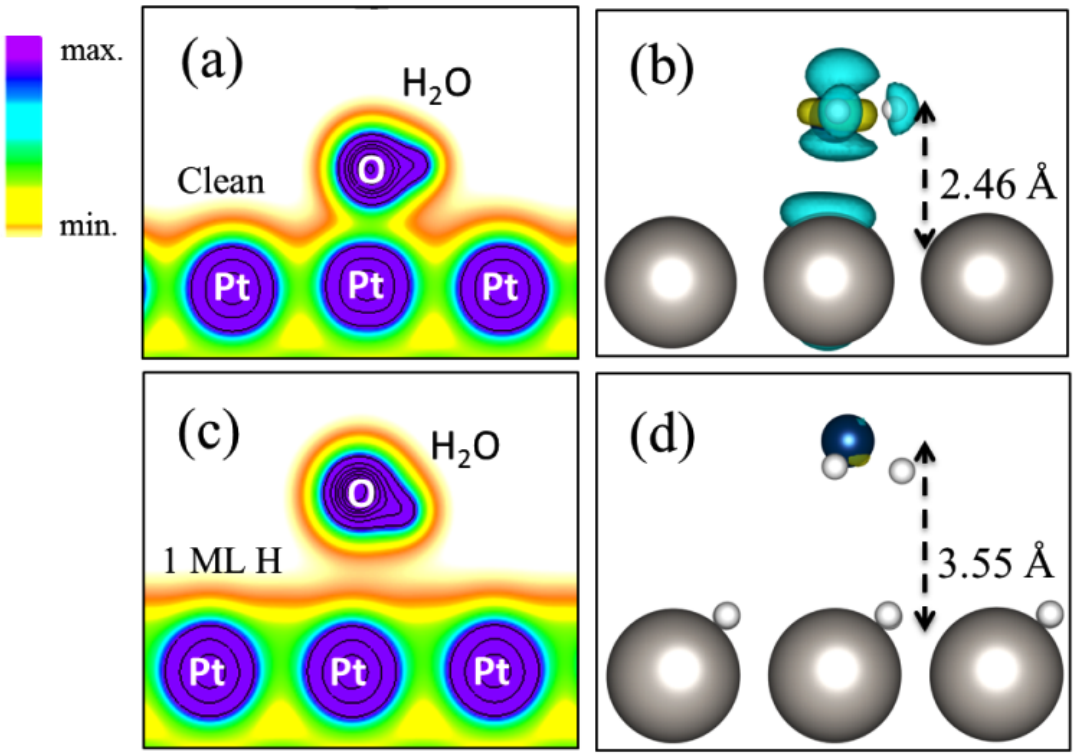

Figure 4.5: Isodensity contours for the total electron density (left panel) and the three dimensional charge density differences (right panel) for a water monomer at clean ((a) and (b)), and hydrogen-covered Pt (111) ((c) and (d)), respectively. In (b) and (d), the isosurface value is taken as 0.002 e per $Å^3$.

Fig. 4.6 shows the difference between the total plane averaged charge density of the interfacial system and separately calculated charge densities of the Pt slab and the adsorbates

Table 4.2: Bader analysis of surface charge (in units of an e) for the electro-adsorbed hydrogen atoms and the top two Pt layers of the (111) surfaces. The charge is reported relative to the corresponding uncharged atom. The average distance of water molecules in the water layer from the surface is included for varying hydrogen coverages.

	Pt-water	Pt-1/4 ML H-water	Pt-1/2 ML H-water	Pt-3/4 ML H-water	Pt-1 ML H-water
average charge on adsorbed hydrogen atoms on surface (e)	—	-0.046	-0.056	-0.036	-0.028
average charge in first top Pt layer (e)	-0.043	-0.019	+0.011	+0.021	+0.034
average charge on second top Pt layer (e)	+0.044	+0.034	+0.022	+0.010	+0.001
average distance of water layer from surface (Å)	3.36	3.55	3.82	4.08	4.09

(defined as $\Delta\lambda$) as a function of the z-coordinate (normal to the surface). Results reveal that the adsorption of hydrogen induces charge polarization at the interface with the dipole moment directed towards the surface, which is consistent with the experimental study [196].

To obtain a more quantitative picture of surface charging effects, we performed Bader analyses [198] for various hydrogen coverages. In this method the electron density around an atom (or ion) in periodic system is analysed to calculate the associated charge of the valence electrons. The results are summarized in Table 4.2. The values represent the partial charge excess/deficiency at adsorbed hydrogen atoms as well as the average charge per Pt atom for the first and for the second layer of the slab. The average charge per Pt atom in the first layer, changes sign from a negative value in the clean surface state to increasingly more positive values with increasing hydrogen coverage.

Impact of surface hydrophobicity on the formation of OH*: As discussed in the previous section, adsorbed hydrogen on fcc sites of Pt (111) inhibits the breaking of the O-O bond necessary for the $4e^-$ pathway M2, in which O^* is an intermediate. Even though H_2O_2 is a higher energy product than H_2O, a two electron pathway to produce H_2O_2 is preferred. Uphill reaction steps involved in the dissociation of OOH* to 3OH* (in M1) and the H_2O_2* decomposition to 2OH* (in M3) render H_2O_2 a relatively stable intermediate reaction product; its diffusion-induced dilution in the electrolyte will suppress the further reaction to H_2O.

As OH* is the key intermediate to understand the path selectivity of the oxygen reduction and hydrogen peroxide decomposition at hydrogen-covered Pt (111), it is useful to generate the surface charge density difference of a system, which contains chemisorbed

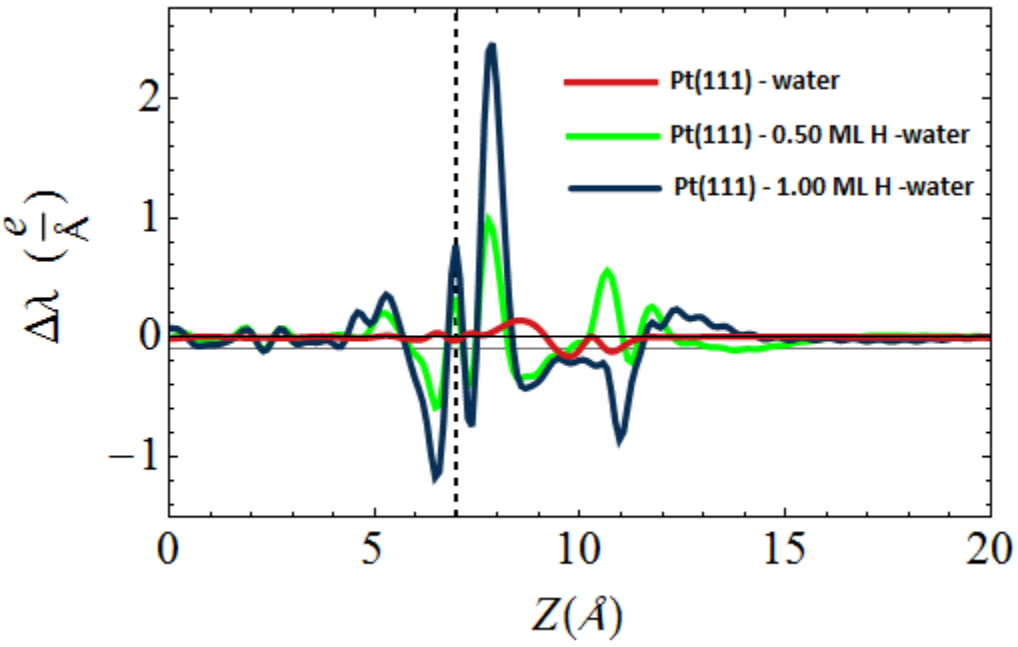

Figure 4.6: Planar average of the induced charge density along the surface normal for clean and hydrogen-covered surfaces.

OH. This gives information about charge transfer and bond formation. It clarifies moreover the strength of the interaction between Pt surface and species in the water layer. The charge density difference function for this system is defined as,

$$\Delta\rho = \rho_{total} - \rho_{slab(-H)} - \rho_{water(-OH)}, \tag{4.5}$$

Here, ρ_{total} is the total charge density of the system; $\rho_{slab(-H)}$ is the charge density for the clean (and the hydrogen-covered) slab; and, $\rho_{water(-OH)}$ is that for OH^* in the water layer. Three-dimensional charge density difference isosurfaces of the clean and hydrogen-covered systems for the H-up and H-down structures are shown in Fig. 4.7. The charge accumulation zones (positive $\Delta\rho$), shown in yellow, are caused by electron transfer of adsorbed surface species, filling the orbitals close to the Fermi level of the metal. This leads to the charge depletion zones (negative $\Delta\rho$), shown in blue, inducing a local polarization.

Results indicate that at the clean surface the relatively strong interaction between the flat-lying water molecules (H-bonded to OH*) and the surface, creates an H_2O-Pt bond. On the other hand, at the hydrogen-covered surface there is almost no charge transfer between near-surface water molecules and the surface. Indeed, this electrostatic effect is caused by the surface hydrophobicity in the HUPD region, which renders the formation of OH^* en-

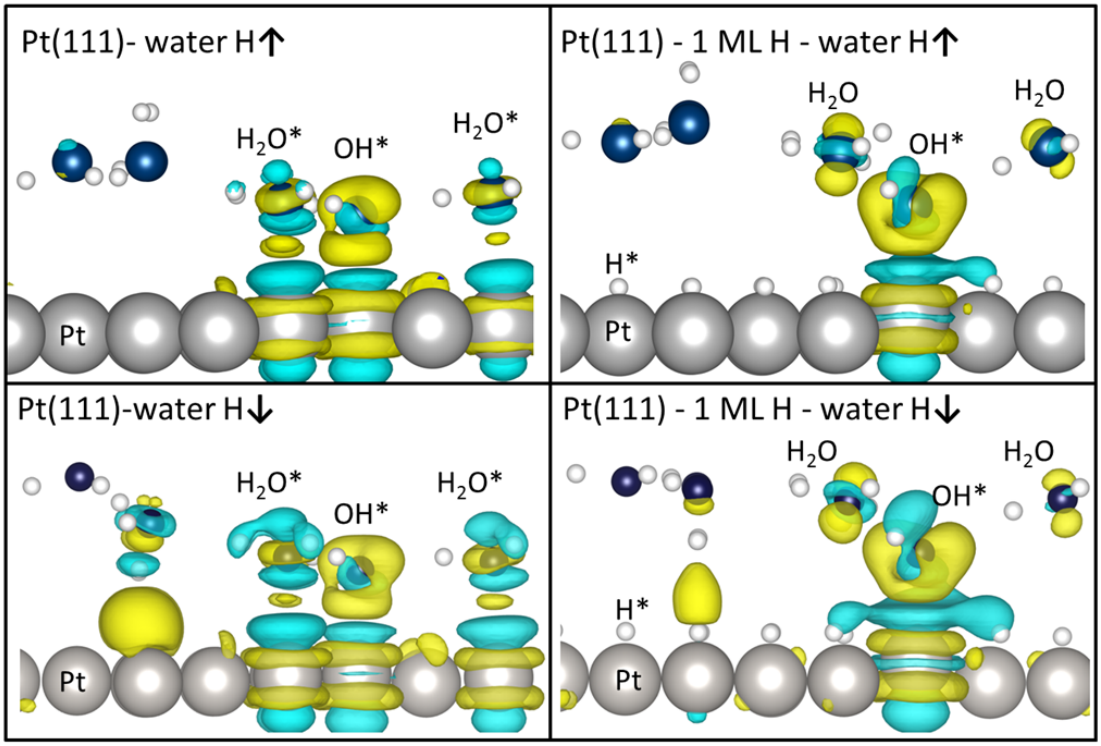

Figure 4.7: Charge density difference isosurfaces of chemisorbed OH at Pt (111), for clean surface (on left, H-up top, H-down bottom) and for 1 ML hydrogen-covered surface (on right, H-up top, H-down bottom). Yellow shows positive isosurfaces (charge accumulation zones); blue shows negative isosurfaces (charge depletion zones); gray, dark blue, and white show Pt, O and H atoms, respectively. The isosurfaces value is taken as 0.002 e per $Å^3$.

ergetically unfavorable. As a result, the decomposition of H_2O_2 to form $2OH^*$ is inhibited in the HUPD region but highly favorable at the clean surface. Similarly, the decomposition of OOH^* to $3OH^*$, catalyzed by surface water molecules, becomes highly unfavorable at the hydrogen-covered surface, but a highly favorable process at the clean surface. This interpretation is consistent with our binding energy calculations.

Moreover, we generated the FED of M1 as a function of hydrogen coverage. The $4e^-$ and the $2e^-$ ORR are compared in Fig. 4.8 at $U = 0\ V$ vs. RHE. As can be seen, at hydrogen coverage below 1/4 ML, OOH^* dissociation to $3OH^*$ becomes an energetically preferred step in comparison to H_2O_2* formation. As the hydrogen coverage increases, the dissociation of OOH^* by neighboring surface water molecules is suppressed thereby enhancing the selectivity of the process to H_2O_2 formation.

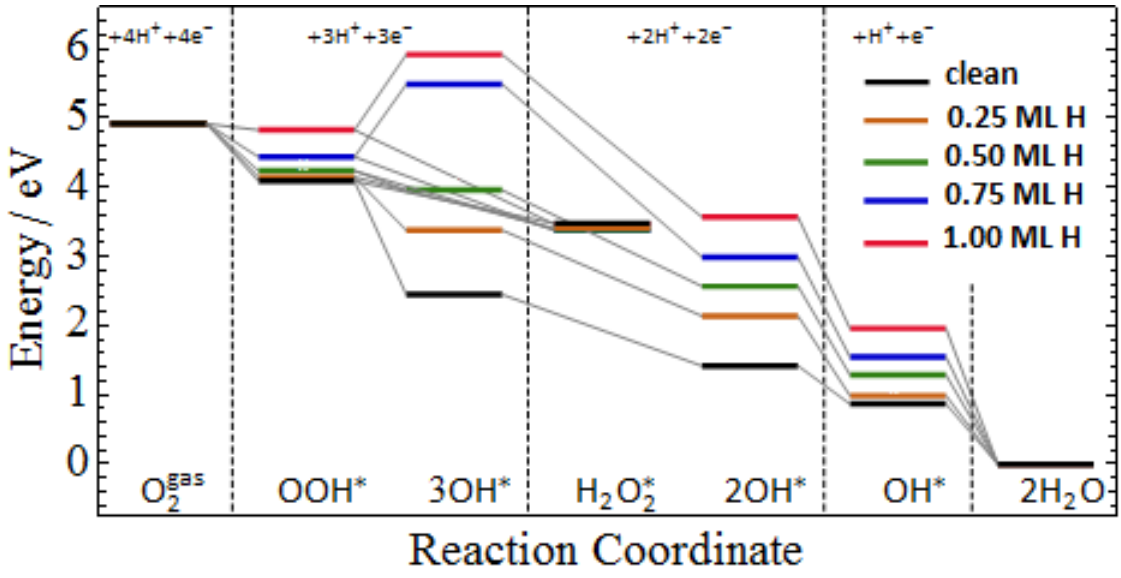

Figure 4.8: Free energy diagram of oxygen reduction reaction at Pt (111) as a function of hydrogen coverage.

4.4 Experimental Validation

Our results support a hypothesis that Pt nanodeposits present in the H_2-rich region of a PEM are responsible for the formation of H_2O_2. The H_2O_2 released from Pt in HUPD surface configuration could react with iron impurities, inevitably present in the membrane from Fe metal ion contamination originated from the end plates[59,74,82], to form $^{\bullet}$OH and thereby initiate membrane chemical degradation[57]. In addition, our studies show that the spontaneous formation of $^{\bullet}$OH at Pt nano-deposits is unlikely. It can be expected that Pt deposits will act as scavengers for $^{\bullet}$OH, which has also been reported experimentally[199].

To check these predictions, in a collaboration with an experimental group at the Institute of Engineering Thermodynamics in the German Aerospace Center (DLR), we experimentally studied the impact of electrochemical conditions at PITM on ionomer composition. The experiment was conducted by Dr. Stefan Helmly in Prof. K. Andreas Friedrich research group. Accordingly, this section presents the effect of H_2 - and O_2-rich conditions on, first the electrical potential of PITM, and second on their role on membrane degradation.

In this work, two experiments with model cells were conducted. In the first experiment, the electrochemical condition at PITM in dependence on H_2 and O_2 concentration was investigated by measuring the electrical potential of a Pt micro-electrode in a membrane electrode assembly (MEA) at various ratios of reactant concentrations. In the second experiment, the effect of electrochemical conditions at PITM on membrane degradation

was studied by operating various cells with and without PITM and with and without the electrodes. The electrochemical conditions were modulated by varying the reactant concentrations between values selected from the first experiment. To obtain a cell with typical PITM, the PEM was prepared with Pt deposits in it. Experimental details are provided in Appendix A.

In the first experiment, suitable pressure settings of the reactants were identified to locally obtain either low potential or high potential conditions at PITM. Therefore, we prepared a cell in which the microelectrode was positioned in the center ($x = 0.5$). As can be seen in Fig. 4.10, the change between low potential and high potential conditions at the microelectrode is clearly visible as the pressure ratio of oxygen to hydrogen at the membrane boundaries changes from 1.15 to 1.46.

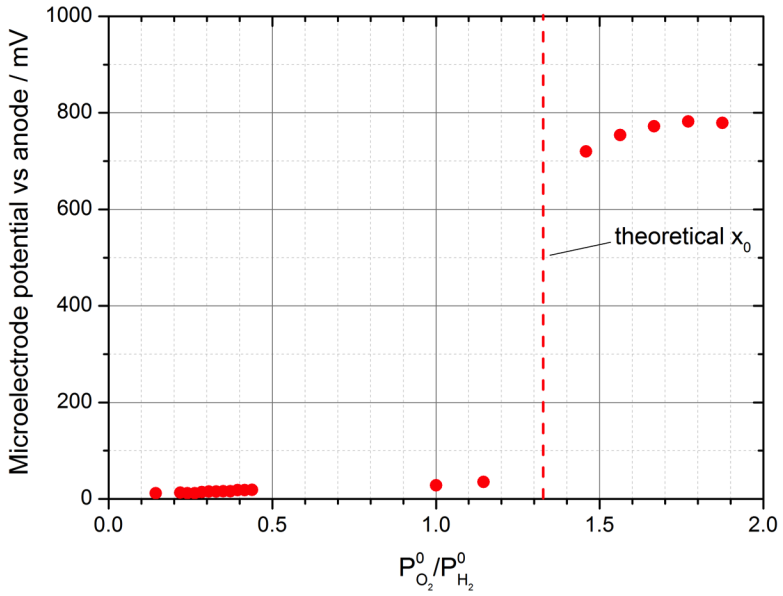

Figure 4.9: Experimental measurement of mixed potential at microelectrode caused by permeation of H_2 and O_2 in the membrane as a function of relative pressures at the membrane boundaries. Results are in agreement with the model prediction (Fig. 4.10).

Fig. 4.10 shows the plot of the potential step position as a function of the relative pressure of oxygen and hydrogen at the membrane boundaries (see eq. 3.47). As discussed in chapter 3, the step position divides the PEM into low potential region (between the anode and the step), and high potential region (between the step and the cathode). In agreement with the experiment for the micro-electrode at $x = 0.5$, the pressure ratio smaller than 1.27 leaves it in the anodic region, while the pressure ratio larger than 1.27 leaves it in the ca-

thodic region. Here, it assumed that the micro-electrode does not significantly perturb the distribution of reactant gases in the membrane.

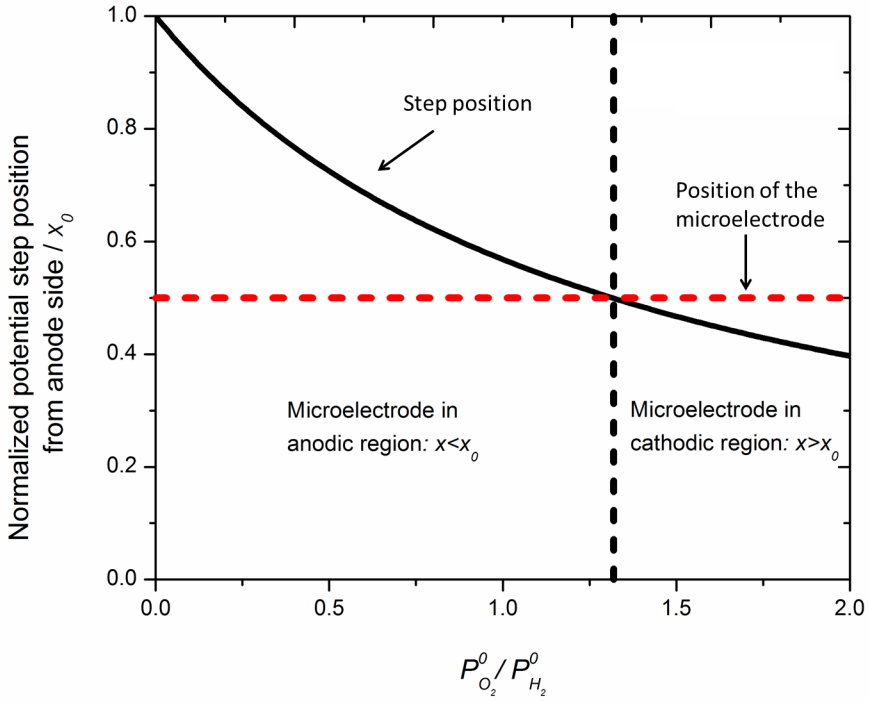

Figure 4.10: Potential step position in the membrane as a function of relative partial pressure of O_2 and H_2. For a micro-electrode at $x = 0.5$, shown as horizontal dashed line, pressure ration smaller than 1.27 leaves it in the anodic region, while pressure ratio larger than 1.27 leaves it in the cathodic condition. The distiction between the two region is shown as vertical dashed line.

In the second experiment, degradation tests were performed for cells of different configuration (with/without PITM, with/without electrodes), under two different pressure settings corresponding to the anodic and the cathodic regions. As degradation data in Fig. 4.11 show, it was found that polymer decomposition is higher for PITM in the anodic condition (pressure ratio 0.69) as compared to PITM in the cathodic condition (pressure ratio 1.46). This is consistent with our theoretical finding that in H_2-rich conditions H_2O_2 formation at Pt nanodeposits is higher. Although, membrane degradation for the cathodic conditions were clearly lower than for the anodic conditions, it has to be remarked that they vary strongly whereas the values for the anodic conditions exhibit less variation. We assume that the variation of FER in the cathodic cnditions is due to the influence of the chronological order of the experimental settings, as the setting of the pressure ratio was switched between each measurement from the anodic to the cathodic condition. Apparently, this in-

fluence could not be avoided by the delay in collecting condensate of 1-2 h after changing operation points.

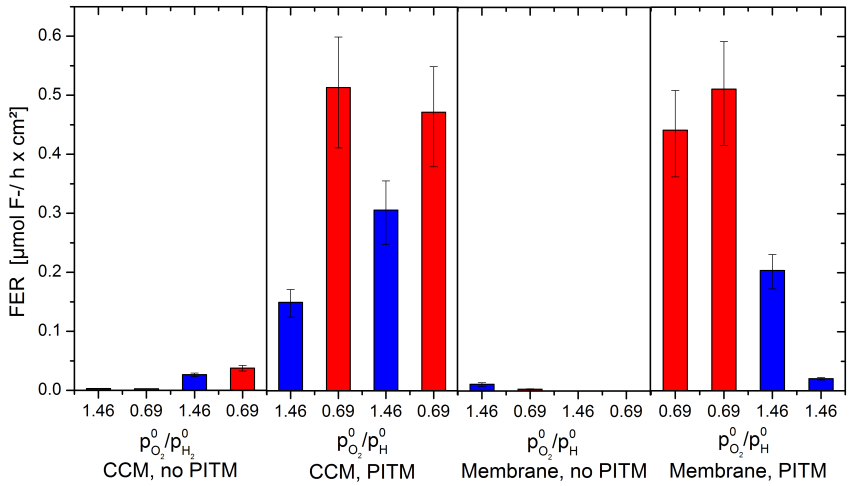

Figure 4.11: FER measurement for various cell configurations and pressure settings. In agreement with the theoretical findings, results indicate higher ionomer decomposition if PITM is present in the low potential region.

Furthermore, the fact that cells with PITM had a higher FER than the PITM-free cells indicates that membrane decomposition was not suppressed by the presence of PITM but increased under any of the conditions combined. Therefore, we are led to conclude that the conditions at PITM have a significant influence on PEM degradation; however, they are not causing an inhibiting effect on degradation as had been observed in other studies[84,91]. Apparently, this effect demands a particular particle morphology to be more precise a star or dendritic shape which means particles contain a high level of Pt(111) surfaces. In contrast, Pt particles with a cubic or spherical shape were not found to inhibit degradation[84]. As can be seen in the micrograph in Fig. 4.12, the Pt particles in the cells tested in our study had the latter structure. Thus, the inhibiting effect of PITM could not be expected.

In summary, we presented an approach to understand the role of environmental conditions around PITM on chemical degradation of the polymer electrolyte membranes in fuel cells. It was discussed that the step-like potential distribution at Pt nanodeposits divides the PEM into two regions of low potential (~ 0 V) and high potential (~ 0.8 V). The position of the potential step depends on the ratio of the partial pressure of reactant gases at the membrane boundaries, as well as the permeability properties of the PEM. This was validated by our first experimental study of local potential at Pt micro-electrode in the membrane for varying partial pressures of H_2 and O_2 at the membrane boundaries. Subsequently, in the second experiment we investigated the effect of various pressure settings (or local potential

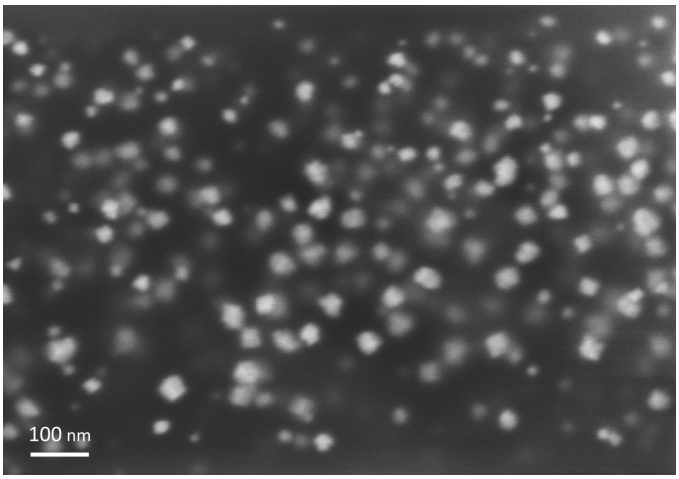

Figure 4.12: Scanning electron microscope (SEM) image of Pt nanodeposits in the membrane

at PITM) on radical-initiated membrane degradation by measuring the FER as an indicator of ionomer decomposition. Consistent with our DFT study, in these experiments we found that PITM located in the low potential region of the membrane leads to significantly higher ionomer decomposition as compared to the case where PITM is in the high potential region.

Chapter 5

DFT Study of Pt Extraction Mechanism at Oxidized (111) Surfaces

This chapter presents a density functional theory study of the atomistic mechanism for interfacial place-exchange between surface Pt atom and chemisorbed oxygen at oxidized Pt (111)-water interfaces. We generate the minimum energy pathways of the processes of Pt atom extraction, followed by the substitution of chemisorbed oxygen to the vacancy. The energy diagrams were analyzed to determine the critical coverages for the Pt extraction and O^{ads} substitution steps. The Pt extraction process depends on two essential conditions: 1. local coordination of a Pt atom by three chemisorbed oxygen atoms at the first fcc nearest neighboring sites; 2. the interaction of the buckled Pt atom with surface water molecules. From a geometrical point of view, the first condition is fulfilled at above 0.50 monolayer (ML) O at Pt (111). Substitution of O^{ads} into the vacancy created by the extracted Pt becomes thermodynamically favorable above 0.75 ML O, as next nearest neighbor hollow fcc sites around the Pt atom start to be occupied. We discuss results in terms of surface charging effects caused by oxygen coverage, surface strain effects, as well the contribution from electronic interaction effects. The utility of the proposed mechanism for the understanding of Pt stability at bimetallic surfaces will be demonstrated by evaluating the energy diagram of a Cu_{ML}/Pt (111) near-surface alloy.

5.1 Introduction

Experimental studies have found the formation of subsurface oxygen on oxidized transition metal surfaces[101,200–202]; yet, so far no coherent theoretical picture of the atomistic mechanism underlying these processes has emerged[99].

Platinum is the electrocatalytic material of choice in porous electrodes of electrochemical energy technologies such as low-temperature polymer electrolyte fuel cells (PEFC) and electrolysis cells[46]. However, it is known that typical operational conditions such as high temperature, high potential, low pH and, in particular, extensive potential cycling lead to unacceptable rates of Pt dissolution[203,204]. The kinetics of Pt dissolution in turn is correlated with loss of catalyst material, transformation of porous composite structure, decrease of active surface area, change in wettability of pore walls, decline of electrochemical performance, and ultimately the lifetime reduction of the device[13].

In spite of tremendous efforts in both experiment and theory focusing on understanding degradation issues and improving catalyst stability[40,205], the understanding of materials properties that control Pt stability and mechanisms involved in catalyst dissolution remains a controversial topic[103,206]. Especially, the comprehension of the elementary surface processes involved is still elusive.

Pt dissolution may proceed through both electrochemical and chemical pathways[48,49]. In a recent detailed experimental study, Furuya *et al.*[204] examined the influence of electrolyte composition and pH on Pt dissolution. Analysis of potential versus pH diagrams (Pourbaix diagrams) suggests that the anion nature has a negligible impact on Pt dissolution; the pH on the other hand exerts a significant impact on the dissolution kinetics[204].

The works of Topalov *et al.*[203], Xing *et al.*[207] as well as Rinaldo *et al.*[208] revealed a staggering enhancement in Pt dissolution rate by a factor 2000 during voltage cycling in accelerated stress tests when the upper potential limit of the voltage cycle was increased above 1.2 V vs. RHE. It was found consistently in these independent studies that the reduction of Pt oxide during the reduction part of the voltage cycle is responsible for the hugely increased rate of Pt dissolution. In addition, based on the in-situ electrochemical scanning tunneling microscopy (STM) observations, Wakisaka *et al.*[209] have found that the irreversible morphological changes at Pt (111) occur predominantly during the reduction phase of oxide. The underlying process is sensitive to the formation of the so-called as α-oxide phase[210] that forms as a surface layer upon ramping up the potential to values above 1.1 V vs. RHE[203].

On the other hand, there is also a much smaller amount of Pt dissolution that is found in potential hold experiments at potentials below 1.1 V vs. RHE. The rate of this process does not depend directly on the electrode potential, but it is affected by the amount of surface oxide, which in turn determines the surface excess energy or surface tension of Pt nanoparticles as well as the rate constant of dissolution[48,49].

Analysis of the cyclic voltammetry (CV) data of polycrystalline Pt in 0.5 M aqueous H_2SO_4, correlated with electrochemical quartz-crystal nanobalance data revealed that

the onset potential of surface oxidation lies at $E \approx 0.85\ V_{RHE}$ [101]. Adsorbed surface oxide at Pt formed by water oxidation is usually identified as chemisorbed oxygen (O^{ads} at $0.85 < E < 1.10 V_{RHE}$), which forms up to half of a ML coverage [101]. As the potential increases, further dissociation of water molecules forms additional O^{ads} that is susceptible to undergoing interfacial exchange with Pt surface atoms; this so-called place-exchange is a basic process involved in oxide growth [194,206,211]. In situ X-ray scattering [100], as well as STM studies under ultrahigh vacuum conditions [102] confirmed the existence of interfacial place-exchange at Pt (111). The formation of subsurface oxygen has also been observed in experiments on other oxidized transition metal surfaces [200–202].

Density functional theory (DFT), molecular dynamics (MD) and *ab initio* MD have also been employed to study involved reaction mechanisms at atomistic scales [104–107,212]. Fantauzzi *et al.* [107] have performed reactive force field (ReaxFF) MD calculations to determine the surface energies for structures with up to one monolayer of oxygen on Pt (111). Their results reveal four stable surface phases corresponding to pure adsorbate, low-coverage and high-coverage buckled, and subsurface-oxygen structures, respectively. They have found that stable phases of Pt(111) with oxygen coverage beyond 0.56 ML contains subsurface oxygen [107]. The work of Gu and Balbuena [104] suggests that the tetra-I site is the energetically preferred site for adsorption of atomic oxygen in the subsurface of Pt (111). However, the large activation barrier of 2.5 eV for the transfer of surface oxygen to this site seemed to render this place-exchange a highly unlikely event [104].

In an earlier work, Hawkins *et al.* [105] had used DFT to study the buckling of Pt atoms at oxygenated Pt (111) surfaces in vacuum conditions. They obtained minimum energy pathways (MEP) for the process of O^{ads} atom diffusing from surface fcc to buckled hcp site and then to subsurface tetra-I site at the coverages of 0.25 ML, 0.5 ML and 0.5625 ML. In their work, it was found that Pt buckling by 1.7 Å is energetically favorable at oxygen coverage of 0.5625 ML, but not at 0.50 ML or 0.25 ML coverages. However, as mentioned in their article, the MEP for higher O^{ads} coverages was not found because of the convergence failure of nudged elastic band calculations at 0.75 ML and 1.0 ML [105]. In addition, the possible role of surface water molecules in this process was not explored.

Considering that the formation of subsurface oxygen at high coverages has also been seen experimentally on other oxidized transition metal surfaces [200–202], we strive to find a universal mechanism of metal atom extraction at an oxidized Pt (111) surface and subsequent transfer of an adsorbed surface oxygen atom to the subsurface. We will discuss that the Pt extraction process depends on two essential local conditions: 1. Local coordination of Pt by three chemisorbed oxygen atoms in neighboring fcc adsorption sites; 2. the interaction of the buckled Pt surface atom with near-surface water molecules. From a geometrical

point of view, the first condition is fulfilled at above 0.50 ML O at Pt (111). Substitution of O^{ads} into the vacancy created by the extracted Pt atom becomes thermodynamically favorable at above 0.75 ML O, as next nearest neighbor hollow fcc sites around the Pt atom start to be occupied. We will demonstrate that the extracted phase is energetically more stable than the buckled phase proposed in Ref. [105].

5.2 Model System

The surface was modeled by a super-cell containing a four-layer slab of Pt (111) and a $2\sqrt{3} \times 2\sqrt{3}\,R30^o$ water layer with hexagonal structure on one side of the slab. Our model included 48 Pt atoms per slab and 8 water molecules in the unit cell. Repeated slabs were separated by a vacuum region of 15 Å. In all geometry optimizations, the two bottom layers of the slab were fixed, while the two top layers together with adsorbates and the water layer were allowed to relax. A standard dipole correction scheme [173], implemented in VASP, compensated the unphysical interaction between opposite surfaces that correspond to neighboring images across the vacuum region of the periodically repeated slab.

To account for the orientation of water molecules at the interface, we evaluated two mixed-phase water structures with 1. three H-up and one H-down as well as four flat-lying water molecules; 2. three H-down and one H-up as well as four flat-lying water molecules. We note that the preferred orientation of water molecules depends on electrode potential, oxygen adsorption state, and total surface charge density; the positively (or negatively) charged surface stabilizes the H-up (or H-down) structures [179]. In this work, we compare minimum energy pathways of the extraction mechanism for the two interfacial water structures with fixed orientation.

5.3 Results and Discussion

In view of understanding the mechanism of Pt atom extraction at oxidized (111) surfaces, we were interested in generating the energy diagram of the following sequence of elementary surface processes: (1) extraction of a Pt surface atom along the surface normal (z-coordinate) and (2) transfer of an adsorbed oxygen atom into the vacant site left by the Pt atom. For this purpose, we utilized the constrained optimization method [169,213–215]. In this technique, the z variable of the transferring atomic nucleus is constrained in defined steps, between values corresponding to the fully optimized initial and final states. At each of the z values a full geometry optimization is performed for all other degrees of freedom. This

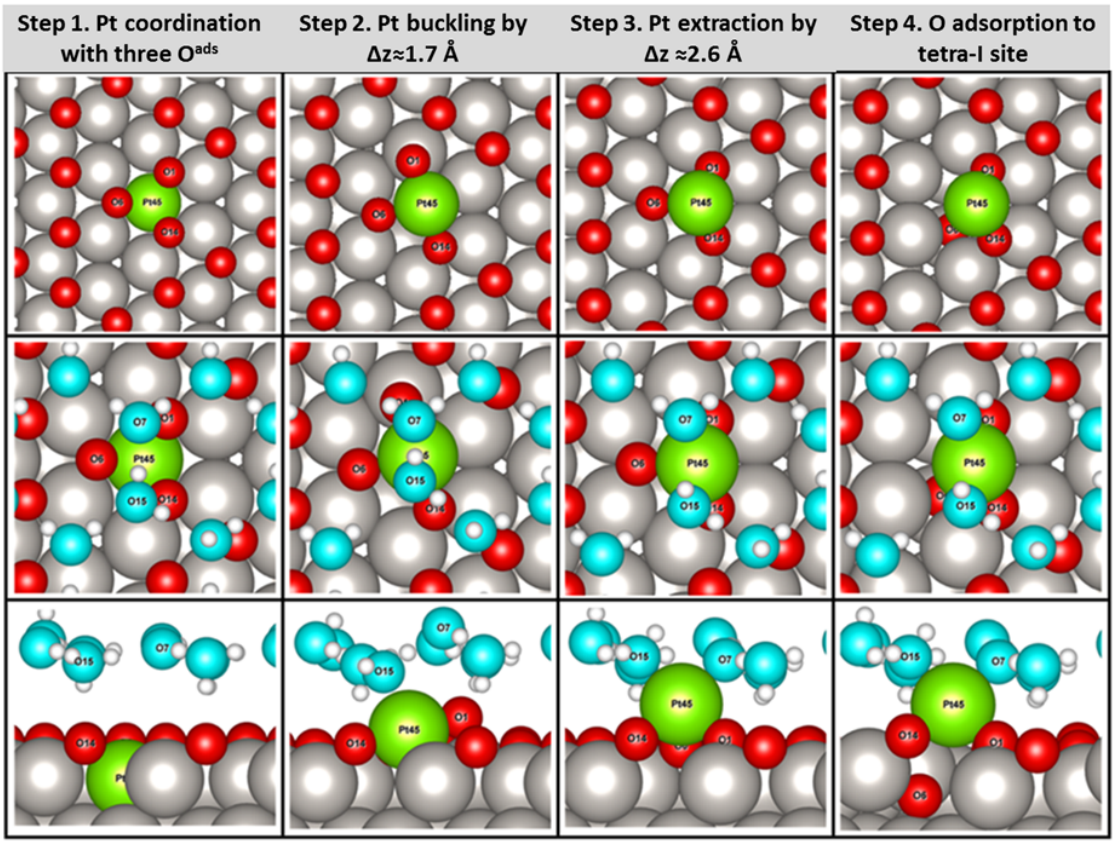

Figure 5.1: Illustration of the mechanism of Pt extraction and O substitution at oxygen-covered Pt (111); gray, red, blue, white and green colors show atoms of Pt, chemisorbed oxygen, oxygen in water layer, hydrogen and the local Pt site studied in this mechanism, respectively. Active atoms are labeled with numbers.

method allows the molecules to rotate and translate subject to the above constraint. Using this procedure, we chose equal increments of z for the Pt atom in the Pt extraction step, i.e. between the fully optimized structures with Pt atom in the initial lattice position and in the extracted state by two water molecules. Thereafter, we translated the O^{ads} atom in equal steps to also create the trajectory along z for the O^{ads} substitution step. This method is efficient and reliable under the premise that the z-coordinate represents a suitable reaction coordinate.

Fig. 5.1 illustrates the proposed mechanism of Pt atom extraction and O^{ads} substitution into the sub-layer. In the extraction step, the threefold O^{ads}-coordinated Pt (labeled as Pt45) is initially displaced by 1.7 Å from the original lattice position to assume an energetically more stable position above the surface. This phase, referred to as buckled hcp in Ref.[105], is accompanied by a lateral move of one of the neighboring oxygen atoms (labeled as O1) from its initial fcc position to the hcp site. Thereafter, two surface water molecules facilitate

the complete extraction of Pt atom with an overall displacement of 2.6 Å from the initial lattice position to reach an energetically more stable state. Following Pt extraction by 2.6 Å, one of the neighboring oxygen atoms, which was not bonded to the detached Pt atom (shown as O6 in Fig. 5.1), substitutes into the subsurface filling the tetra-I site underneath the hcp site. The energetics of these processes is sensitive to the O^{ads} coverage as will be discussed.

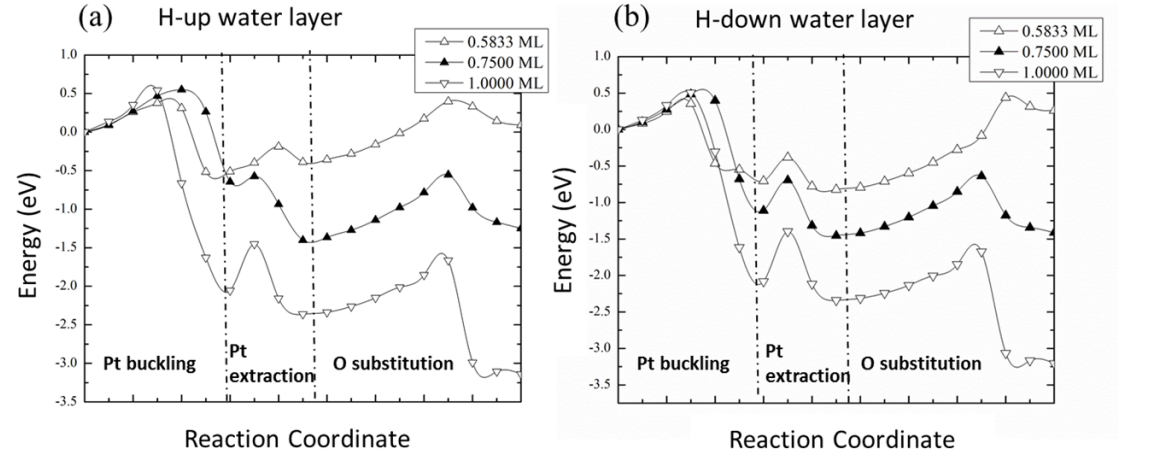

Figure 5.2: Minimum energy path for Pt extraction and O substitution at coverages above 0.50 ML O and for two opposite orientations of water layer: (a) three H-up and one H-down, (b) three H-down and one H-up

Fig. 5.2 (a) and (b) show the energy diagrams of the processes illustrated in Fig. 5.1, as a function of O^{ads} coverage and for the two opposite orientations of interfacial water layer. Comparing the energy diagrams in Fig. 5.2 (a) and (b), it is clear that the impact of O^{ads} coverage on the minimum energy pathway is dominant, while the water orientation plays a minor role. As the coverage increases above 0.5 ML, the concerted sequence of Pt extraction and O^{ads} substitution at the three-fold coordinated Pt site leads to a thermodynamically more favorable place-exchanged state. The activation barrier energies for the initial Pt buckling step (by 1.7 Å) were found to be 0.36 eV for 0.58 ML O, and 0.48 eV for 0.75 ML O, and 0.5 eV 1.0 ML O. For this step, the value of Pt displacement is in very good agreement with STM images under ultrahigh vacuum conditions showing protrusions, interpreted as buckled Pt atoms, with an apparent height of 1.7 Å[102]. Following the Pt buckling step, the destabilized Pt atom is completely extracted from the surface and displaced by 2.6 Å relative to its initial position at the surface in order to find an even more stable phase. For the extraction step, two flat-lying surface water molecules are necessary to be involved in the process of forming a chemical complex of $[PtO_2(H_2O)_2]$ at the interface. Notably, we did not find a stable phase with only one water molecule involved in

the extraction process. The 3D charge density difference isosurfaces for the $[PtO_2(H_2O)_2]$ were shown in Fig. 5.3, illustrating the electropositive (blue) and electronegative (yellow) zones that occur between the oxygen atoms of two water molecules (shown as O7 and O15) and the extracted Pt, as well as the extracted Pt and two neighboring chemisorbed oxygen atoms (shown as O1 and O14).

In the final step, the neighboring oxygen atom that was not bonded to the extracted Pt (shown as O6 in Fig. 5.1 and 5.3) transfers to the subsurface to become sorbed on the tetra-I site underneath the hcp site. This final step is also sensitive to the oxygen coverage and is only thermodynamically favorable at coverages above 0.75 ML O, as the second nearest neighbor hollow fcc sites around the Pt atom start to be occupied with O^{ads} (also see Fig. 5.5 for clarification). This finding is in agreement with the results presented in the Ref.[107]. The reaction energies corresponding to Fig. 5.2 and Pt displacements from the surface for all studied systems are provided in Table 5.1.

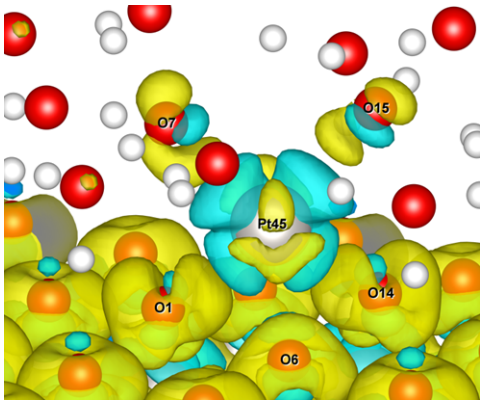

Figure 5.3: The 3D charge density difference isosurfaces of Pt45 extracted by two water molecules at 1.0 ML O^{ads}; Blue shows negative isosurfaces (charge depletion zones); yellow shows positive isosurfaces (charge accumulation zones); the isosurfaces value is taken as 0.002 e per $Å^3$.

We further explored the effect of Pt coordination with one and two chemisorbed oxygen at lower coverages on the buckling and extraction processes. Fig. 5.4 (a) shows the energy diagrams of the Pt extraction step at $\theta_O = 0.42$ ML O (where a Pt surface atom is coordinated with one O^{ads}) and at $\theta_O = 0.50$ ML O (as Pt surface atom is coordinated with two O^{ads}, also see Fig. 5.5), in comparison with that for triply coordinated Pt (at $\theta_O = 0.58$ ML O). As indicated, the formation of threefold O^{ads}-coordinated Pt atom is a critical condition for the Pt atom extraction at Pt (111), while Pt detachment from the surface is thermodynamically unfavorable for lower coverages.

Interestingly, the role of surface water molecules is indispensable to stabilize the extracted Pt atom and provide a minimum energy pathway for O^{ads} substitution. In Fig. 5.4

Table 5.1: Reaction energies and barriers of the steps of Pt buckling, Pt extraction and O^{ads} substitution (in eV) for various oxygen coverages and water orientations; Pt atom displacement valies (in Å) are relative to its initial position at surface.

	Pt	buckling		Pt	extraction		O	substitution	
Coverage	$\Delta G(eV)$	ΔG^+	ΔZ(Å)	$\Delta G(eV)$	ΔZ(Å)	ΔG^+	$\Delta G(eV)$	ΔZ(Å)	ΔG^+
0.58 MLO (Hup)	-0.51	0.38	1.36	0.12	0.38	2.45	0.48	0.79	0.09
0.58 MLO (Hdown)	-0.70	0.36	1.77	-0.12	0.32	2.49	1.08	1.26	0.26
0.75 MLO (Hup)	-0.65	0.55	1.67	-0.75	0.07	2.49	0.15	0.85	-1.24
0.75 MLO (Hdown)	-1.11	0.48	1.77	-0.35	0.42	2.60	0.04	0.82	-1.41
1.00 MLO (Hup)	-2.05	0.54	1.79	-0.31	0.60	2.69	-0.78	0.70	-3.14
1.00 MLO (Hdown)	-2.08	0.50	1.78	-0.26	0.69	2.68	-0.87	0.67	-3.21

(b), the mechanism is evaluated in the absence of a water layer. In this case, although the initial Pt buckling step remains energetically viable at $\theta_O > 0.50$ ML, the extraction step is prohibited without water molecules, i.e., there is no stable phase for the extraction step; moreover, without surface water molecules, O^{ads} substitution involves a large activation barrier of 1 eV which renders the substitution step unlikely.

We discuss the surface charging behavior at oxidized Pt(111) slightly below and above the critical coverage of 0.50 ML. Fig. 5.5 (a)-(e) illustrate the most stable oxygen surface atom configurations for O^{ads} coverages, ranging from 0.42 to 1.0 ML. As θ_O increases in this range, the calculated average Bader charge[198] per atom of the surface Pt layer grows from 0.27 e per atom to 0.67 e per atom (see Table 5.2), where e is the elementary charge.

For $\theta_O > 0.50ML$, local Pt sites appear (shown as Pt45 in Fig. 5.5) that are coordinated by chemisorbed oxygen atoms in each adjacent three-fold hollow fcc site. This state of high local O^{ads} coordination induces electronic charge depletion at triply coordinated Pt surface atoms that exceeds 0.7 e. The magnitude of the electronic charge depletion is larger for triply coordinated Pt as compared to doubly (0.49 e/Pt) or singly (0.26 e/Pt) coordinated Pt (see Table 5.2). Plots in Fig. 5.5 (f)-(j) show isosurfaces of the charge density difference, defined as

$$\Delta\rho = \rho_{total} - \rho_{slab} - \rho_{ads}, \tag{5.1}$$

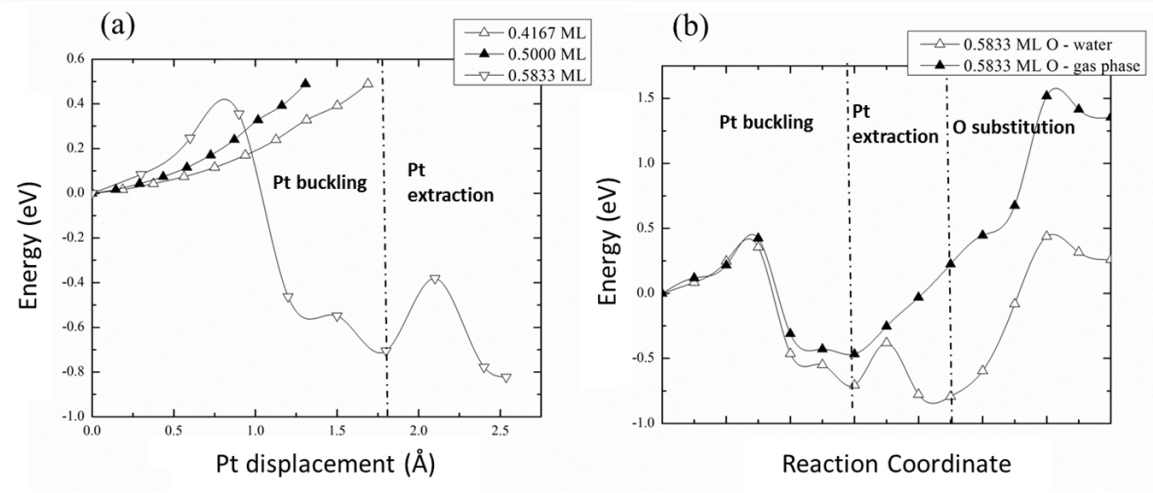

Figure 5.4: (a) Comparison between the minimum energy path for Pt extraction at oxygen coverage below and above 0.50 ML O. (b) Comparison between the minimum energy path for Pt extraction and O substitution with and without water layer at 0.58 ML O^{ads}.

where, ρ_{total} is the charge density of the total system; ρ_{slab} and ρ_{ads} are separately calculated charge densities for the bare slab and adsorbed oxygen atoms fixed in their positions in the overall system, respectively. The isosurfaces in Fig. 5.5 (f)-(j) illustrate the charge transfer that has occurred between Pt surface and chemisorbed oxygen atoms. Electronegative zones (yellow) are created by electron transfer from Pt atoms to chemisorbed oxygen atoms, which lead to the electropositive zones at surface Pt atoms (blue). As shown, as the Pt site is coordinated with three oxygen atoms for coverages above 0.50 ML, it becomes more electropositive inducing a larger local polarization at the site.

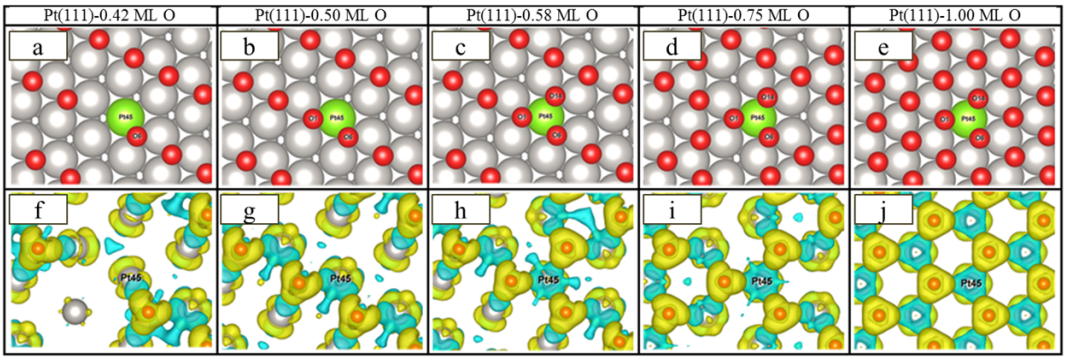

Figure 5.5: (a)-(e) Top views of the most stable O surface atom configurations for coverage of (a) 0.42 ML, (b) 0.50 ML, (c) 0.58 ML, (d) 0.75 ML and (e) 1.0 ML; gray and red colors are used to represent Pt and O^{ads}, respectively. Green shows the local Pt atom, labeled as Pt45, which participates in the mechanism of extraction. (f)-(j) show the corresponding top views of the charge density difference isosurfaces of chemisorbed oxygen at Pt (111). Blue shows negative isosurfaces (charge depletion zones); yellow shows the positive isosurfaces (charge accumulation zones); the isosurfaces value is taken as 0.002 e per $Å^3$.

Table 5.2: Bader analysis of surface charge for various oxygen coverage (in units of an electron, e) for the top and bottom Pt layers of the (111) structure and for the active Pt site studied in this work (shown as Pt45). The charge is reported relative to the corresponding uncharged atom.

	0.42 ML O	0.50 ML O	0.58 ML O	0.75 ML O	1.00 ML O
Average induced charge per atom on top Pt layer (e) for reference system	0.2730	0.3334	0.3878	0.5097	0.6683
Average induced charge per atom on bottom Pt layer (e) for reference system	-0.0634	-0.0719	-0.0578	-0.084	-0.049
Average induced charge per atom on bottom Pt layer (e) for Pt extracted system	- - -	- - -	-0.0444	-0.0572	-0.0335
Average induced charge per atom on bottom Pt layer (e) for O substituted system	- - -	- - -	-0.0562	-0.0550	-0.0457

To rationalize the local driving force for the Pt extraction process, we estimated the z-component of the local dipole moment at Pt45. The simulated slab is asymmetric with surface oxide formed only at one side. This asymmetry causes a redistribution of charge between the two slab surfaces. The net amount of the total surface charge can be determined after application of the dipole correction to eliminate the electric field between periodic images of the slab. We determine the total surface charge, Q, induced by this correction for the oxide-free backside of the simulated slab. For electroneutrality, an equal but opposite total amount of charge, - Q, must be deposited at the oxide side of the slab. For simplicity, we assume that this total charge is distributed in equal amounts over the surface Pt atoms at the oxygen-side of the slab, corresponding to a value of $-Q/n$ per surface atom, where n = 12 is the number of surface Pt atoms per unit cell. We are interested in the local dipole moment induced by oxide formation at the Pt45 site. We determine the Bader charge[198] for this atom relative to the corresponding uncharged atom, qPt45, and obtain the induced oxide dipole charge as $q = qPt45 + Q/n$. As for the dipole length we use the distance dz along z from the center of Pt45 to the plane of the adsorbed oxygen atoms coordinated to this site. The dipole moment is calculated as $\mu_{45} = qdz$. Using the same method, we calculated the local dipole moment between the extracted Pt site and two involved surface water molecules after completion of the Pt extraction and O^{ads} substitution steps, in order to estimate the net dipole moment for these phases (see Table 5.3). Values of μ_{45} were shown in Table 5.3 for the different oxide coverages considered.

Table 5.3: Bader analysis for the active Pt site studied in this work (shown as Pt45) for various oxygen coverage (in units of an electron, e) . The charge is reported relative to the corresponding uncharged atom. Induced oxide dipole charge at Pt45 (δq) and distance along z from the center of Pt45 to the plane of the adsorbed oxygen atoms, as well, adsorbed water molecules coordinated to this site (dz) are shown. Values of estimated net z-component of the local dipole moment at the extraction site are shown indicating the direction towards or away from the surface.

	0.42 ML O	0.5 ML O	0.58 ML O	0.75 ML O	1.0 ML O
qPt45 (e) for reference system	0.2643	0.4894	0.7165	0.7026	0.7282
qPt45 (e) for Pt extracted system	- - -	- - -	0.9904	1.0184	1.0624
qPt45 (e) for O substituted system	- - -	- - -	0.8896	0.9070	0.9874
δq (e) for reference system	0.2009	0.4175	0.6587	0.6186	0.6792
δq (e) for Pt extracted system	- - -	- - -	0.9460	0.9612	1.0289
δq (e) for O substituted system	- - -	- - -	0.8334	0.8520	0.9417
dz (PtO) () for reference system	1.19	1.04	1.12	1.21	1.24
dz (PtO) () for Pt extracted system	- - -	- - -	1.19	1.20	1.17
dz (PtO) () for O substituted system	- - -	- - -	1.20	1.25	1.38
dz (PtH2O) () for Pt extracted system	- - -	- - -	1.36	1.47	1.54
dz (PtH2O) () for O substituted system	- - -	- - -	1.32	1.41	1.30
μ45 (D) for reference system	1.15 $\downarrow$	2.09 $\downarrow$	3.54 $\downarrow$	3.60 $\downarrow$	4.05 $\downarrow$
μ45 (D) for Pt extracted system	- - -	- - -	0.16 $\downarrow$	0.26 $\downarrow$	0.38 $\downarrow$
μ45 (D) for O substituted system	- - -	- - -	0.10 $\downarrow$	0.14 $\downarrow$	0.08 $\uparrow$

The calculated dipole moments are consistent with values reported in Ref.[206]. Upon coordination of Pt45 with three O^{ads}, a strong local dipole moment ($> 3.5D$) directed towards the surface occurs, which destabilizes Pt45 and leads to its extraction from the surface. As a result of Pt extraction and O substitution, the local dipole moment drops to much smaller values (about 0.1 D) and eventually changes orientation at high oxide coverage of 1.0 ML, thereby stabilizing the surface at the site, at which Pt extraction and O^{ads} substitution have occurred. Furthermore, we generated the planar average of the induced charge density along the surface normal for various coverages shown in Fig. 5.6 (a). The plots were obtained by calculating the difference between the total plane-averaged charge density of the interfacial system and separately obtained charge densities of the Pt slab and the adsorbates (defined as $\Delta\lambda$) as a function of z. The adsorption of oxygen induces a large polarization at the interface with the dipole moment directed towards the surface. However, as shown in Fig. 5.6 b , Pt extraction and O^{ads} substitution steps modify the surface dipole moment, which as discussed results in obtaining a thermodynamically more stable state.

The surface potential energy is a function of the charge density distribution, which varies with coverage. Work function, Φ (in eV), is the energy required to bring an electron from inside of the slab to the vacuum and it is defined as the energy difference between the Fermi energy, E_f, and the electrostatic potential in the middle of the vacuum level, E_{vac},

$$\Phi = E_f - E_{vac}. \tag{5.2}$$

The surface adsorption state affects the work function; we calculated Φ as the difference between the potential energy of an electron in the middle of the vacuum and E_f in the middle of the slab. Fig. 5.6 c shows Φ as a function of oxygen coverage for the 2×2 Pt(111) reference systems. The work function increases with increasing coverage due to the positive charge carried on the surface layer of Pt atoms.

Coverage by oxygen also affects the surface strain as well as the electronic interactions. We studied the effect of coverage on the lateral strain using a 2×2 Pt (111) system. For this aim, structural optimizations of the slab for varying unit cell parameter were carried out in order to find the energy profiles as a function of the lateral strain. As shown in Fig. 5.7, results suggest that for coverage > 0.50 ML surface contraction is favored, with a maximum of 3 % at 1.0 ML; but, below < 0.50 ML O lateral expansion is favored. This result is also in agreement with the recent DFT study by Li *et al.*[216]

To understand the effect of oxygen coverage on the electronic interactions, we utilized the d-band model developed by Hammer and Nørskov[217]. This model predicts the trends in the adsorption binding energies of various adsorbates on the metal surfaces. An upshift in

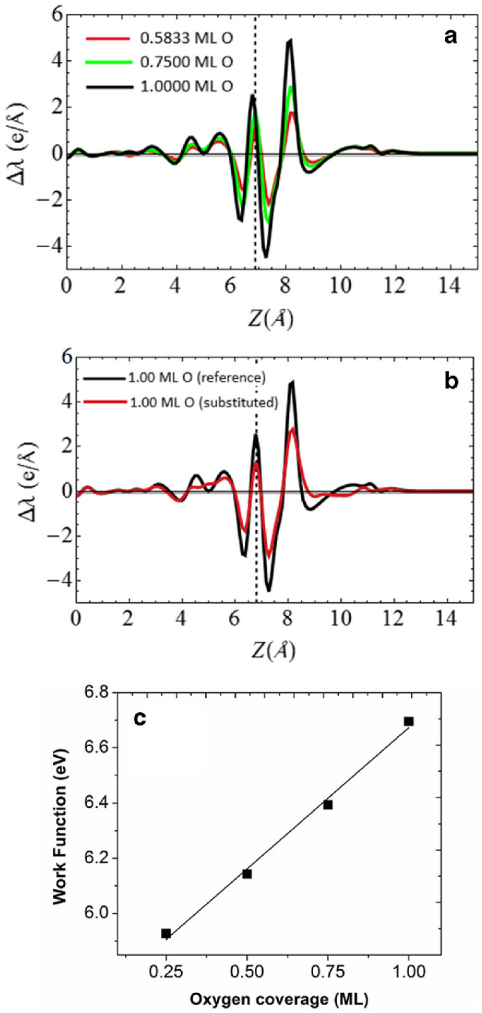

Figure 5.6: Comparison between the planar average of the induced charge density along the surface normal for (a) oxygen coverage above 0.50 ML; and (b) for surface covered with 1.0 ML O and with one O substituted surface Pt.

the average energy of the d-states relative to the Fermi level, so-called as the d-band center, results in a stronger interaction between surface atoms and adsorbates. We first calculated the binding energy of oxygen as a function of coverage for a 2×2 Pt (111) system using the following equation,

$$\Delta E = E_{slab+nO} - E_{slab} - n/2E_{O_2}, \tag{5.3}$$

where, n is the number of oxygen atoms in the unit cell, and E_{O_2} was considered as 5.87 eV[218]. As shown in Fig. 5.8 (a), increasing the oxygen coverage lowers the strength of the interaction of oxygen with the surface and results in decreasing the binding energy. We also performed density of states (DOS) calculations which is common for understanding

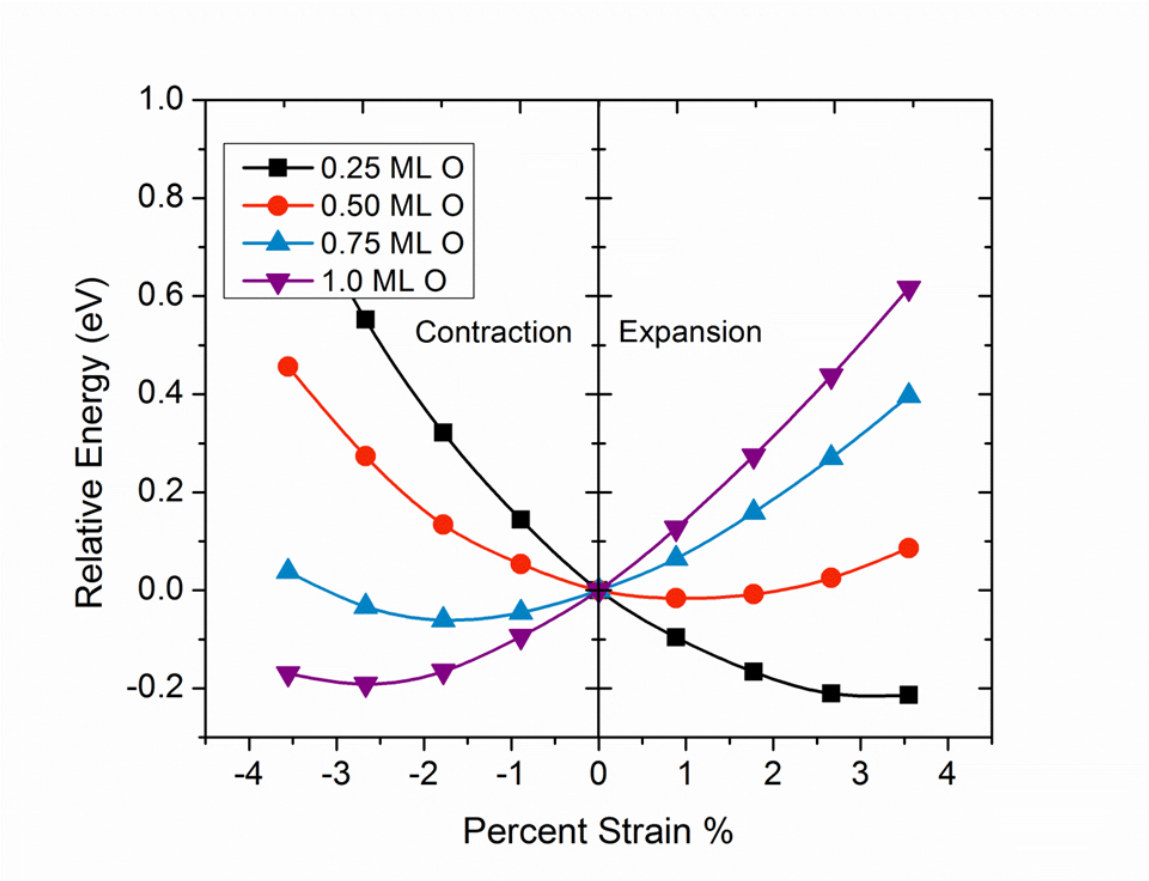

Figure 5.7: Percent surface strain caused by oxygen coverage at Pt (111). The energy profile is relative to the slab optimized in its bulk lattice constant. Coverage above 0.5 ML O results in surface contraction and coverage below 0.5 ML O leads to surface expansion.

the characteristics of the chemical bonding. DOS analyses provide information about the distribution of electronic states at energy bands in periodic systems. To determine the electronic state for a particular ion in a system, the projected density of states (PDOS) is analysed, where the DOS is projected onto the atomic orbitals. Fig. 5.8 (b) shows the d-projected density of states (DOS) of surface Pt atoms as a function of coverage for a 2×2 (111) system. The d-band is narrower and higher in energy for the clean surface and as the coverage increases the d-band center shifts down to more negative values. Consistently, as shown in Fig. 5.8 (c), the downshift in the d-band center with coverage lowers the strength of interaction of oxygen with the surface.

Furthermore, we examined the proposed mechanism of Pt extraction for a Cu_{ML}/Pt(111) near-surface alloy system. Fig. 5.9 compares the energy diagrams for the Pt extraction and O^{ads} substitution processes on Cu_{ML}/Pt(111) with that of Pt(111) at $\theta_O = 0.58ML$. For this coverage, the extraction energy for Cu_{ML}/Pt(111) was found to be -0.17 eV while that for

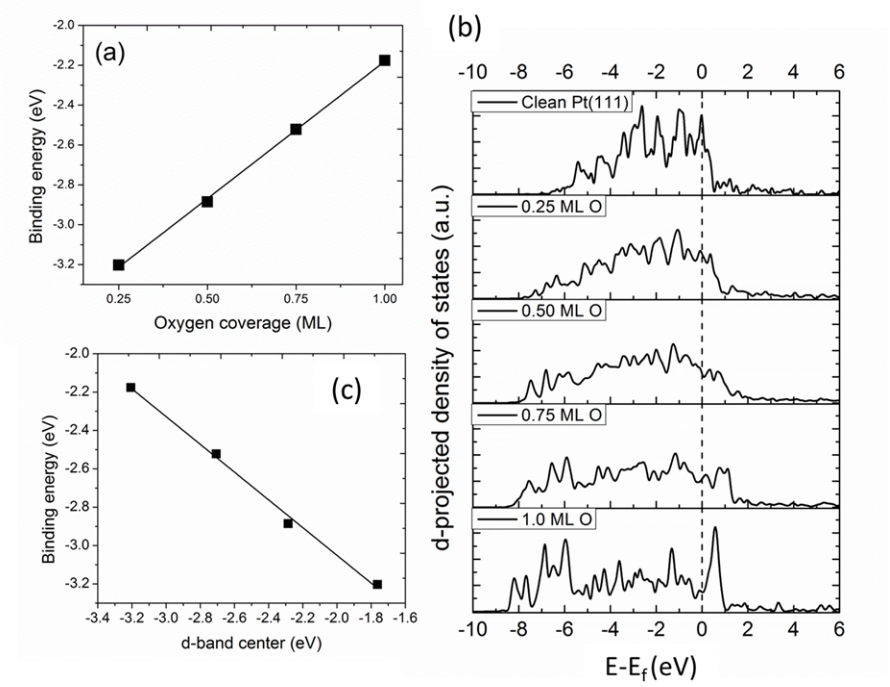

Figure 5.8: (a) Calculated oxygen binding energy for varying oxygen coverage at Pt(111). (b) d-projected density of states of surface Pt atoms for varying oxygen cover age at Pt(111). (c) V ariations in the binding energy of oxygen as a function of the d-band center of surface atoms

Pt(111) was obtained as -0.82 eV. In addition, the activation barrier for the buckling step at Cu_{ML}/Pt(111) was obtained as 0.63 eV which is larger as compared to 0.36 eV for Pt(111). Results suggest that the extraction is both kinetically and thermodynamically less favored for the Cu_{ML}/Pt(111) system. Indeed, a recent study have reported the noticeable enhancement in the Pt stability of Cu_{ML}/Pt(111)[219]. In the future, we will continue this study to obtain a relation between the extraction energy and segregation energy for near-surface alloys with a range of different metals in the sub-layer, in order to unravel systematic trends in the stability of these systems.

Overall, the results presented in this chapter are very insightful for the understanding of the atomistic details of Pt dissolution under electrochemical conditions which is of both fundamental and applied importance. The approach of anionic species from the solution could fulfill a similar role as interfacial water dipoles in enabling the Pt extraction process. We expect that the proposed re-interpretation of interfacial place-exchange as a local process will make it possible to extend the proposed mechanism to different Pt surface structures, ordered or disordered, toward understanding the mechanisms of Pt dissolution and predicting the stability of various surface structures.

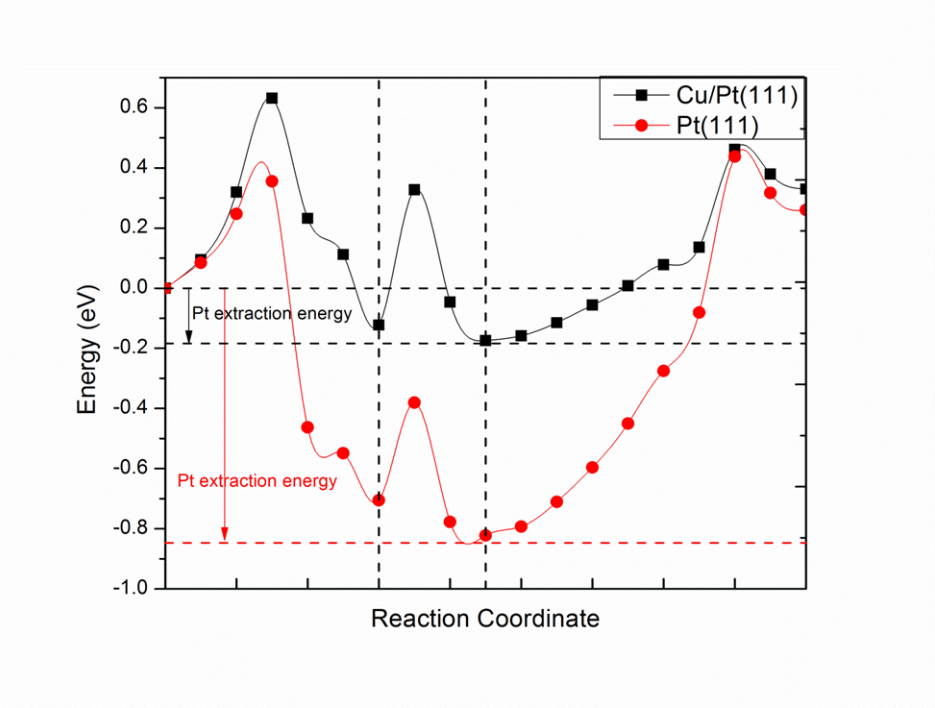

Figure 5.9: Comparison between the energy diagram s of Pt extraction and O ads substitution mechanism for Cu_{ML} - Pt(111) and Pt(111)

Chapter 6

Conclusions and Outlook

In this work, we studied the impact of electrochemical conditions around Pt nanodeposits in the membrane on the formation of membrane degrading species. Pt nanodeposits, which originate from Pt degradation in the cathode catalyst layer, provide catalytic sites for the production of membrane degrading species. Among them hydrogen peroxide is of particular importance. Decomposition of hydrogen peroxide at iron impurities in the membrane (via Fenton's reaction), leads to the formation of hydroxyl radical which attack the weak bonds of ionomers and degrade them chemically. Chemical degradation weakens the mechanical properties of the membrane, which results in the formation of pinholes, cracks and fractures in the membrane. Membrane-spanning fractures facilitate the higher crossover of the reactant gases and eventually lead to fuel cell failure.

Understanding the impact of Pt nanoparticles on the formation/deactivation of reactive oxygen species in an electrolyte involves a complex phenomenology of local conditions and structure of the electrolyte, as well as structure-dependent transport and reaction processes at solid Pt deposits. For this aim, we developed a multi-step theoretical approach:

In chapter 3, we presented a physical-analytical model to determine the potential distribution at spherical Pt nanodeposits in the polymer electrolyte membrane. The approach incorporates a continuum description of crossover fluxes of reactant gases at the macroscale, coupled with the kinetics of electrochemical surface reactions at Pt nanodeposits. The potential distribution is obtained as a function of the local composition of the PEM, which is given by concentrations of H_2 and O_2 as well as the size and density distribution of Pt particles. In good agreement with experimental data, the model predicts a step-like potential profile. In the anodic region of the PEM, the potential is close to the equilibrium potential of the HOR. In the cathodic region, the potential is closer to the equilibrium potential of the ORR. For a uniform distribution of Pt particles, the position of the step is only determined

by the relative partial pressures of H_2 and O_2 at the membrane interfaces as well as their permeation properties in the PEM.

Given the local potential at Pt nanoparticles as a variable to determine their surface adsorption state, in the second step of this approach, we presented DFT study of the processes of hydrogen peroxide and hydroxyl radical formation at clean, hydrogen-covered, and partaly oxygen-covered Pt (111)-water interfaces. We distinguished three adsorption regimes, which are discernible in the cyclic voltammograms that span the appropriate potential range of Pt based catalysts. Results demonstrate that in the HUPD potential region the rate of the 2 e- reduction of O_2 to H_2O_2 is strongly enhanced due to effective inhibition of the 4 e- ORR. In this region, the metal surface is found to be strongly hydrophobic, in agreement with findings reported earlier by experimentalists. We also found that solid deposits of Pt will always tend to scavenge $^{\bullet}$OH. In addition, if present in the solution due to external sources, H_2O_2 will be decomposed at clean or partially-oxide covered surfaces but not at the hydrogen-covered surface. This effect is caused by surface hydrophobicity in this region and weaker interaction of water molecules with the surface rendering the formation of chemisorbed OH thermodynamically unfavorable.

We generated the energy diagrams corresponding to $2e^-$ and $4e^-$ ORR, as well the diagrams corresponding to H_2O_2 reduction at clean, hydrogen-covered, and partially oxygen-covered Pt(111) - water interfaces. It was found that the coverage by hydrogen considerably affects the ORR pathway leading to a $2e^-$ reduction of oxygen and formation of H_2O_2 for this surface state. On the clean surface, however, the peroxide formation is negligible and the 4e- pathway to water formation is thermodynamically preferred. We conclude that surface coverage with hydrogen at Pt deposits, expected in the low potential region of the membrane, results in significant H_2O_2 formation which in turn leads to higher membrane degradation in the H_2-rich region of the membrane. Subsequently, in the second experiment we validated this finding by investigating the effect of various pressure settings on PITM-mediated membrane chemical degradation and measuring the fluoride emission rate as the indicator of ionomer decomposition. Consistently, in these experiments we found that PITM located in the low potential region of the membrane leads to significantly higher ionomer decomposition as compared to the case where PITM is in high potential region.

Overall, this work expanded the fundamental understanding of radical-initiated membrane degradation. We identified the reaction regimes at PITM, which determine their local potential in the membrane. Next, we studied the ORR reaction pathways corresponding to the given local condition at PITM. The obtained results are consistent with the experimental study about the role of electrochemical environment around PITM on the ionomer decomposition. This work can be linked to a kinetic model to calculate the effective rates of

radical production at PITM by incorporating the local conditions obtained in the first step. For this purpose, the activation energies should be calculated from a DFT study. Next, the model can be incorporated to a more general membrane durability model that can predict membrane lifetime as a function of operating conditions and load cycles. Understanding obtained from this study, moreover, can help in developing, testing and implementing strategies for improving membrane durability at the materials science and engineering design level.

In chapter 5, we proposed a new mechanism of Pt extraction and O^{ads} substitution that depends on stringent local selection criteria: (i) the destabilization of surface Pt atoms by the formation of chemisorbed O^{ads} in three adjacent fcc adsorption sites and (ii) the presence of surface water molecules to stabilize the extracted Pt. Results suggest that the extraction mechanism is favored above 0.5 ML O, where the first criteria is fulfilled. O^{ads} substitution to the vacancy left by the extracted Pt, on the other hand, is thermodynamically favorable above 0.75 ML O, as the second fcc nearest neighbors of the Pt site start to be occupied by oxygen. We discussed that the strong induced local dipole moment is the main driving force for Pt extraction; in addition, the role of surface water molecules is essential to stabilize the extracted Pt atom and provide a minimum energy path for the O^{ads} substitution.

Moreover, we studied the effect of oxygen coverage on surface strain and electronic interactions. Increase in the coverage above 0.5 ML O results in surface contraction, while for coverages below 0.5 ML O surface expansion is favored. The increase of the coverage also shifts the d-band center down and leads to lowering the binding energy of oxygen. Moreover, we generated the energy diagram of Pt extraction and O^{ads} substitution for Cu_{ML}/Pt(111) system. As compared to Pt(111), it was found that the Pt extraction from the Cu_{ML}/Pt(111) surface is both kinetically and thermodynamically less favored for this system caused by the stronger interaction between Pt surface atoms and Cu subsurface atoms.

Information obtained from the energy diagrams of the Pt extraction and O substitution processes can be used as input for the kinetic modelling of oxide formation and growth on Pt. As discussed, Pt dissolution is dramatically enhanced during the reduction phase of oxide. Thus, with a full dynamic model of oxide formation and reduction, the side reaction of Pt dissolution during the reduction phase can be integrated and analyzed, creating a link between a DFT-based oxide growth models and dissolution models.

Likewise, DFT is considered to be the theory at zero temperature and pressure. However, in reality catalysts in PEFCs work under harsh operational conditions (high pressures and temperatures). Therefore, DFT results need to be combined with statistical thermo-

dynamics to account for the effects of pressure and temperature. The statistical thermodynamic properties of the system can be described by the Gibbs free energy, which is a function of the number of Pt and adsorbed oxygen atoms, as well as temperature and pressure.

Bibliography

[1] N. S. Lewis and D. G. Nocera, "Powering the planet: Chemical challenges in solar energy utilization," *Proceedings of the National Academy of Sciences*, vol. 103, no. 43, pp. 15729–15735, 2006.

[2] T. R. Cook, D. K. Dogutan, S. Y. Reece, Y. Surendranath, T. S. Teets, and D. G. Nocera, "Solar energy supply and storage for the legacy and nonlegacy worlds," *Chemical reviews*, vol. 110, no. 11, pp. 6474–6502, 2010.

[3] C. C. McCrory, S. Jung, I. M. Ferrer, S. M. Chatman, J. C. Peters, and T. F. Jaramillo, "Benchmarking hydrogen evolving reaction and oxygen evolving reaction electrocatalysts for solar water splitting devices," *Journal of the American Chemical Society*, vol. 137, no. 13, pp. 4347–4357, 2015.

[4] M. S. Whittingham and T. Zawodzinski, "Introduction: Batteries and fuel cells," *Chemical reviews*, vol. 104, no. 10, pp. 4243–4244, 2004.

[5] M. L. Perry, T. F. Fuller, *et al.*, "A historical perspective of fuel cell technology in the 20th century," *Journal of Electrochemical Society*, vol. 149, no. 7, pp. S59–S67, 2002.

[6] W. R. Grove, "Xxiv. on voltaic series and the combination of gases by platinum," *The London and Edinburgh philosophical magazine and journal of science*, vol. 14, no. 86, pp. 127–130, 1839.

[7] W. R. Grove, "On the gas voltaic battery. experiments made with a view of ascertaining the rationale of its action and its application to eudiometry," *Philosophical Transactions of the Royal Society of London*, vol. 133, pp. 91–112, 1843.

[8] C. F. Schönbein *The London and Edinburgh philosophical magazine and journal of science*, vol. 14, no. 3, p. 43, 1839.

[9] V. Gold, *Compendium of chemical terminology*. Blackwell scientific publications, 1987.

[10] F. Barbir, *PEM fuel cells: theory and practice*. Academic Press, 2012.

[11] J. Larminie, A. Dicks, and M. S. McDonald, *Fuel cell systems explained*, vol. 2. Wiley New York, 2003.

[12] W. Grubb and L. Niedrach, "Batteries with solid ion-exchange membrane electrolytes ii. low-temperature hydrogen-oxygen fuel cells," *Journal of the Electrochemical Society*, vol. 107, no. 2, pp. 131–135, 1960.

[13] M. Eikerling and A. Kulikovsky, *Polymer Electrolyte Fuel Cells: Physical Principles of Materials and Operation*. CRC Press, 2014.

[14] M. Turco, A. Ausiello, and L. Micoli, *Treatment of Biogas for Feeding High Temperature Fuel Cells: Removal of Harmful Compounds by Adsorption Processes*. Springer, 2016.

[15] R. B. Gupta, *Hydrogen fuel: production, transport, and storage*. Crc Press, 2008.

[16] K. S. Joya, Y. F. Joya, K. Ocakoglu, and R. van de Krol, "Water-splitting catalysis and solar fuel devices: Artificial leaves on the move," *Angewandte Chemie International Edition*, vol. 52, no. 40, pp. 10426–10437, 2013.

[17] *U.S. DOE National Renewable Energy Laboratory, Fuel Cell Buses in U.S. Transit Fleets: Current Status, 2012, http://www.energy.gov/sites/prod/files/2014/03/f12/fceb_status_2012.pdfJ*.

[18] M. M. Mench, E. C. Kumbur, and T. N. Veziroglu, *Polymer electrolyte fuel cell degradation*. Academic Press, 2011.

[19] V. A. Sethuraman, J. W. Weidner, A. T. Haug, and L. V. Protsailo, "Durability of perfluorosulfonic acid and hydrocarbon membranes: effect of humidity and temperature," *Journal of the Electrochemical Society*, vol. 155, no. 2, pp. B119–B124, 2008.

[20] B. Smitha, S. Sridhar, and A. Khan, "Solid polymer electrolyte membranes for fuel cell applications—a review," *Journal of membrane science*, vol. 259, no. 1, pp. 10–26, 2005.

[21] U. Paulus, A. Wokaun, G. Scherer, T. Schmidt, V. Stamenkovic, V. Radmilovic, N. Markovic, and P. Ross, "Oxygen reduction on carbon-supported pt-ni and pt-co alloy catalysts," *The Journal of Physical Chemistry B*, vol. 106, no. 16, pp. 4181–4191, 2002.

[22] V. R. Stamenkovic, B. Fowler, B. S. Mun, G. F. Wang, P. N. Ross, C. A. Lucas, and N. M. Markovic, "Improved oxygen reduction activity on pt3ni(111) via increased surface site availability," *Science*, vol. 315, no. 5811, pp. 493–497, 2007.

[23] C. Wang, D. Li, M. Chi, J. Pearson, R. B. Rankin, J. Greeley, Z. Duan, G. Wang, D. Van der Vliet, K. L. More, *et al.*, "Rational development of ternary alloy electrocatalysts," *The Journal of Physical Chemistry Letters*, vol. 3, no. 12, pp. 1668–1673, 2012.

[24] X. Tan, S. Prabhudev, A. Kohandehghan, D. Karpuzov, G. A. Botton, and D. Mitlin, "Pt–au–co alloy electrocatalysts demonstrating enhanced activity and durability toward the oxygen reduction reaction," *ACS Catalysis*, vol. 5, no. 3, pp. 1513–1524, 2015.

[25] A. Dicks and J. Larminie, "Fuel cell systems explained," 2000.

[26] H. Gasteiger, J. Panels, and S. Yan, "Dependence of pem fuel cell performance on catalyst loading," *Journal of Power Sources*, vol. 127, no. 1, pp. 162–171, 2004.

[27] I. D. Raistrick, "Electrode assembly for use in a solid polymer electrolyte fuel cell," Oct. 24 1989. US Patent 4,876,115.

[28] M. S. Wilson and S. Gottesfeld, "Thin-film catalyst layers for polymer electrolyte fuel cell electrodes," *Journal of applied electrochemistry*, vol. 22, no. 1, pp. 1–7, 1992.

[29] J. Zhang, Y. Mo, M. Vukmirovic, R. Klie, K. Sasaki, and R. Adzic, "Platinum monolayer electrocatalysts for o2 reduction: Pt monolayer on pd (111) and on carbon-supported pd nanoparticles," *The Journal of Physical Chemistry B*, vol. 108, no. 30, pp. 10955–10964, 2004.

[30] W. M. Zhang, J. Chen, A. I. Minett, G. F. Swiegers, C. O. Too, and G. G. Wallace, "Novel acnt arrays based mea structure:nano-pt loaded acnt/nafion/acnt for fuel cell applications," *Chem. Commun.*, vol. 46, no. 26, pp. 4824–4826, 2010.

[31] R. R. Adzic, "Platinum monolayer electrocatalysts: tunable activity, stability, and self-healing properties," *Electrocatalysis*, vol. 3, no. 3-4, pp. 163–169, 2012.

[32] L. Zhang, L. Y. Wang, C. M. B. Holt, B. Zahiri, Z. Li, K. Malek, T. Navessin, M. H. Eikerling, and D. Mitlin, "Highly corrosion resistant platinum-niobium oxide-carbon nanotube electrodes for the oxygen reduction in pem fuel cells," *Energy & Environmental Science*, vol. 5, no. 3, pp. 6156–6172, 2012.

[33] J. Kibsgaard, Z. Chen, B. N. Reinecke, and T. F. Jaramillo, "Engineering the surface structure of mos2 to preferentially expose active edge sites for electrocatalysis," *Nature materials*, vol. 11, no. 11, pp. 963–969, 2012.

[34] F. J. Vidal-Iglesias, R. M. Arán-Ais, J. Solla-Gullön, E. Herrero, and J. M. Feliu, "Electrochemical characterization of shape-controlled pt nanoparticles in different supporting electrolytes," *ACS Catalysis*, vol. 2, no. 5, pp. 901–910, 2012.

[35] L. Yang, M. B. Vukmirovic, D. Su, K. Sasaki, J. A. Herron, M. Mavrikakis, S. Liao, and R. R. Adzic, "Tuning the catalytic activity of ru@ pt core–shell nanoparticles for the oxygen reduction reaction by varying the shell thickness," *The Journal of Physical Chemistry C*, vol. 117, no. 4, pp. 1748–1753, 2013.

[36] R. M. Arán-Ais, F. Dionigi, T. Merzdorf, M. Gocyla, M. Heggen, R. E. Dunin-Borkowski, M. Gliech, J. Solla-Gullón, E. Herrero, J. M. Feliu, *et al.*, "Elemental anisotropic growth and atomic-scale structure of shape-controlled octahedral pt–ni–co alloy nanocatalysts," *Nano letters*, vol. 15, no. 11, pp. 7473–7480, 2015.

[37] Y. Nie, L. Li, and Z. Wei, "Recent advancements in pt and pt-free catalysts for oxygen reduction reaction," *Chemical Society Reviews*, vol. 44, no. 8, pp. 2168–2201, 2015.

[38] S. Sun, G. Zhang, N. Gauquelin, N. Chen, J. Zhou, S. Yang, W. Chen, X. Meng, D. Geng, M. N. Banis, *et al.*, "Single-atom catalysis using pt/graphene achieved through atomic layer deposition," *Scientific reports*, vol. 3, 2013.

[39] C. Chen, Y. Kang, Z. Huo, Z. Zhu, W. Huang, H. L. Xin, J. D. Snyder, D. Li, J. A. Herron, M. Mavrikakis, *et al.*, "Highly crystalline multimetallic nanoframes with three-dimensional electrocatalytic surfaces," *Science*, vol. 343, no. 6177, pp. 1339–1343, 2014.

[40] M. A. Hoque, F. M. Hassan, D. Higgins, J.-Y. Choi, M. Pritzker, S. Knights, S. Ye, and Z. Chen, "Multigrain platinum nanowires consisting of oriented nanoparticles anchored on sulfur-doped graphene as a highly active and durable oxygen reduction electrocatalyst," *Advanced Materials*, vol. 27, no. 7, pp. 1229–1234, 2015.

[41] G. N. Vayssilov, Y. Lykhach, A. Migani, T. Staudt, G. P. Petrova, N. Tsud, T. Skála, A. Bruix, F. Illas, K. C. Prince, *et al.*, "Support nanostructure boosts oxygen transfer to catalytically active platinum nanoparticles," *Nature materials*, vol. 10, no. 4, pp. 310–315, 2011.

[42] J. Seo, D. H. Anjum, K. Takanabe, J. Kubota, and K. Domen, "Electrodeposited ultrafine taox/cb catalysts for pefc cathode application: Their oxygen reduction reaction kinetics," *Electrochimica Acta*, vol. 149, pp. 76–85, 2014.

[43] N. Cheng, M. N. Banis, J. Liu, A. Riese, S. Mu, R. Li, T.-K. Sham, and X. Sun, "Atomic scale enhancement of metal–support interactions between pt and zrc for highly stable electrocatalysts," *Energy & Environmental Science*, vol. 8, no. 5, pp. 1450–1455, 2015.

[44] X. Zhou, J. Qiao, L. Yang, and J. Zhang, "A review of graphene-based nanostructural materials for both catalyst supports and metal-free catalysts in pem fuel cell oxygen reduction reactions," *Advanced Energy Materials*, vol. 4, no. 8, 2014.

[45] A. Rabis, P. Rodriguez, and T. J. Schmidt, "Electrocatalysis for polymer electrolyte fuel cells: recent achievements and future challenges," *ACS Catalysis*, vol. 2, no. 5, pp. 864–890, 2012.

[46] M. K. Debe, "Electrocatalyst approaches and challenges for automotive fuel cells," *Nature*, vol. 486, no. 7401, pp. 43–51, 2012.

[47] A. M. Gómez-Marín, R. Rizo, and J. M. Feliu, "Oxygen reduction reaction at pt single crystals: a critical overview," *Catalysis Science & Technology*, vol. 4, no. 6, pp. 1685–1698, 2014.

[48] S. G. Rinaldo, J. Stumper, and M. Eikerling, "Physical theory of platinum nanoparticle dissolution in polymer electrolyte fuel cells," *J. Phys. Chem. C*, vol. 114, no. 13, pp. 5773–5785, 2010.

[49] S. G. Rinaldo, W. Lee, J. Stumper, and M. Eikerling, "Nonmonotonic dynamics in lifshitz-slyozov-wagner theory: Ostwald ripening in nanoparticle catalysts," *PHYSICAL REVIEW E*, vol. 86, OCT 5 2012.

[50] P. P. Lopes, D. Strmcnik, D. Tripkovic, J. G. Connell, V. R. Stamenkovic, and N. M. Markovic, "Relationships between atomic level surface structure and stability/activity of platinum surface atoms in aqueous environments," *ACS Catalysis*, 2016.

[51] M. J. Eslamibidgoli, J. Huang, T. Kadyk, A. Malek, and M. H. Eikerling, "How theory and simulation can drive fuel cell electrocatalysis," *Nanoenergy*, p. doi:10.1016/j.nanoen.2016.06.004, 2016.

[52] no. U.S. DRIVE Partnership, Fuel Cell Technical Team Roadmap, 2013. http:// energy.gov/sites/prod/files/2014/02/f8/fctt_roadmap_june2013.pdf.

[53] T. Madden, D. Weiss, N. Cipollini, D. Condit, M. Gummalla, S. Burlatsky, and V. Atrazhev, "Degradation of polymer-electrolyte membranes in fuel cells i. experimental," *Journal of The Electrochemical Society*, vol. 156, no. 5, pp. B657–B662, 2009.

[54] F. De Bruijn, V. Dam, and G. Janssen, "Review: durability and degradation issues of pem fuel cell components," *Fuel cells*, vol. 8, no. 1, pp. 3–22, 2008.

[55] J. Wu, X. Z. Yuan, J. J. Martin, H. Wang, J. Zhang, J. Shen, S. Wu, and W. Merida, "A review of pem fuel cell durability: degradation mechanisms and mitigation strategies," *Journal of Power Sources*, vol. 184, no. 1, pp. 104–119, 2008.

[56] T. Jahnke, G. Futter, A. Latz, T. Malkow, G. Papakonstantinou, G. Tsotridis, P. Schott, M. Gérard, M. Quinaud, M. Quiroga, *et al.*, "Performance and degradation of proton exchange membrane fuel cells: State of the art in modeling from atomistic to system scale," *Journal of Power Sources*, vol. 304, pp. 207–233, 2016.

[57] L. Gubler, S. M. Dockheer, and W. H. Koppenol, "Radical formation and ionomer degradation in polymer electrolyte fuel cells," *Journal of The Electrochemical Society*, vol. 158, no. 7, pp. B755–B769, 2011.

[58] X. Huang, R. Solasi, Y. Zou, M. Feshler, K. Reifsnider, D. Condit, S. Burlatsky, and T. Madden, "Mechanical endurance of polymer electrolyte membrane and pem fuel cell durability," *Journal of Polymer Science Part B: Polymer Physics*, vol. 44, no. 16, pp. 2346–2357, 2006.

[59] V. O. Mittal, H. R. Kunz, and J. M. Fenton, "Membrane degradation mechanisms in pemfcs," *Journal of The Electrochemical Society*, vol. 154, no. 7, pp. B652–B656, 2007.

[60] J. Healy, C. Hayden, T. Xie, K. Olson, R. Waldo, M. Brundage, H. Gasteiger, and J. Abbott, "Aspects of the chemical degradation of pfsa ionomers used in pem fuel cells," *Fuel cells*, vol. 5, no. 2, pp. 302–308, 2005.

[61] R. Borup, J. Meyers, B. Pivovar, Y. S. Kim, R. Mukundan, N. Garland, D. Myers, M. Wilson, F. Garzon, D. Wood, *et al.*, "Scientific aspects of polymer electrolyte fuel cell durability and degradation," *Chemical reviews*, vol. 107, no. 10, pp. 3904–3951, 2007.

[62] C. Lim, L. Ghassemzadeh, F. Van Hove, M. Lauritzen, J. Kolodziej, G. Wang, S. Holdcroft, and E. Kjeang, "Membrane degradation during combined chemical and mechanical accelerated stress testing of polymer electrolyte fuel cells," *Journal of Power Sources*, vol. 257, pp. 102–110, 2014.

[63] X. Fang, P. K. Shen, S. Song, V. Stergiopoulos, and P. Tsiakaras, "Degradation of perfluorinated sulfonic acid films: An in-situ infrared spectro-electrochemical study," *Polymer Degradation and stability*, vol. 94, no. 10, pp. 1707–1713, 2009.

[64] C. Chen, G. Levitin, D. W. Hess, and T. F. Fuller, "Xps investigation of nafion® membrane degradation," *Journal of Power Sources*, vol. 169, no. 2, pp. 288–295, 2007.

[65] L. Ghassemzadeh, M. Marrony, R. Barrera, K. Kreuer, J. Maier, and K. Müller, "Chemical degradation of proton conducting perflurosulfonic acid ionomer membranes studied by solid-state nuclear magnetic resonance spectroscopy," *Journal of Power Sources*, vol. 186, no. 2, pp. 334–338, 2009.

[66] M. P. Rodgers, L. J. Bonville, H. R. Kunz, D. K. Slattery, and J. M. Fenton, "Fuel cell perfluorinated sulfonic acid membrane degradation correlating accelerated stress testing and lifetime," *Chemical reviews*, vol. 112, no. 11, pp. 6075–6103, 2012.

[67] A. C. Fernandes and E. A. Ticianelli, "A performance and degradation study of nafion 212 membrane for proton exchange membrane fuel cells," *Journal of Power Sources*, vol. 193, no. 2, pp. 547–554, 2009.

[68] M. P. Rodgers, R. P. Brooker, N. Mohajeri, L. J. Bonville, H. R. Kunz, D. K. Slattery, and J. M. Fenton, "Comparison of proton exchange membranes degradation rates between accelerated and performance tests," *Journal of The Electrochemical Society*, vol. 159, no. 7, pp. F338–F352, 2012.

[69] L. Ghassemzadeh, K. Kreuer, J. Maier, and K. Müller, "Evaluating chemical degradation of proton conducting perfluorosulfonic acid ionomers in a fenton test by solid-state 19 f nmr spectroscopy," *Journal of Power Sources*, vol. 196, no. 5, pp. 2490–2497, 2011.

[70] M. Inaba, T. Kinumoto, M. Kiriake, R. Umebayashi, A. Tasaka, and Z. Ogumi, "Gas crossover and membrane degradation in polymer electrolyte fuel cells," *Electrochimica Acta*, vol. 51, no. 26, pp. 5746–5753, 2006.

[71] S. A. Vilekar and R. Datta, "The effect of hydrogen crossover on open-circuit voltage in polymer electrolyte membrane fuel cells," *Journal of Power Sources*, vol. 195, no. 8, pp. 2241–2247, 2010.

[72] L. Ghassemzadeh and S. Holdcroft, "Quantifying the structural changes of perfluorosulfonated acid ionomer upon reaction with hydroxyl radicals," *Journal of the American Chemical Society*, vol. 135, no. 22, pp. 8181–8184, 2013.

[73] F. D. Coms, "The chemistry of fuel cell membrane chemical degradation," *ECS Transactions*, vol. 16, no. 2, pp. 235–255, 2008.

[74] W. Liu and D. Zuckerbrod, "In situ detection of hydrogen peroxide in pem fuel cells," *Journal of The Electrochemical Society*, vol. 152, no. 6, pp. A1165–A1170, 2005.

[75] L. Ghassemzadeh, K.-D. Kreuer, J. Maier, and K. Müller, "Chemical degradation of nafion membranes under mimic fuel cell conditions as investigated by solid-state nmr spectroscopy," *The Journal of Physical Chemistry C*, vol. 114, no. 34, pp. 14635–14645, 2010.

[76] M. Aoki, H. Uchida, and M. Watanabe, "Novel evaluation method for degradation rate of polymer electrolytes in fuel cells," *Electrochemistry communications*, vol. 7, no. 12, pp. 1434–1438, 2005.

[77] M. Aoki, H. Uchida, and M. Watanabe, "Decomposition mechanism of perfluorosulfonic acid electrolyte in polymer electrolyte fuel cells," *Electrochemistry communications*, vol. 8, no. 9, pp. 1509–1513, 2006.

[78] A. Ohma, S. Suga, S. Yamamoto, and K. Shinohara, "Phenomenon analysis of pefc for automotive use (1) membrane degradation behavior during ocv hold test," *ECS Transactions*, vol. 3, no. 1, pp. 519–529, 2006.

[79] D. Zhao, B. Yi, H. Zhang, and M. Liu, "The effect of platinum in a nafion membrane on the durability of the membrane under fuel cell conditions," *Journal of Power Sources*, vol. 195, no. 15, pp. 4606–4612, 2010.

[80] N. Hasegawa, T. Asano, T. Hatanaka, M. Kawasumi, and Y. Morimoto, "Degradation of perfluorinated membranes having intentionally formed pt-band," *ECS Transactions*, vol. 16, no. 2, pp. 1713–1716, 2008.

[81] S. Helmly, B. Ohnmacht, R. Hiesgen, E. Gülzow, and K. A. Friedrich, "Influence of platinum precipitation on properties and degradation of nafion® membranes," *ECS Transactions*, vol. 58, no. 1, pp. 969–990, 2013.

[82] A. Pozio, R. Silva, M. De Francesco, and L. Giorgi, "Nafion degradation in pefcs from end plate iron contamination," *Electrochimica acta*, vol. 48, no. 11, pp. 1543–1549, 2003.

[83] P. Ferreira, Y. Shao-Horn, D. Morgan, R. Makharia, S. Kocha, H. Gasteiger, *et al.*, "Instability of pt/ c electrocatalysts in proton exchange membrane fuel cells: A mechanistic investigation," *J. Electrochem. Soc.*, vol. 152, no. 11, pp. A2256–A2271, (2005).

[84] N. Macauley, K. H. Wong, M. Watson, and E. Kjeang, "Favorable effect of in-situ generated platinum in the membrane on fuel cell membrane durability," *Journal of Power Sources*, vol. 299, pp. 139–148, 2015.

[85] M. P. Rodgers, B. P. Pearman, L. J. Bonville, D. A. Cullen, N. Mohajeri, and D. K. Slattery, "Evaluation of the effect of impregnated platinum on pfsa degradation for pem fuel cells," *Journal of The Electrochemical Society*, vol. 160, no. 10, pp. F1123–F1128, 2013.

[86] A. Ohma, S. Yamamoto, and K. Shinohara, "Analysis of membrane degradation behavior during ocv hold test," *ECS Transactions*, vol. 11, no. 1, pp. 1181–1192, 2007.

[87] S. Kundu, M. Cimenti, S. Lee, and D. Bessarabov, "Fingerprint of automotive fuel cell cathode catalyst degradation: Pt band in pems," *Membrane Technology*, vol. 2009, no. 10, pp. 7–10, 2009.

[88] A. Ohma, S. Yamamoto, and K. Shinohara, "Membrane degradation mechanism during open-circuit voltage hold test," *Journal of Power Sources*, vol. 182, no. 1, pp. 39–47, 2008.

[89] W. Bi, G. E. Gray, and T. F. Fuller, "Pem fuel cell pt/ c dissolution and deposition in nafion electrolyte," *Electrochemical and Solid-State Letters*, vol. 10, no. 5, pp. B101–B104, 2007.

[90] N. Ohguri, A. Y. Nosaka, and Y. Nosaka, "Detection of oh radicals as the effect of pt particles in the membrane of polymer electrolyte fuel cells," *Journal of Power Sources*, vol. 195, no. 15, pp. 4647–4652, 2010.

[91] N. Macauley, L. Ghassemzadeh, C. Lim, M. Watson, J. Kolodziej, M. Lauritzen, S. Holdcroft, and E. Kjeang, "Pt band formation enhances the stability of fuel cell membranes," *ECS Electrochemistry Letters*, vol. 2, no. 4, pp. F33–F35, 2013.

[92] H. Hagihara, H. Uchida, and M. Watanabe, "Preparation of highly dispersed sio< sub> 2</sub> and pt particles in nafion< sup>®</sup> 112 for self-humidifying electrolyte membranes in fuel cells," *Electrochimica Acta*, vol. 51, no. 19, pp. 3979–3985, 2006.

[93] M. J. Eslamibidgoli, P.-É. A. Melchy, and M. H. Eikerling, "Modeling the local potential at pt nanoparticles in polymer electrolyte membranes," *Physical Chemistry Chemical Physics*, vol. 17, no. 15, pp. 9802–9811, 2015.

[94] M. J. Eslamibidgoli and M. H. Eikerling, "Electrochemical formation of reactive oxygen species at pt (111)– a density functional theory study," *ACS Catalysis*, vol. 5, no. 10, pp. 6090–6098, 2015.

[95] S. Helmly, M. J. Eslamibidgoli, A. Friedrich, and M. H. Eikerling, "Impact of electrochemical conditions around pt deposits in polymer electrolyte membranes on ionomer decomposition âĂŞ an experimental study," *Electrochimica Acta*, vol. Submitted, 2016.

[96] D. Rand and R. Woods, "A study of the dissolution of platinum, palladium, rhodium and gold electrodes in 1 m sulphuric acid by cyclic voltammetry," *Journal of Electroanalytical Chemistry and Interfacial Electrochemistry*, vol. 35, no. 1, pp. 209–218, 1972.

[97] H. Angerstein-Kozlowska, B. Conway, and W. Sharp, "The real condition of electrochemically oxidized platinum surfaces: Part i. resolution of component processes," *Journal of Electroanalytical Chemistry and Interfacial Electrochemistry*, vol. 43, no. 1, pp. 9–36, 1973.

[98] B. E. Conway, "Electrochemical oxide film formation at noble metals as a surface-chemical process," *Progress in surface science*, vol. 49, no. 4, pp. 331–452, 1995.

[99] S. Cherevko, N. Kulyk, and K. J. Mayrhofer, "Durability of platinum-based fuel cell electrocatalysts: Dissolution of bulk and nanoscale platinum," *Nano Energy*, 2016.

[100] H. You, D. Zurawski, Z. Nagy, and R. Yonco, "In-situ x-ray reflectivity study of incipient oxidation of pt (111) surface in electrolyte solutions," *The Journal of chemical physics*, vol. 100, no. 6, pp. 4699–4702, 1994.

[101] G. Jerkiewicz, G. Vatankhah, J. Lessard, M. P. Soriaga, and Y.-S. Park, "Surface-oxide growth at platinum electrodes in aqueous h 2 so 4: Reexamination of its mechanism through combined cyclic-voltammetry, electrochemical quartz-crystal nanobalance, and auger electron spectroscopy measurements," *Electrochimica Acta*, vol. 49, no. 9, pp. 1451–1459, 2004.

[102] S. P. Devarajan, J. A. Hinojosa, and J. F. Weaver, "Stm study of high-coverage structures of atomic oxygen on pt (111): p (2$\times$ 1) and pt oxide chain structures," *Surface Science*, vol. 602, no. 19, pp. 3116–3124, 2008.

[103] B. Conway, B. Barnett, H. Angerstein-Kozlowska, and B. Tilak, "A surface-electrochemical basis for the direct logarithmic growth law for initial stages of extension of anodic oxide films formed at noble metals," *The Journal of chemical physics*, vol. 93, no. 11, pp. 8361–8373, 1990.

[104] Z. Gu and P. B. Balbuena, "Chemical environment effects on the atomic oxygen absorption into pt (111) subsurfaces," *The Journal of Physical Chemistry C*, vol. 111, no. 46, pp. 17388–17396, 2007.

[105] J. M. Hawkins, J. F. Weaver, and A. Asthagiri, "Density functional theory study of the initial oxidation of the pt (111) surface," *Physical Review B*, vol. 79, no. 12, p. 125434, 2009.

[106] E. F. Holby, J. Greeley, and D. Morgan, "Thermodynamics and hysteresis of oxide formation and removal on platinum (111) surfaces," *The Journal of Physical Chemistry C*, vol. 116, no. 18, pp. 9942–9946, 2012.

[107] D. Fantauzzi, J. E. Mueller, L. Sabo, A. C. van Duin, and T. Jacob, "Surface buckling and subsurface oxygen: Atomistic insights into the surface oxidation of pt (111)," *ChemPhysChem*, vol. 16, no. 13, pp. 2797–2802, 2015.

[108] M. J. Eslamibidgoli and M. H. Eikerling, "Atomistic mechanism of pt extraction at oxidized surfaces: Insights from dft," *Electrocatalysis*, vol. 7, p. 345, 2016.

[109] E. G. Lewars, *Computational chemistry: introduction to the theory and applications of molecular and quantum mechanics*. Springer Science & Business Media, 2010.

[110] W. J. Hehre, *Ab initio molecular orbital theory*. Wiley-Interscience, 1986.

[111] M. Born and R. Oppenheimer, "Zur quantentheorie der molekeln," *Annalen der Physik*, vol. 389, no. 20, pp. 457–484, 1927.

[112] J. C. Slater, "A simplification of the hartree-fock method," *Physical Review*, vol. 81, no. 3, p. 385, 1951.

[113] J. A. Pople and D. L. Beveridge, *Approximate molecular orbital theory*, vol. 30. McGraw-Hill New York, 1970.

[114] I. N. Levine, *Quantum chemistry*, vol. 6. Pearson Prentice Hall Upper Saddle River, NJ, 2009.

[115] A. K. Rappé and C. J. Casewit, *Molecular mechanics across chemistry*. University Science Books, 1997.

[116] C. C. J. Roothaan, "New developments in molecular orbital theory," *Reviews of modern physics*, vol. 23, no. 2, p. 69, 1951.

[117] C. Pisani, *Quantum-mechanical ab-initio calculation of the properties of crystalline materials*, vol. 67. Springer Science & Business Media, 2012.

[118] R. F. Bader, *Atoms in molecules*. Wiley Online Library, 1990.

[119] A. Szabo and N. S. Ostlund, *Modern quantum chemistry: introduction to advanced electronic structure theory*. Courier Corporation, 1989.

[120] W. Kohn and L. J. Sham, "Self-consistent equations including exchange and correlation effects," *Physical review*, vol. 140, no. 4A, p. A1133, 1965.

[121] S. Vosko, L. Wilk, and M. Nusair, "Accurate spin-dependent electron liquid correlation energies for local spin density calculations: a critical analysis," *Canadian Journal of physics*, vol. 58, no. 8, pp. 1200–1211, 1980.

[122] P. Stephens, F. Devlin, C. Chabalowski, and M. J. Frisch, "Ab initio calculation of vibrational absorption and circular dichroism spectra using density functional force fields," *The Journal of Physical Chemistry*, vol. 98, no. 45, pp. 11623–11627, 1994.

[123] S. Grimme, J. Antony, S. Ehrlich, and H. Krieg, "A consistent and accurate ab initio parametrization of density functional dispersion correction (dft-d) for the 94 elements h-pu," *The Journal of chemical physics*, vol. 132, no. 15, p. 154104, 2010.

[124] S. Grimme, S. Ehrlich, and L. Goerigk, "Effect of the damping function in dispersion corrected density functional theory," *Journal of computational chemistry*, vol. 32, no. 7, pp. 1456–1465, 2011.

[125] K. Tonigold and A. Groß, "Dispersive interactions in water bilayers at metallic surfaces: A comparison of the pbe and rpbe functional including semiempirical dispersion corrections," *Journal of computational chemistry*, vol. 33, no. 6, pp. 695–701, 2012.

[126] K. Forster-Tonigold and A. Groß, "Dispersion corrected rpbe studies of liquid water," *The Journal of chemical physics*, vol. 141, no. 6, p. 064501, 2014.

[127] G. Kresse and J. Furthmüller, "Efficient iterative schemes for ab initio total-energy calculations using a plane-wave basis set," *Physical Review B*, vol. 54, no. 16, p. 11169, 1996.

[128] N. W. Ashcroft and N. D. Mermin, "Solid state physics (holt, rinehart and winston, new york, 1976)," *There is no corresponding record for this reference*, pp. 490–495, 2005.

[129] J. D. Pack and H. J. Monkhorst, """ special points for brillouin-zone integrations"âĂŤa reply," *Physical Review B*, vol. 16, no. 4, p. 1748, 1977.

[130] J. P. Perdew, K. Burke, and M. Ernzerhof, "Generalized gradient approximation made simple," *Physical review letters*, vol. 77, no. 18, p. 3865, 1996.

[131] S. Schnur and A. Groß, "Properties of metal–water interfaces studied from first principles," *New Journal of Physics*, vol. 11, no. 12, p. 125003, 2009.

[132] T. Roman and A. Groß, "Structure of water layers on hydrogen-covered pt electrodes," *Catalysis today*, vol. 202, pp. 183–190, 2013.

[133] V. Berejnov, Z. Martin, M. West, S. Kundu, D. Bessarabov, J. Stumper, D. Susac, and A. P. Hitchcock, "Probing platinum degradation in polymer electrolyte membrane fuel cells by synchrotron x-ray microscopy," *Physical Chemistry Chemical Physics*, vol. 14, no. 14, pp. 4835–4843, 2012.

[134] T. Akita, A. Taniguchi, J. Maekawa, Z. Siroma, K. Tanaka, M. Kohyama, and K. Yasuda, "Analytical tem study of pt particle deposition in the proton-exchange membrane of a membrane-electrode-assembly," *Journal of power sources*, vol. 159, no. 1, pp. 461–467, 2006.

[135] K. Yasuda, A. Taniguchi, T. Akita, T. Ioroi, and Z. Siroma, "Platinum dissolution and deposition in the polymer electrolyte membrane of a pem fuel cell as studied by potential cycling," *Physical Chemistry Chemical Physics*, vol. 8, no. 6, pp. 746–752, 2006.

[136] L. Kim, C. G. Chung, Y. W. Sung, and J. S. Chung, "Dissolution and migration of platinum after long-term operation of a polymer electrolyte fuel cell under various conditions," *Journal of Power Sources*, vol. 183, no. 2, pp. 524–532, 2008.

[137] G. Diloyan, M. Sobel, K. Das, and P. Hutapea, "Effect of mechanical vibration on platinum particle agglomeration and growth in polymer electrolyte membrane fuel cell catalyst layers," *Journal of Power Sources*, vol. 214, pp. 59–67, 2012.

[138] M. Ohishi, Y. Okano, Y. Ono, A. Ohma, K. Fushinobu, and K. Okazaki, "Investigation of potential profile in electrolyte membrane of pefc by using microprobe technique," *International Journal of Heat and Mass Transfer*, vol. 55, no. 23, pp. 7213–7217, 2012.

[139] S. Takaichi, H. Uchida, and M. Watanabe, "Distribution profile of hydrogen and oxygen permeating in polymer electrolyte membrane measured by mixed potential," *Electrochemistry communications*, vol. 9, no. 8, pp. 1975–1979, 2007.

[140] V. Atrazhev, N. Erikhman, and S. Burlatsky, "The potential of catalytic particle in ion exchange membrane," *Journal of Electroanalytical Chemistry*, vol. 601, no. 1, pp. 251–259, 2007.

[141] W. Sheng, H. A. Gasteiger, and Y. Shao-Horn, "Hydrogen oxidation and evolution reaction kinetics on platinum: acid vs alkaline electrolytes," *Journal of The Electrochemical Society*, vol. 157, no. 11, pp. B1529–B1536, 2010.

[142] D. Sepa, M. Vojnovic, and A. Damjanovic, "Reaction intermediates as a controlling factor in the kinetics and mechanism of oxygen reduction at platinum electrodes," *Electrochimica Acta*, vol. 26, no. 6, pp. 781–793, 1981.

[143] P. D. Beattie, V. I. Basura, and S. Holdcroft, "Temperature and pressure dependence of o< sub> 2</sub> reduction at ptâĹč nafion® 117 and ptâĹč bam® 407 interfaces," *Journal of Electroanalytical Chemistry*, vol. 468, no. 2, pp. 180–192, 1999.

[144] A. J. Bard and L. R. Faulkner, "Electrochemical methods: fundamentals and applications, 2nd," *Hoboken: Wiley and Sons*, 2001.

[145] H. Ju, C.-Y. Wang, S. Cleghorn, and U. Beuscher, "Nonisothermal modeling of polymer electrolyte fuel cells i. experimental validation," *Journal of The Electrochemical Society*, vol. 152, no. 8, pp. A1645–A1653, 2005.

[146] M. M. Mench, *FUEL CELL engines*. John Wiley & Sons, 2008.

[147] E. L. Cussler, *Diffusion: mass transfer in fluid systems*. Cambridge university press, 2009.

[148] P. Gode, G. Lindbergh, and G. Sundholm, "In-situ measurements of gas permeability in fuel cell membranes using a cylindrical microelectrode," *Journal of Electroanalytical Chemistry*, vol. 518, no. 2, pp. 115–122, 2002.

[149] K. Neyerlin, W. Gu, J. Jorne, and H. A. Gasteiger, "Study of the exchange current density for the hydrogen oxidation and evolution reactions," *Journal of the Electrochemical Society*, vol. 154, no. 7, pp. B631–B635, 2007.

[150] J. H. Park, H. Zhou, S. J. Percival, B. Zhang, F.-R. F. Fan, and A. J. Bard, "Open circuit (mixed) potential changes upon contact between different inert electrodes–size and kinetic effects," *Analytical chemistry*, vol. 85, no. 2, pp. 964–970, 2013.

[151] T. Biegler, D. Rand, and R. Woods, "Limiting oxygen coverage on platinized platinum; relevance to determination of real platinum area by hydrogen adsorption," *Journal of Electroanalytical Chemistry and Interfacial Electrochemistry*, vol. 29, no. 2, pp. 269–277, 1971.

[152] G. Jerkiewicz, "Hydrogen sorption atin electrodes," *Progress in Surface Science*, vol. 57, no. 2, pp. 137–186, 1998.

[153] G. Jerkiewicz and A. Zolfaghari, "Comparison of hydrogen electroadsorption from the electrolyte with hydrogen adsorption from the gas phase," *Journal of The Electrochemical Society*, vol. 143, no. 4, pp. 1240–1248, 1996.

[154] N. M. Markovic, H. A. Gasteiger, and P. N. Ross Jr, "Oxygen reduction on platinum low-index single-crystal surfaces in sulfuric acid solution: rotating ring-pt (hkl) disk studies," *The Journal of Physical Chemistry*, vol. 99, no. 11, pp. 3411–3415, 1995.

[155] V. Stamenkovic, N. Markovic, and P. N. Ross, "Structure-relationships in electrocatalysis: oxygen reduction and hydrogen oxidation reactions on pt (111) and pt (100) in solutions containing chloride ions," *Journal of Electroanalytical Chemistry*, vol. 500, no. 1, pp. 44–51, 2001.

[156] T. Schmidt, P. Ross, and N. Markovic, "Temperature dependent surface electrochemistry on pt single crystals in alkaline electrolytes: Part 2. the hydrogen evolution/oxidation reaction," *Journal of Electroanalytical Chemistry*, vol. 524, pp. 252–260, 2002.

[157] A. Panchenko, M. Koper, T. Shubina, S. Mitchell, and E. Roduner, "Ab initio calculations of intermediates of oxygen reduction on low-index platinum surfaces," *Journal of the Electrochemical Society*, vol. 151, no. 12, pp. A2016–A2027, 2004.

[158] J. A. Keith and T. Jacob, "Theoretical studies of potential-dependent and competing mechanisms of the electrocatalytic oxygen reduction reaction on pt (111)," *Angewandte Chemie International Edition*, vol. 49, no. 49, pp. 9521–9525, 2010.

[159] M. Markiewicz, C. Zalitis, and A. Kucernak, "Performance measurements and modelling of the orr on fuel cell electrocatalysts–the modified double trap model," *Electrochimica Acta*, vol. 179, pp. 126–136, 2015.

[160] N. Marković and P. N. Ross, "Surface science studies of model fuel cell electrocatalysts," *Surface Science Reports*, vol. 45, no. 4, pp. 117–229, 2002.

[161] M. Wakisaka, H. Suzuki, S. Mitsui, H. Uchida, and M. Watanabe, "Identification and quantification of oxygen species adsorbed on pt (111) single-crystal and polycrystalline pt electrodes by photoelectron spectroscopy," *Langmuir*, vol. 25, no. 4, pp. 1897–1900, 2009.

[162] J. Rossmeisl, J. K. Nørskov, C. D. Taylor, M. J. Janik, and M. Neurock, "Calculated phase diagrams for the electrochemical oxidation and reduction of water over pt (111)," *The Journal of Physical Chemistry B*, vol. 110, no. 43, pp. 21833–21839, 2006.

[163] S. Schnur and A. Groß, "Challenges in the first-principles description of reactions in electrocatalysis," *Catalysis today*, vol. 165, no. 1, pp. 129–137, 2011.

[164] E. Skulason, G. Karlberg, J. Rossmeisl, T. Bligaard, J. P. Greeley, H. Jonsson, and J. K. Norskov, "Density functional theory calculations for the hydrogen evolution reaction in an electrochemical double layer on the pt(111) electrode," *Abstracts of Papers of the American Chemical Society*, vol. 233, 2007.

[165] H. A. Hansen, J. Rossmeisl, and J. K. Nørskov, "Surface pourbaix diagrams and oxygen reduction activity of pt, ag and ni (111) surfaces studied by dft," *Physical Chemistry Chemical Physics*, vol. 10, no. 25, pp. 3722–3730, 2008.

[166] A. S. Bondarenko, I. E. Stephens, H. A. Hansen, F. J. Pérez-Alonso, V. Tripkovic, T. P. Johansson, J. Rossmeisl, J. K. Nørskov, and I. Chorkendorff, "The pt (111)/electrolyte interface under oxygen reduction reaction conditions: an electrochemical impedance spectroscopy study," *Langmuir*, vol. 27, no. 5, pp. 2058–2066, 2011.

[167] F. Calle-Vallejo and M. T. Koper, "First-principles computational electrochemistry: Achievements and challenges," *Electrochimica Acta*, vol. 84, pp. 3–11, 2012.

[168] T. Jacob, "The mechanism of forming h2o from h2 and o2 over a pt catalyst via direct oxygen reduction," *Fuel Cells*, vol. 6, no. 3-4, pp. 159–181, 2006.

[169] T. H. Yu, Y. Sha, W.-G. Liu, B. V. Merinov, P. Shirvanian, and W. A. Goddard III, "Mechanism for degradation of nafion in pem fuel cells from quantum mechanics calculations," *Journal of the American Chemical Society*, vol. 133, no. 49, pp. 19857–19863, 2011.

[170] P. A. Thiel and T. E. Madey, "The interaction of water with solid surfaces: fundamental aspects," *Surface Science Reports*, vol. 7, no. 6-8, pp. 211–385, 1987.

[171] M. A. Henderson, "The interaction of water with solid surfaces: fundamental aspects revisited," *Surface Science Reports*, vol. 46, no. 1, pp. 1–308, 2002.

[172] J. Rossmeisl, E. Skulason, M. E. Bjorketun, V. Tripkovic, and J. K. Norskov, "Modeling the electrified solid-liquid interface," *Chemical Physics Letters*, vol. 466, no. 1-3, pp. 68–71, 2008.

[173] J. Neugebauer and M. Scheffler, "Adsorbate-substrate and adsorbate-adsorbate interactions of na and k adlayers on al (111)," *Physical Review B*, vol. 46, no. 24, p. 16067, 1992.

[174] A. Glebov, A. Graham, A. Menzel, and J. Toennies, "Orientational ordering of two-dimensional ice on pt (111)," *The Journal of chemical physics*, vol. 106, no. 22, pp. 9382–9385, 1997.

[175] P. J. Feibelman, N. C. Bartelt, S. Nie, and K. Thu¨ rmer, "Interpretation of high-resolution images of the best-bound wetting layers on pt (111)," *Journal of Chemical Physics*, vol. 133, no. 15, p. 154703, 2010.

[176] S. Nie, P. J. Feibelman, N. Bartelt, and K. Thürmer, "Pentagons and heptagons in the first water layer on pt (111)," *Physical review letters*, vol. 105, no. 2, p. 026102, 2010.

[177] D. L. Doering and T. E. Madey, "The adsorption of water on clean and oxygen-dosed ru (011)," *Surface Science*, vol. 123, no. 2, pp. 305–337, 1982.

[178] H. Ogasawara, B. Brena, D. Nordlund, M. Nyberg, A. Pelmenschikov, L. Pettersson, and A. Nilsson, "Structure and bonding of water on pt (111)," *Physical review letters*, vol. 89, no. 27, p. 276102, 2002.

[179] J.-S. Filhol and M.-L. Doublet, "An ab initio study of surface electrochemical disproportionation: the case of a water monolayer adsorbed on a pd (111) surface," *Catalysis Today*, vol. 202, pp. 87–97, 2013.

[180] H. S. Casalongue, S. Kaya, V. Viswanathan, D. J. Miller, D. Friebel, H. A. Hansen, J. K. Nørskov, A. Nilsson, and H. Ogasawara, "Direct observation of the oxygenated species during oxygen reduction on a platinum fuel cell cathode," *Nature communications*, vol. 4, 2013.

[181] I. Katsounaros, W. B. Schneider, J. C. Meier, U. Benedikt, P. U. Biedermann, A. A. Auer, and K. J. Mayrhofer, "Hydrogen peroxide electrochemistry on platinum: towards understanding the oxygen reduction reaction mechanism," *Physical Chemistry Chemical Physics*, vol. 14, no. 20, pp. 7384–7391, 2012.

[182] A. Damjanovic and V. Brusic, "Electrode kinetics of oxygen reduction on oxide-free platinum electrodes," *Electrochimica Acta*, vol. 12, no. 6, pp. 615–628, 1967.

[183] J. K. Nørskov, J. Rossmeisl, A. Logadottir, L. Lindqvist, J. R. Kitchin, T. Bligaard, and H. Jonsson, "Origin of the overpotential for oxygen reduction at a fuel-cell cathode," *The Journal of Physical Chemistry B*, vol. 108, no. 46, pp. 17886–17892, 2004.

[184] G. Karlberg, T. Jaramillo, E. Skulason, J. Rossmeisl, T. Bligaard, and J. K. Nørskov, "Cyclic voltammograms for h on pt (111) and pt (100) from first principles," *Physical review letters*, vol. 99, no. 12, p. 126101, 2007.

[185] J. A. Keith, G. Jerkiewicz, and T. Jacob, "Theoretical investigations of the oxygen reduction reaction on pt (111)," *ChemPhysChem*, vol. 11, no. 13, pp. 2779–2794, 2010.

[186] V. Tripković, E. Skúlason, S. Siahrostami, J. K. Nørskov, and J. Rossmeisl, "The oxygen reduction reaction mechanism on pt (111) from density functional theory calculations," *Electrochimica Acta*, vol. 55, no. 27, pp. 7975–7981, 2010.

[187] B. Hammer and J. K. Nørskov, "Theoretical surface science and catalysis: calculations and concepts," *Advances in catalysis*, vol. 45, pp. 71–129, 2000.

[188] H. A. Hansen, I. C. Man, F. Studt, F. Abild-Pedersen, T. Bligaard, and J. Rossmeisl, "Electrochemical chlorine evolution at rutile oxide (110) surfaces," *Physical Chemistry Chemical Physics*, vol. 12, no. 1, pp. 283–290, 2010.

[189] F. Gossenberger, T. Roman, and A. Groß, "Equilibrium coverage of halides on metal electrodes," *Surface Science*, vol. 631, pp. 17–22, 2015.

[190] A. B. Anderson and T. V. Albu, "Catalytic effect of platinum on oxygen reduction an ab initio model including electrode potential dependence," *Journal of the Electrochemical Society*, vol. 147, no. 11, pp. 4229–4238, 2000.

[191] R. A. Sidik and A. B. Anderson, "Density functional theory study of o 2 electroreduction when bonded to a pt dual site," *Journal of Electroanalytical Chemistry*, vol. 528, no. 1, pp. 69–76, 2002.

[192] J. P. Hoare, *The Electrochemistry of Oxygen*. Interscience Publishers: London, 1968.

[193] N. Markovic, H. Gasteiger, and P. N. Ross, "Kinetics of oxygen reduction on pt (hkl) electrodes: implications for the crystallite size effect with supported pt electrocatalysts," *Journal of the Electrochemical Society*, vol. 144, no. 5, pp. 1591–1597, 1997.

[194] A. M. Gómez-Marín and J. M. Feliu, "Pt (111) surface disorder kinetics in perchloric acid solutions and the influence of specific anion adsorption," *Electrochimica Acta*, vol. 82, pp. 558–569, 2012.

[195] A. Kuzume, E. Herrero, and J. M. Feliu, "Oxygen reduction on stepped platinum surfaces in acidic media," *Journal of Electroanalytical Chemistry*, vol. 599, no. 2, pp. 333–343, 2007.

[196] G. Jerkiewicz, G. Vatankhah, S.-i. Tanaka, and J. Lessard, "Discovery of the potential of minimum mass for platinum electrodes," *Langmuir*, vol. 27, no. 7, pp. 4220–4226, 2011.

[197] S. Meng, E. Wang, and S. Gao, "A molecular picture of hydrophilic and hydrophobic interactions from ab initio density functional theory calculations," *The Journal of chemical physics*, vol. 119, no. 15, pp. 7617–7620, 2003.

[198] G. Henkelman, A. Arnaldsson, and H. Jónsson, "A fast and robust algorithm for bader decomposition of charge density," *Computational Materials Science*, vol. 36, no. 3, pp. 354–360, 2006.

[199] T. Hamasaki, T. Kashiwagi, T. Imada, N. Nakamichi, S. Aramaki, K. Toh, S. Morisawa, H. Shimakoshi, Y. Hisaeda, and S. Shirahata, "Kinetic analysis of superoxide anion radical-scavenging and hydroxyl radical-scavenging activities of platinum nanoparticles," *Langmuir*, vol. 24, no. 14, pp. 7354–7364, 2008.

[200] A. Kortan and R. L. Park, "Phase diagram of oxygen chemisorbed on nickel (111)," *Physical Review B*, vol. 23, no. 12, p. 6340, 1981.

[201] F. Leisenberger, G. Koller, M. Sock, S. Surnev, M. Ramsey, F. Netzer, B. Klötzer, and K. Hayek, "Surface and subsurface oxygen on pd (111)," *Surface science*, vol. 445, no. 2, pp. 380–393, 2000.

[202] Y. He, M. Knapp, E. Lundgren, and H. Over, "Ru (0001) model catalyst under oxidizing and reducing reaction conditions: in-situ high-pressure surface x-ray diffraction study," *The Journal of Physical Chemistry B*, vol. 109, no. 46, pp. 21825–21830, 2005.

[203] A. A. Topalov, I. Katsounaros, M. Auinger, S. Cherevko, J. C. Meier, S. O. Klemm, and K. J. J. Mayrhofer, "Dissolution of platinum: Limits for the deployment of electrochemical energy conversion?," *ANGEWANDTE CHEMIE-INTERNATIONAL EDITION*, vol. 51, no. 50, pp. 12613–12615, 2012.

[204] Y. Furuya, T. Mashio, A. Ohma, M. Tian, F. Kaveh, D. Beauchemin, and G. Jerkiewicz, "Influence of electrolyte composition and ph on platinum electrochemical and/or chemical dissolution in aqueous acidic media," *ACS Catalysis*, vol. 5, no. 4, pp. 2605–2614, 2015.

[205] Y. Kang, J. Snyder, M. Chi, D. Li, K. L. More, N. M. Markovic, and V. R. Stamenkovic, "Multimetallic core/interlayer/shell nanostructures as advanced electrocatalysts," *Nano letters*, vol. 14, no. 11, pp. 6361–6367, 2014.

[206] Y. Furuya, T. Mashio, A. Ohma, N. Dale, K. Oshihara, and G. Jerkiewicz, "Surface oxide growth on platinum electrode in aqueous trifluoromethanesulfonic acid," *The Journal of chemical physics*, vol. 141, no. 16, p. 164705, 2014.

[207] L. Xing, M. A. Hossain, M. Tian, D. Beauchemin, K. T. Adjemian, and G. Jerkiewicz, "Platinum electro-dissolution in acidic media upon potential cycling," *Electrocatalysis*, vol. 5, no. 1, pp. 96–112, 2014.

[208] S. G. Rinaldo, P. Urchaga, J. Hu, W. Lee, J. Stumper, C. Rice, and M. Eikerling, "Theoretical analysis of electrochemical surface-area loss in supported nanoparticle catalysts," *Physical Chemistry Chemical Physics*, vol. 16, no. 48, pp. 26876–26886, 2014.

[209] M. Wakisaka, S. Asizawa, H. Uchida, and M. Watanabe, "In situ stm observation of morphological changes of the pt (111) electrode surface during potential cycling in 10 mm hf solution," *Physical Chemistry Chemical Physics*, vol. 12, no. 16, pp. 4184–4190, 2010.

[210] A. Sun, J. Franc, and D. D. Macdonald, "Growth and properties of oxide films on platinum i. eis and x-ray photoelectron spectroscopy studies," *Journal of the Electrochemical Society*, vol. 153, no. 7, pp. B260–B277, 2006.

[211] K. Sasaki, N. Marinkovic, H. S. Isaacs, and R. R. Adzic, "Synchrotron-based in situ characterization of carbon-supported platinum and platinum monolayer electrocatalysts," *ACS Catalysis*, vol. 6, no. 1, pp. 69–76, 2015.

[212] P. Balbuena, R. Callejas-Tovar, P. d. Hirunsit, J. M. De La Hoz, Y. Ma, and G. Ramirez-Caballero, "Evolution of pt and pt-alloy catalytic surfaces under oxygen reduction reaction in acid medium," *Topics in Catalysis*, vol. 55, no. 5-6, pp. 322–335, 2012.

[213] A. Michaelides and P. Hu, "Insight into microscopic reaction pathways in heterogeneous catalysis," *Journal of the American Chemical Society*, vol. 122, no. 40, pp. 9866–9867, 2000.

[214] A. Michaelides, P. Hu, and A. Alavi, "Physical origin of the high reactivity of subsurface hydrogen in catalytic hydrogenation," *The Journal of chemical physics*, vol. 111, no. 4, pp. 1343–1345, 1999.

[215] Z.-P. Liu and P. Hu, "General rules for predicting where a catalytic reaction should occur on metal surfaces: A density functional theory study of ch and co bond breaking/making on flat, stepped, and kinked metal surfaces," *Journal of the American Chemical Society*, vol. 125, no. 7, pp. 1958–1967, 2003.

[216] L. Li, F. Abild-Pedersen, J. Greeley, and J. K. Nørskov, "Surface tension effects on the reactivity of metal nanoparticles," *The Journal of Physical Chemistry Letters*, vol. 6, no. 19, pp. 3797–3801, 2015.

[217] B. Hammer and J. Nørskov, "Electronic factors determining the reactivity of metal surfaces," *Surface Science*, vol. 343, no. 3, pp. 211–220, 1995.

[218] A. Eichler, F. Mittendorfer, and J. Hafner, "Precursor-mediated adsorption of oxygen on the (111) surfaces of platinum-group metals," *Physical Review B*, vol. 62, no. 7, p. 4744, 2000.

[219] J. Tymoczko, F. Calle-Vallejo, V. Čolić, W. Schuhmann, and A. S. Bandarenka, "Evaluation of the electrochemical stability of model cu-pt (111) near-surface alloy catalysts," *Electrochimica Acta*, vol. 179, pp. 469–474, 2015.

Appendix A

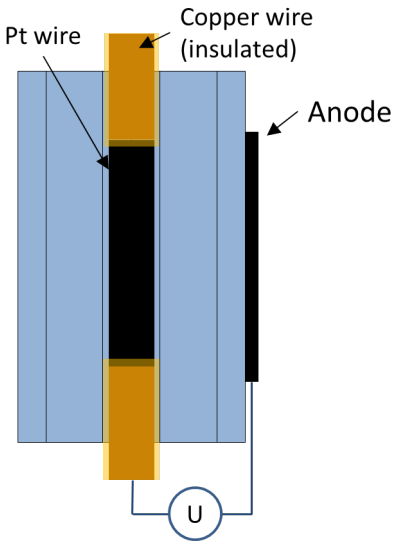

Figure A.1: Cell configuration of Pt micro-electrode placed in a multi-membrane unit

In the first experiment, the electrical potential of PITM was investigated via a Pt microelectrode which was inserted into the electrolyte membrane. This method was also used in other studies to examine the potential distribution within the electrolyte membrane[74,138,139].

As Pt microelectrode, a Pt wire with a diameter of 40 μm was used. For sensing the Pt potential, each end of the Pt wire was soldered to an isolated copper wire which protruded from the electrolyte. This contact redundancy not only yielded a back-up contact for potential sensing but allowed also checking for contact problems such as breaking of the mechanically weak Pt wire. To achieve a sufficient spatial resolution for potential sensing, it was necessary to increase the ratio between the electrolyte thickness and diameter of the Pt wire. Therefore, the electrolyte membrane thickness was increased by stacking several single membranes to a series connection of membranes, hereafter referred to as a multi-membrane-unit (MMU), with a nominal thickness of 200 μm. The configuration of this cell is shown in Fig. A.1.

As membranes, the chemically stabilized membrane types Nafion® NRE-211CS (25 μm thick, DuPont) and NRE-212CS (50 μm thick, DuPont) were used in sheets with a size

of 65 x 65 mm. The Pt microelectrode was inserted in the middle of the MMU between two membranes. The membrane on the hydrogen side was provided with an electrode which served as both, counter and reversible hydrogen electrode. For this, the membrane was coated beforehand with a catalyst layer at an area of 25 cm^2 by dry-spraying and hot-pressed with a supporting gas diffusion layer (Sigracet GDL 25 BC, SGL Technologies GmbH) for 5 min at 160°C with 700 N cm^{-2}.

The catalyst layer consisted of Pt black (Hispec 1000, Johnson Matthey Fuel Cells) and 30 wt Nafion® ionomer powder. The ionomer powder used in the dry spraying technique is produced by freeze milling Nafion® resin NR-50 (DuPont). The Pt loading was 0.3 mgPt cm^{-2}. Lastly, the MMU with the microelectrode was hot-pressed for 5 min at 180 °C with 700 N cm^{-2}. For operating this cell, it was equipped with an additional gas diffusion layer (Sigracet SGL-BC25) on the oxygen side and gaskets (Freudenberg FC-PO, 350 μm thick) on both sides and sandwiched between two cell holders which were bolted together with a tightening torque of 3 Nm. The flow field in the cell holders had a single serpentine channel. Both cell holders were arranged in co-flow configuration.

The cell was operated in a test station at 80°C. For gas humidification, humidifiers were used which allowed the control of the humidity level by adjusting the dew point temperature. The dew point temperature was set to 76 °C. H_2 and O_2/air were fed to the cell, each with a flow rate of 100 sccm. The concentration of H_2 and O_2 at the Pt microelectrode was varied by controlling the reactant pressure at the inlet of the cell holder. The electrical potential of the Pt-microelectrode vs. RHE was measured with the potentiostat IM6 (Zahner elektrik).

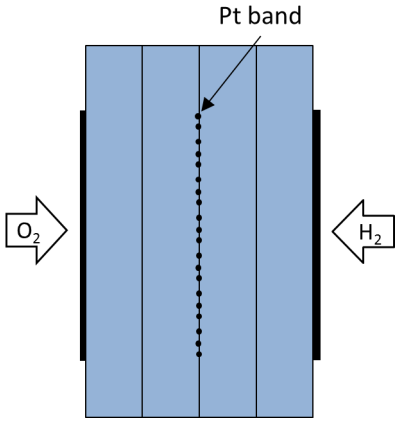

Figure A.2: Cell configuration for membrane degradation tests

The degradation experiment was performed with four cells containing a MMU but differing regarding the presence of PITM and catalyst layers. The four configurations were: MMU without PITM, MMU with PITM, catalyst coated MMU (CCM) without PITM and CCM with PITM (see as example in Fig. A.2). In cells without PITM, pristine membranes were used whereas in cells with PITM, the central membrane of the MMU contained PITM which was deposited beforehand in a process described in the next section.

The optional catalyst layers were prepared with Pt black as described above. This catalyst was selected due to the relatively large crystallite size of its Pt particles of around 9

nm which improves its thermodynamic stability. Therefore, additional Pt deposition from the catalyst layers during operation can be avoided. The MMU was hot pressed with gas diffusion layers (GDL) on both sides (Sigracet GDL 25 BC, SGL Technologies GmbH) for 5 min at 160 °C with 700 N cm^{-2}. For operation in the test station, the cells were mounted in the test station as single cells via cell holders as described above. In the degradation test, the cells were operated at different settings of reactant pressures which yielded either a low or high potential of the PITM.

The settings were chosen based on the results from experiment with the Pt microelectrode and kept for 24 to 70 h each. To check for reproducibility, the settings were repeated. The cell temperature was set to 80 °C. H_2 and O_2 were fed to the cells with equal flow rates of 40 sccm at 76 °C. The cells were not electrically connected that means current or voltage was not controlled. During the degradation test, condensate water from anode and cathode side was collected in polyethylene bottles for analysis of fluoride emission.

For obtaining a blank, i.e. uncoated, membrane containing typical Pt precipitations, Pt was deposited from the catalyst of a single-side catalyst coated membrane (geometric electrode area: 5 cm x 5 cm, IP111, Ion Power Inc.) into a blank Nafion® membrane (size: 6.5 cm x 6.5 cm, NRE-212CS, DuPont) under fuel cell operating conditions. For this, the membranes were arranged to each other so that the catalyst layer of the IP111 was facing the blank membrane. In order to increase the oxygen transport across the IP111 membrane to the catalyst layer, the catalyst coated membrane was perforated with a scalpel beforehand.

The combined membranes were sandwiched between GDL, which was the Sigracet GDL 25 BC (SGL Technologies GmbH) on the side of the IP111 and a Sigracet GDL 25 BA (SGL Technologies GmbH) on the side of the NRE-212CS. The latter did not exhibit a micro-porous layer so that the contamination of the membrane by deposition of carbon from the MPL could be avoided. The arrangement of the membranes is shown in Fig. A.3. This cell was then assembled the same was as described above and operated in the test station for 64 h at OCV. As in the other experiments, the cell temperature was set to 80 °C and the temperatures of the humidifiers to 76 °C. For dissolving the Pt in the catalyst layer, 50 sccm oxygen was supplied at 150 kPa to the side of the catalyst coated membrane. The Pt-ions in the blank membrane were reduced to metallic Pt by feeding 50 sccm H_2 with 110 kPa to the membrane.

After the preparation of the PITM-membrane, the NRE-212CS membrane (containing now PITM) was separated from the CCM and rinsed for 4 h in demineralized water which was heated to 60 °C and stirred in a beaker with a speed of 500 rpm. After drying the membrane between precision wipes (Kimtech, Kimberly-Clark), it was ready for usage as the PITM-membrane in a MMU for the degradation experiment.

Membrane decomposition was measured based on fluoride ion concentration in the collected condensate. The concentration was measured with an ion selective electrode (laboratory meter ProLab 4000 and fluoride electrode F 60, SCHOTT Instruments). The electrode was calibrated over the range of 10-10000 μmolF l-1 using KF aqueous standard solutions.

The standard samples and condensate samples (15 ml) were diluted with buffer solution (TISAB II, Bernd Kraft GmbH) with a ratio of 1:1. The reading of the meter was recorded

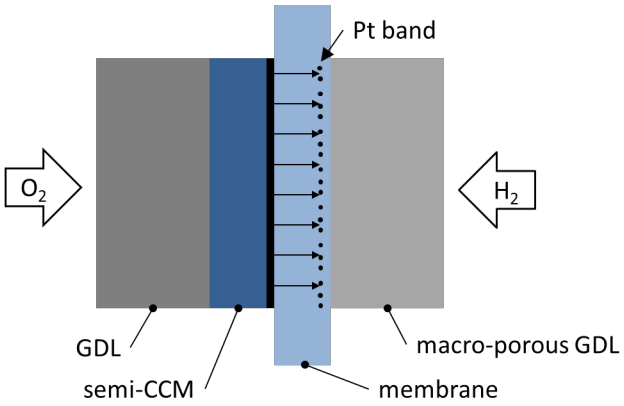

Figure A.3: Cell configuration for Pt deposition in the membrane

after equilibrium was reached; typically 5-10 min after the electrode was immersed into the solution. The error of the given measurement data include the electrode error of Âś 2

The membrane cross sections were examined with SEM to determine the position of the PITM and the distribution of Pt particles. Samples with a width (i.e., cross-sectional length) of approximately 3 mm were cut from the CCM and MMU with PITM after operation in the test station. For preparation of cross-sections via freeze-fractioning, GDLs were removed from the samples which were then immersed in liquid nitrogen and broken.

SEM measurements were conducted on an ULTRA plus (Zeiss Corp.) scanning electron microscope. The images were recorded based on secondary electrons (SE) and backscattered electrons (BE) at 3 or 5 kV. The resolution of the SEM was 1.0 nm at 15 kV and 1.7 nm at 1 kV. SEM micrographs were analyzed with ImageJ 1.46r software (National Institute of Health) to determine the number of single Pt particles as well as their position and area. Based on these data, the equivalent particle diameter and the nearest neighbor distance were calculated for each particle. For each MEA sample, the single values of diameter and distance were averaged. Furthermore, the particle density, i. e. the ratio of the image area covered by particles to the total image area, and the particle intensity, i.e., the number of particles in the total image area, were determined.